INFORMATION TO USERS

This manuscript has been reproduced from the microfilm master. UMI films the text directly from the original or copy submitted. Thus, some thesis and dissertation copies are in typewriter face, while others may be from any type of computer printer.

The quality of this reproduction is dependent upon the quality of the copy submitted. Broken or indistinct print, colored or poor quality illustrations and photographs, print bleedthrough, substandard margins, and improper alignment can adversely affect reproduction.

In the unlikely event that the author did not send UMI a complete manuscript and there are missing pages, these will be noted. Also, if unauthorized copyright material had to be removed, a note will indicate the deletion.

Oversize materials (e.g., maps, drawings, charts) are reproduced by sectioning the original, beginning at the upper left-hand corner and continuing from left to right in equal sections with small overlaps.

Photographs included in the original manuscript have been reproduced xerographically in this copy. Higher quality 6" x 9" black and white photographic prints are available for any photographs or illustrations appearing in this copy for an additional charge. Contact UMI directly to order.

UMI®

A Study on $^{15}C(d,p)^{16}C$ Reaction and the Role of Neutron Capture by ^{15}C in Big Bang Nucleosynthesis

DISSERTATION

Presented in Partial Fulfillment of the Requirements for

the Degree Doctor of Philosophy in the Graduate

School of The Ohio State University

By

Recep Taygun Güray, M.Sc.

* * * * *

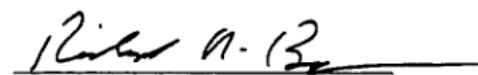The Ohio State University

2000

Dissertation Committee:

Dr. Richard N. Boyd, Advisor

Dr. Robert J. Scherrer

Dr. Evan R. Sugarbaker

Dr. Gregory Lafyatis

Approved by

_____

Advisor

Department of Physics

UMI Number: 9994870

UMI®

UMI Microform 9994870

ABSTRACT

There are two branch points found in the mass flow from light to heavy elements in various inhomogeneous big bang scenarios. Since the $^{15}C(n,\gamma)^{16}C$ governs one of these branch points, its reaction rate may be an important ingredient for network calculations needed to predict cosmic abundances. Therefore, because of the experimental impossibility of studying the $^{15}C(n,\gamma)^{16}C$ reaction, the astrophysically important reaction $^{15}C(n,\gamma)^{16}C$ cross section was investigated by measuring the transfer reaction $^{15}C(d,p)^{16}C$ to bound states and to states above the ^{16}C neutron emission threshold. The bound states give information on direct contributions to $^{15}C(n,\gamma)^{16}C$, and the unbound states levels give the resonant contributions.

The angular distribution of the differential cross section of $^{15}C(d,p)^{16}C$ transfer reaction was compared to that from the distorted wave Born approximation (DWBA) calculations results in order to determine the angular momentum transfers through which the reaction is proceeding. It seems that, from this comparison, the dominant angular momentum transfer is $L = 2$ transfer.

Any contribution of $L = 0$ transfer to the reaction yield would have an unobservable effect on the observed yield. This is due to two factors, one being the poor experimental resolution, and the other being the intrinsic dominance of the reaction yield by $L = 2$ transfer, as shown by the DWBA results. Therefore, the potential

ii

contribution of any state populated by zero angular momentum ($L = 0$) transfer is indeterminate. This is unfortunate. The aim of the experiment was to identify states in ^{16}C below and just above the neutron threshold with the hope of determining the nonresonant and resonant cross section components of the ^{15}C(n,γ)^{16}C reaction. Excited states potentially populated by $L = 0$ transfer, through which resonant scattering could occur, would be expected to dominate the astrophysical reaction rate for ^{15}C(n,γ)^{16}C reaction. However, we were unable to identify any such states.

To future, my son Kuzey Sarp

ACKNOWLEDGMENTS

I would like to express my sincere gratitude to Dr. Richard N. Boyd, my academic advisor, for his guidance and continuous encouragement, as well as his personal understanding and kindness, throughout the course of this research. I would like to thank Dr. Alexander Murphy for assisting me in working through the details involved in many of the ideas, specially the Monte Carlo simulation, presented here.

I wish to thank the members of Dr. Boyd's group for their support and the friendship we shared. I take this opportunity to thank Dr. Gerhard Raimann for computer expertise.

I would like to thank Dr. Daniel Bazin of National Superconducting Cyclotron Laboratory at Michigan State University for his technical assistance and for email correspondence.

Finally, my deepest gratitude to my wife Nalan and my parents for their strong encouragement, cheerful support, and everlasting endurance.

v

Recep Taygun Güray

VITA

09 April 1966 .... Born - Ankara. Turkey

1987 .... B.A. Engineering Physics
                                           University of Ankara
                                           Ankara.Turkey

1988 - 1993 .... Teaching Assistant
                                           Department of Engineering Physics
                                           University of Ankara
                                           Ankara. Turkey

1992 .... M.Sc. Nuclear Engineering
                                           Middle East Tec. University
                                           Ankara. Turkey

1998 .... M.Sc. Department of Physics
                                           The Ohio State University
                                           Columbus. OH

1997 - 2000 .... Graduate Teaching Assistant
                                           Department of Physics
                                           The Ohio State University
                                           Columbus. OH

Publications

Measurements of Low Energy Proton Radiative Capture Cross Sections.
F.R. Chloupek. A. St.J. Murphy. R.N. Boyd. A.L. Cole. J. Goerres. **R.T. Guray.**
G. Raimann. J. Von Schwarzenburg. M.C. Wiesher. 1999. Nuclear Physics A. 652.
391-405.

Cesium-137 Levels in Surface Soils Over The Black Sea Coast of Turkey.
T. Yesin. **R.T. Guray.** 1993. Turkish Journal of Engineering and Environmental
Sciences. 17. 213-216.

Fields of Study

Major Field: Physics

Minor Field: Nuclear Astrophysics

vii

TABLE OF CONTENTS

viii

ix

LIST OF FIGURES

x

xi

xii

LIST OF TABLES

xiv

CHAPTER 1

Big Bang Nucleosynthesis

1.1 Introduction

Over the past few decades big bang nucleosynthesis has emerged as one of the corner-stones [*Malaney and Mathews*(1993)] of the big bang, joining the Hubble expansion and the cosmic microwave background radiation. Big bang nucleosynthesis probes the Universe to the earliest times, from a fraction of a second to hundreds of seconds.

The big bang nucleosynthesis story begins with Gamow and his collaborators, who viewed the early Universe as a nuclear furnace that could "cook the periodic table" [*Kragh*(1996)]. In 1948 they proposed that all of the elements in the periodic table could be produced in the big bang. It was soon realized, according to the standard big bang scenario, that the lack of stable nuclei of mass 5 and 8 prevent significant nucleosynthesis beyond ^{7}Li.

The standard model of primordial nucleosynthesis, which describes elemental abundances resulting from nucleonic freeze-out from the big bang, has been very successful. It puts strong limitations on the mass of the universe, which is related to the usual abundance parameter η, the ratio of the number of baryons to photons in

1

the universe. In this standard model only nuclei below mass number 8 are produced and their abundances are found to produce a qualitative match with the observed primordial abundances.

In recent years, models of non-standard big bang scenarios have been discussed where inhomogeneties between the initial proton and neutron distribution arise following the early quark-gluon phase transition [*Malaney and Mathews*(1993)]. There are some theoretical indications [*Boyd and Kajino*(1989), *Malaney and Fowler*(1989), *Kajino and Boyd*(1990)] that ^{9}Be and ^{11}B might be a product of primordial nucleosynthesis, which could be explained in an inhomogeneous big bang.

The inhomogeneous big bang involves reaction chains composed of light, neutron-rich isotopes for the mass region around ^{9}Be. This scenario offers the possibility of bridging the mass 8 gap that limits isotopic production in the standard big bang.

1.2 Standard Big Bang Nucleosynthesis

The Standard Big Bang Model assumes a homogeneous, isotropic expansion from an initial state of very high temperature, $T \sim 10^{19}$GeV, and density, $\rho \sim 10^{78}$ GeV fm^{-3} [*Malaney and Mathews*(1993)]. The present state of the universe is characterized by four large scale phenomena [*Rolfs and Rodney*(1988), *Kragh*(1996), *Pagel*(1997)]:

1- The Hubble expansion law: The linear relation between distance and velocity of galaxies can be explained in a natural way by an expanding universe. During the 1920's and 1930's, Edwin Hubble discovered that the universe is expanding, with galaxies moving away from each other at a velocity given by an expression known

2

as the Hubble expansion law: $v = H * r$. Here v represents the galaxy's recessional velocity, r is its distance away from Earth, and H is a constant of proportionality called the Hubble constant. The Hubble constant has been recently determined using 42 Type Ia supernovae as standard candles: it is 70 kilometers per second for every megaparsec in distance, km/sec/Mpc (A megaparsec is given by 1 Mpc = 3 10^6 light-years), and also, the results of this study are fully consistent with the existence of a Λ cosmological constant (vacuum energy) whose contribution to the energy density is around 70% of the critical density which is defined below. That is strongly inconsistent with a $\Lambda = 0$ flat cosmology [*Perlmutter et al.*(1999)].

2- The cosmic microwave background radiation: In 1964, Penzias and Wilson discovered that the Universe is filled with microwave radiation, coming from all directions. This is the redshifted remnant of thermal radiation in the Universe when it was only about 300,000 years old, and was at a temperature of about 4,000K. Using the COBE (Cosmic Background Explorer) satellite, the spectrum of the radiation was found to be a perfect black body spectrum, with a temperature of 2.728 ± 0.002 K [*Smoot and Scott*(1998)].

3- The ratio for the number of nucleons (baryons) per proton: The baryon number N_B is a conserved quantum number in the Standard Model. Of the stable particles, protons and neutrons have $N_B=1$, while the rest carry zero baryon number. We do not know of any sizable density of antiprotons or antineutrons in the Universe, so it seems that the baryon number density does not vanish, although it is very small when compared to the number density of photons: $N_B/N_\gamma \simeq 10^{-9}$. This is just a

3

parameter which must be set by hand in the Standard Big Bang.

4- The universal abundance by weight of about 25% ⁴He and 75% H: The theory predicts that most of the matter in the Universe, about 75% by mass, is Hydrogen, and about 24 % is Helium, with a trace contribution from the rest. The proportions of the light elements, such as ⁴He, D, ³He, and ⁷Li can all be explained fairly well by the nuclear reactions that happened when the Universe was between 1 and 100 seconds old. The important point is that the prediction depends critically on the density of baryons (i.e. neutrons and protons) at the time of the Big Bang Nucleosynthesis; that will be discussed in detail below.

To understand why approximately one-quarter of the mass of the Universe is in the form of helium, let us consider the radiation era, when the expansion of the Universe was governed by the equivalent mass density of the blackbody radiation. The time-dependence of the expansion of the Universe was slightly reduced during the radiation era. The expansion rate is governed by the Freidmann equation [*Kolb and Turner*(1990)].

$$H^2 = \left(\frac{\dot{R}}{R}\right)^2 = \left(\frac{8\pi G}{3}\rho\right) - \frac{kc^2}{R^2} \tag{1.1}$$

where ρ is the energy density of the Universe, G is the gravitation constant, k is the curvature constant, and R is the scale factor. This serves to define the density parameter $\Omega = \rho/\rho_c$, where $\rho_c = 3H^2/8\pi G$, the critical density. The expansion of the early Universe at large redshifts is very well described by the equations for a flat Universe, those with $k=0$ and $\Omega=1$. This means that Equation 1.1 can be used with $k=0$. In the radiation era, however, the mass density ρ must be replaced by the

4

equivalent mass density of the cosmic background radiation. ρ_{rad}. Then. Equation 1.1 becomes

$$\left(\frac{\dot{R}}{R}\right)^2 = \frac{8\pi G}{3}\rho_{rad} \tag{1.2}$$

Since the energy density of blackbody radiation is aT^4. where a is the radiation constant. Equation 1.2 is

$$\frac{\dot{R}}{R} = \left(\frac{8\pi G a T^4}{3c^2}\right)^{1/2} \tag{1.3}$$

Because $\dot{R}/R = \dot{T}/T$. Equation 1.3 can be rewritten as

$$\frac{dT}{T^3} = -\left(\frac{8\pi G a}{3c^2}\right)^{1/2} dt \tag{1.4}$$

Equation 1.4 can be integrated with $T = \infty$ at $t = 0$ to give the temperature at time t during the radiation era as

$$T(t) = \left(\frac{3c^2}{32\pi G a}\right)^{1/4} t^{-1/2} \tag{1.5}$$

The epoch of the nucleosynthesis is very well discussed in [*Yang et al.*(1984). *Boesgaard and Steigman*(1985). *Kolb and Turner*(1990). *Walker et al.*(1991). *Smith et al.*(1993)]. At a temperature just below 10^{11} K ($t >\sim 10^{-2}$s). the universe contained a mixture of photons (γ). electron-positron pairs. neutrinos (ν) and their antiparticles. Electrons and neutrinos are kept in the thermal equilibrium by the neutral current weak interaction as

$$e^+ + e^- \leftrightarrow \nu_i + \overline{\nu_i} \tag{1.6}$$

(where $i = e. \mu. \tau....$). There were also a smaller number of protons and neutrons. about five for every 10^{10} photons [*Burles et al.*(1999)]. that were kept in equilibrium

5

via the reactions

$$n \leftrightarrow p + e^- + \overline{\nu_r} \qquad (1.7)$$

$$n + e^+ \leftrightarrow p + \overline{\nu_r} \qquad (1.8)$$

$$p + e^- \leftrightarrow n + \nu_r \qquad (1.9)$$

These constant transformations were easily accomplished because of the small mass-energy difference between the proton and the neutron. $(m_n - m_p)c^2 = 1.293$ MeV. The ratio of free neutrons to free protons assumes its equilibrium value.

$$\frac{n}{p} = exp[-\frac{(m_n - m_p)c^2}{kT}] \sim 1 \qquad (1.10)$$

because the mass difference between the protons and the neutrons is negligible at such a high temperature.

As the Universe expanded and the temperature decreased. the number density ratio followed the Equation 1.10 as long as reactions (1.7). (1.8). and (1.9) were maintained fast enough to reach the equilibrium. However. detailed calculations show that when the temperature fell to about 10^{10} K. the time for these reactions exceeded the expansion time. At a temperature just above 10^{10} K. the reaction rates significantly decreased. for two reasons. The expansion had reduced the energy density of the neutrinos until they were unable to participate in reactions (1.7)-(1.9). Also. shortly thereafter. the characteristic thermal energy of the photons. kT. fell below the 1.022 MeV threshold for creating electron-positron pairs via the pair-production process

$$\gamma \rightarrow e^- + e^+ \qquad (1.11)$$

6

As a result, the electrons and positrons annihilated each other without being re-placed, leaving only a small remainder of excess electrons. For these, reasons, the neutrons could not be replenished as fast as they were destroyed. The creation of new neutrons could not keep up with the rate of expansion of the universe. The ratio of the number densities then was frozen at its value of $n/p = 0.223$ when the temperature is equal to about $10^{10} K$.

At this point, there were 223 neutrons for every 1000 protons, and essentially no more neutrons were being created. The beta decay reactions, the forward one in Equation 1.7, continued to convert neutrons into protons with a mean-life of 885.4 seconds [Arzumanov et al.(2000)]. It was not yet possible for the protons and neutrons to combine to form deuterium nuclei via

$$p + n \leftrightarrow d + \gamma \tag{1.12}$$

since high-energy photons quickly dissociated the nuclei at a temperature higher than 10^9 K. The neutrons and protons remained separated until the temperature had dropped from 10^{10} K to 10^9 K.

At a temperature below 10^9 K ($t > 10^2$s), there was no longer a sufficient density of high-energy photons to photodissociate the deuteron, so the neutrons and protons readily combined to form as many deuterium nuclei as possible. Then, a number of reactions led to the formation of the tightly bound nucleus, ^{4}He, involved in Big Bang nucleosynthesis. The efficient reactions leading ^{4}He are as follows [Boyd(1999)]:

$$p + n \rightarrow d + \gamma$$

7

$$d + p \rightarrow {}^3He + \gamma; \quad d + n \rightarrow {}^3H + \gamma;$$
$${}^3He + n \rightarrow {}^4He + \gamma; \quad {}^3H + p \rightarrow {}^4He + \gamma;$$
$${}^3He + d \rightarrow {}^4He + p \quad {}^3H + d \rightarrow {}^4He + n$$
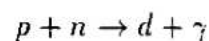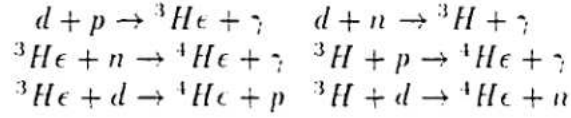
The relative abundances of different nuclei are fixed by nuclear statistical equilibrium, with the mass fraction of nuclear species A [*Kolb and Turner*(1990)].

$$X_A \propto (kT/M_N c^2)^{\frac{3(A-1)}{2}} \eta^{A-1} exp(B_A/kT) \tag{1.13}$$

where B_A is the binding energy, M_N is the nucleon rest-mass, and η is the baryon-to-photon ratio.

Figure 1.1 shows the evolution of the light element abundances with decreasing temperature. At $T \approx 1$ MeV the neutron-to-photon ratio freezes-out. For $T > 0.6$ MeV, the ^{4}He abundance has its nuclear statistical equilibrium (NSE) values. At $T \approx 0.6$ MeV, the ^{3}He, ^{3}H, and ^{4}He curves cross, and ^{4}He is forced to leave its NSE curve and plod along with ^{3}H and ^{3}He curves. This is because ^{4}He is so tightly bound. At this temperature ^{3}He(n,γ)^{4}He and ^{3}H(p,γ)^{4}He which keep ^{4}He in equilibrium with ^{3}He and ^{3}H are not fast enough to maintain the NSE abundance. Since the ^{4}He abundance falls off its NSE path, the reverse reactions slow down relative to those in the forward direction, so a short-lived but effective ^{3}He and ^{3}H bottleneck [*Smith et al.*(1993)] prevents ^{4}He from dominating all the abundances immediately.

At $T \approx 0.2$ MeV, ^{3}He and ^{3}H leave their NSE track since d(n,γ)^{3}H and d(p,γ)^{3}He, which keep them in equilibrium with d, slow down. The ^{3}He, ^{3}H, and ^{4}He abundances starts to follow along the deuterium NSE curve since the formation of deuterium (a minor deuterium bottleneck) limits these abundances. ^{3}He(n,p)^{3}H keeps ^{3}He in

8
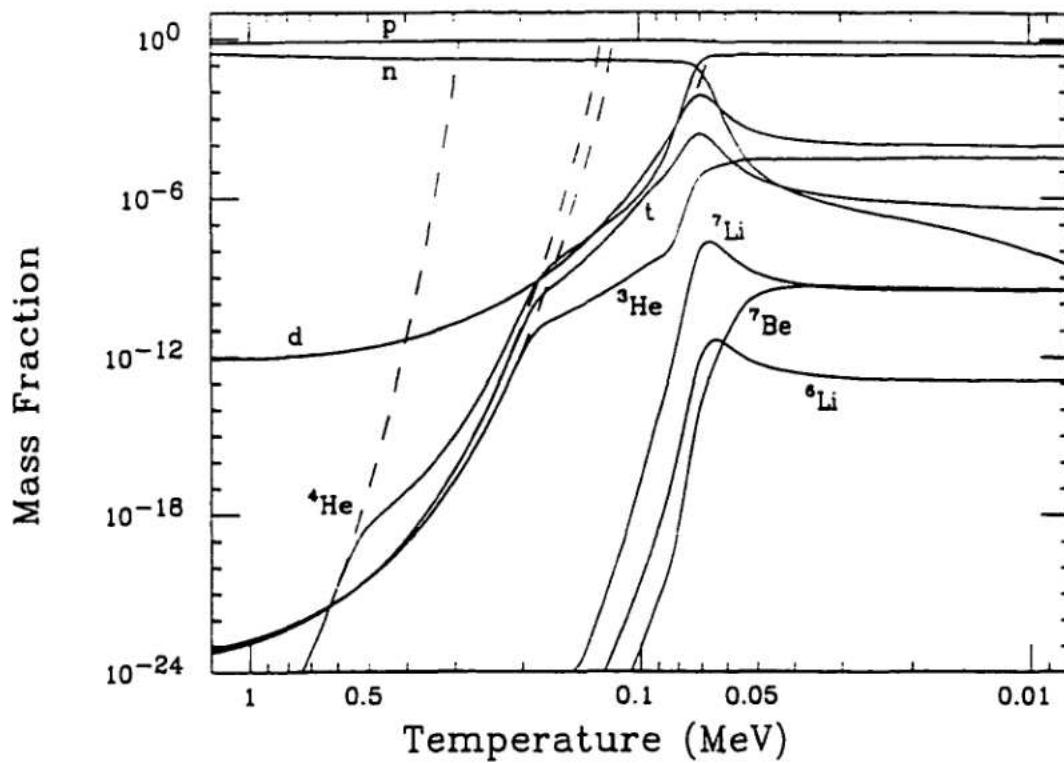
Figure 1.1: Evolution of light-element abundances with temperature, for a baryon-to-photon ratio $\eta_{10}=3.16$. The dashed curves give the NSE curves [Pagel(1997)].

9

equilibrium with ^{3}H until T=0.8 MeV. At T=0.07 MeV. the deuterium abundance falls out of NSE.

As the last of the light elements departs from its NSE track. nearly all the available neutrons are quickly processed into the most tightly bound of the light nuclei. ^{4}He [*Walker et al.*(1991)]. and ^{4}He production peaks. The mass fraction of ^{4}He produced is thus $X_s \approx 2(n/p)/(1+n/p) \approx 0.25$. Collisions of d. ^{3}H. and ^{3}He on the now abundant ^{4}He begin producing ^{6}Li. ^{7}Li. and ^{7}Be. and now these heavier nuclides. and d. ^{3}H and ^{3}He are in quasi-static equilibrium [*Smith et al.*(1993)]. Rilley and Irvine [*Riley and Irvine*(1991)] and Smith et al. [*Smith et al.*(1993)] determined that 12 reactions. shown in Figure 1.2. are primarily important in the production of the big bang nucleosynthesis. Unlike NSE. in quasi-static equilibrium. reactions have no longer equal magnitudes in both forward and reverse directions. however. the total forward processing rate of all reactions is still essentially the same in magnitude as the total reverse processing rate. The number abundance of each nuclear species i evolves through the rate equation [*Esmailzadeh et al.*(1991)]

$$\frac{dY_i}{dt} = \sum_{k,l} Y_k Y_l < kl > - \sum_j Y_i Y_j < ij > \qquad (1.14)$$

where $< kl >$ is the reaction rate for creating i. and $< ij >$ is the reaction rate for destroying i. The condition of quasi-static equilibrium gives the temperature-dependent solution

$$Y_i(T) = (\sum_{k,l} Y_k Y_l < kl >)/(\sum_j Y_j < ij >). \qquad (1.15)$$

10
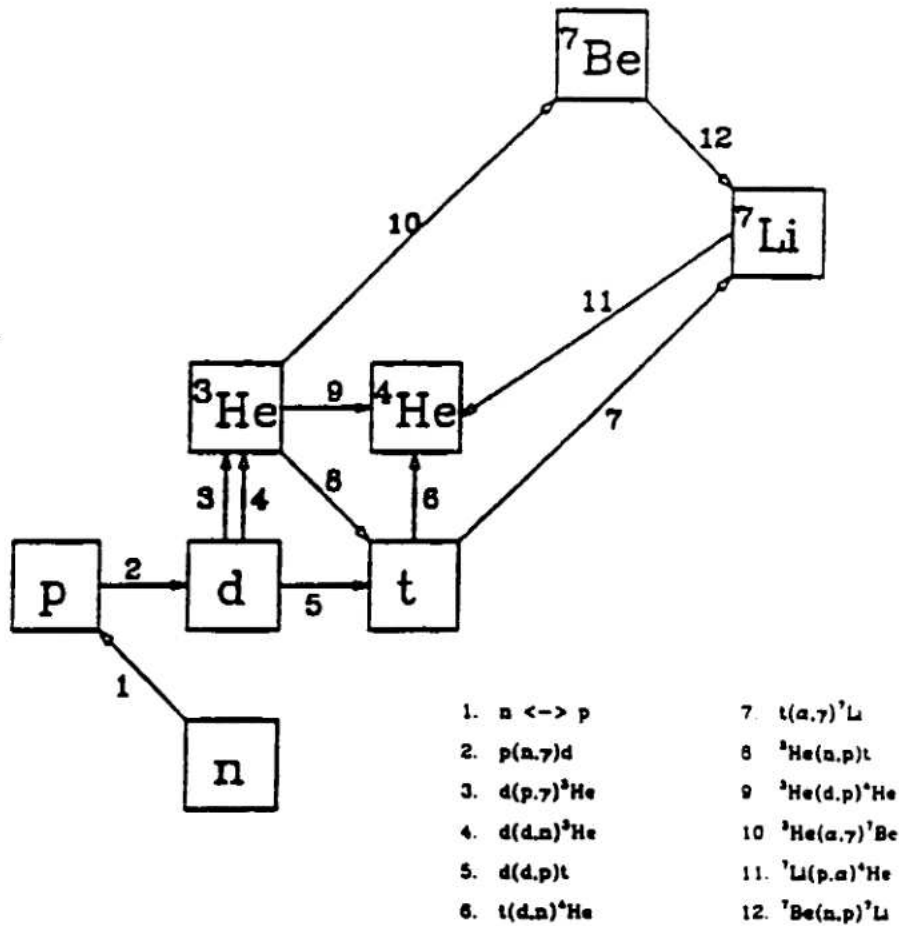
Figure 1.2: Network diagram of the 12 primary reactions [Smith(1993)].

1. n <-> p
2. p(n,γ)d
3. d(p,γ)³He
4. d(d,n)³He
5. d(d,p)t
6. t(d,n)⁴He
7. t(α,γ)⁷Li
8. ³He(n,p)t
9. ³He(d,p)⁴He
10. ³He(α,γ)⁷Be
11. ⁷Li(p,α)⁴He
12. ⁷Be(n,p)⁷Li

11

If the reaction rates for destroying and creating i are fast relative to the expansion rate, this condition is maintained. Until the abundance freezes out, the reactions keeping quasi-static equilibrium slow down as the temperature decreases.

The results of Standard Big Bang Nucleosynthesis are determined by the matter density, nuclear matrix elements, and the expansion rate. The matter density enters only through the ratio of baryons to photons η. Since the present temperature of the cosmic background radiation is known, η and the baryonic mass-density parameter Ω_B are directly related [Steigman et al.(1999)].

$$
\begin{aligned}
\Omega_B h^2 &= 3.675 \times 10^{-3} (T/2.73K)^3 \eta_{10} \\
&= 3.667 \times 10^{-3} \eta_{10}
\end{aligned}
\tag{1.16}
$$

where h is defined by the present Hubble parameter H_o ($\equiv h *100$ km s^{-1}Mpc^{-1}), T is the present microwave background temperature, and η_{10} is the baryon-to-photon ratio in units of 10^{10}. The abundances of individual nuclei depend on η in the following way [Thielemann et al.(1991), Rauscher et al.(1994)]. A high baryon density (i.e. large η) gives rise to a large number of capture reactions on d and ^{3}He, and consequently leaves less d and ^{3}He, but increases the ^{4}He. The behavior of the ^{7}Li abundance is more complex. At low densities ^{7}Li is produced via ^{3}H$(\alpha, \gamma)^7$Li, but is destroyed at higher densities by ^{7}Li$(p, \alpha)^4$He. However, increasing densities lead also to a larger production of ^{7}Be via ^{3}He$(\alpha, \gamma)^7$Be, which is preserved during the big bang nucleosynthesis period and subsequently decays to ^{7}Li. This leads to predicted minimum in the ^{7}Li abundance for $2 < \eta_{10} < 4$, as seen in Figure 1.3. Figure 1.3 shows the predicted abundances for ^{4}He (mass fraction Y_p), deuterium D, ^{3}He,

12
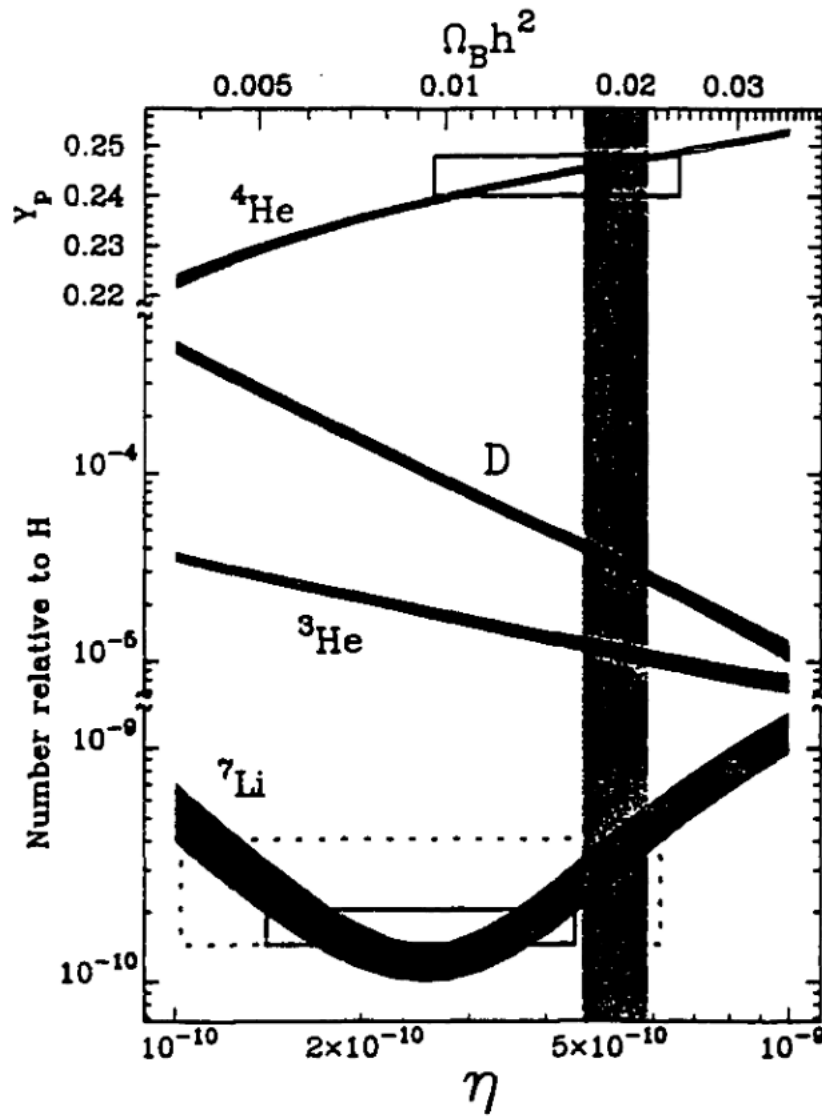
Figure 1.3: Light-element abundance versus baryon-to-photon ratio for the ^{4}He mass fraction. D. ^{3}He. and ^{7}Li [Burles(1999)].

13

and ^{7}Li versus the baryon-to-photon ratio η. as well as the observed abundances. The boxes indicate observationally acceptable regions for η. Because of the experimental uncertainties, standard big bang nucleosynthesis predictions are represented by bands on the abundance versus η plot. determined by performing Monte Carlo analysis [*Krauss and Romanelli*(1990). *Smith et al.*(1993). *Burles et al.*(1999)].

In addition to the η-dependency [*Thielemann et al.*(1991)]. the abundances resulting from big bang nucleosynthesis are also dependent upon the number of existing neutrinos species and the neutron half-life. In the standard model the neutron-to-proton ratio n/p. resulting from weak decoupling. is always smaller than 1 since the proton mass is smaller than neutron mass. If it is assumed that all neutrons combine with available protons to produce ^{4}He. then the ^{4}He mass fraction can be given $X_4 = 2X_n = 2n/(n + p) = 2(n/p)/(1 + (n/p))$. This makes the helium mass fraction X_4 a function of the neutron-to-proton ratio n/p at the time of big bang nucleosynthesis after freeze-out. Increasing the number of neutrino species has an effect equivalent to that of a faster expansion. This leads to an earlier weak decoupling. and thus a higher n/p ratio and a higher ^{4}He abundance. From reaction (1.7). a longer neutron half-life could result in a similar effect.

1.3 Inhomogeneous Big Bang Nucleosynthesis

A great deal of attention has been given to the possibility that baryons might be distributed inhomogeneously at the time of BBN. being highly concentrated in relatively isolated regions [*Applegate et al.*(1987). *Alcock et al.*(1987). *Malaney and*

14

$Mathews(1993)$]. Such inhomogenity could arise if the transition from the quark-gluon plasma to hadronic matter, which should take place at a time of around 10^{-5}sec, is a strongly first-order phase transition and occurs at a relatively low temperature of less than around 130 MeV [$Copi(1995)$]. In the homogeneous Big Bang Model, neutrons can diffuse easily through the primordial plasma, and the different diffusion lengths for neutrons and protons could lead to the formation of the high-baryon-density proton-rich regions and low-baryon-density neutron-rich regions [$Applegate\ et\ al.(1987)$]. Before the freeze-out from weak reaction equilibrium ($T \approx 1$ MeV), there is no segregation between neutrons and protons since the baryons only diffuse efficiently during the fraction of the time they spend as neutrons [$Suh\ and\ Mathews(1998)$]. After weak equilibrium freeze-out protons and neutrons diffuse independently [$Malaney\ and\ Mathews(1993)$].

Over the last a few decades the focus has been an understanding the evolution of the light-element abundances from the big bang to the present in order to test the BBN predictions for the primeval abundances.

1.3.1 Light Element Production

The primordial abundances of light elements in such inhomogeneous big bang nucleosynthesis models could be quite different from those homogeneous big bang nucleosynthesis. An inhomogeneity of this kind introduces new parameters, the density ratio R between high and low density regions, the mean separation between nucleation sites, the relative volume filling factor f_v of high density zones, and the

15

total baryon density Ω_B (or η) as in the standard model [*Mathews et al.*(1990), *Malaney and Fowler*(1988)].

Once the temperature has dropped below the photodissociation threshold for deuterium ($T \sim 100$ keV) [*Malaney and Mathews*(1993)] the epoch of nucleosynthesis can begin. However, because of neutron diffusion, the conditions for nucleosynthesis will involve regions of varying n/p ratio.

In the high-baryon-density proton-rich regions, using the expression for the ^{4}He abundance $X_\alpha = 2(n/p)/(1+n/p)$, a smaller He-abundance along with heavier elements than those in the standard model is expected because of the neutron diffusion and smaller (n/p) ratios. Because of the high baryon density, significant light and intermediate-mass destruction occurs [*Kajino and Boyd*(1990)] resulting in the ^{2}H and ^{3}He underabundances [*Thielemann et al.*(1991)]. Figure 1.a [*Malaney and Fowler*(1988)] shows the nucleosynthesis of the light isotopes in the proton-rich region, plotted as a function of time.

In the low-baryon-density neutron-rich regions, all available protons can be captured to form deuterium and subsequently ^{4}He [*Malaney and Mathews*(1993)]. As a consequence of the small initial (p/n) ratio, nucleosynthesis becomes effective after protons are formed by neutron decay, and this can lead to a local increase of deuterium and ^{4}He abundances in the neutron-rich regions. Also, relatively more ^{3}He is formed, due to the nucleosynthesis at lower densities [*Thielemann et al.*(1991)]. The ^{7}Li abundance is also high in these regions [*Malaney and Mathews*(1993)]. Figure

16
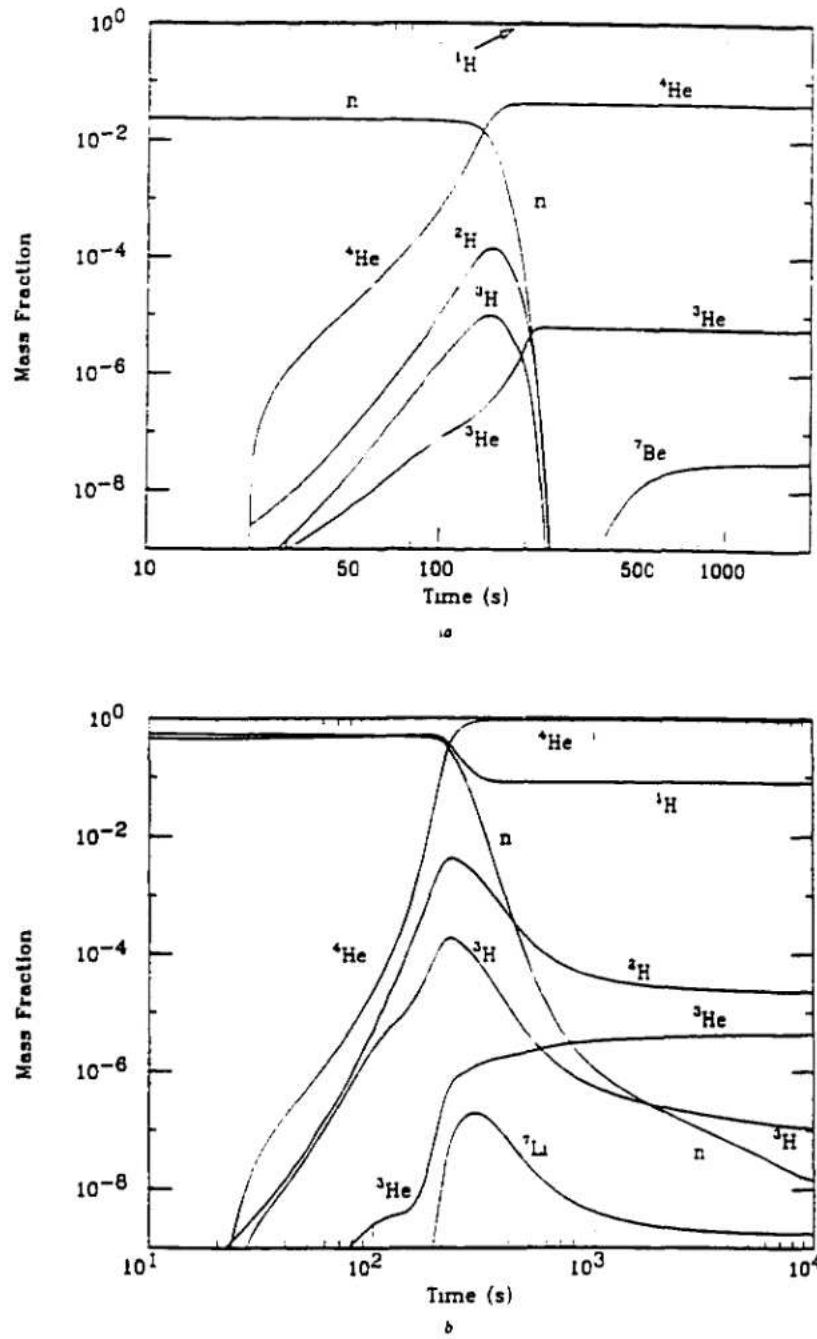
Figure 1.4: (a) The nucleosynthesis of the light isotopes in the proton-rich region of an $f_v \approx 0.1$. $\Omega_B = 1$ universe. plotted as a function of time. (b) The nucleosynthesis of the light isotopes in the neutron-rich region of an $f_v \approx 0.1$. $\Omega_B = 1$ universe. plotted as a function of time [Malaney(1988)].

17

4.b [*Malaney and Fowler*(1988)] shows the nucleosynthesis of the light isotopes in the neutron-rich region plotted as a function of time.

The two regions affect the primordial abundances in different ways [*Thielemann et al*(1991)]. ^{7}Li is always overabundant by a factor of 10 - 100 compared to its abundance in the standard big bang. Back-diffusion of neutrons from the neutron-rich regions after neutron exhaustion in the high density regions was found to be able to reduce this overproduction via ^{7}Be$(n,p)^7$Li$(p,\alpha)^4$He [*Malaney and Fowler*(1988)].

The standard model with only one free parameter, η, which provided a fair fit to the ^{2}H, ^{3}He, ^{4}He, and ^{7}Li primordial abundances, was replaced by a model which has at least 4 parameters (R, f_v, l and Ω_B). Even though the inhomogeneous big bang models did not simplify the topic of primordial nucleosynthesis [*Rauscher et al.*(1994)], if the quark-hadron transition is a first order phase transition, density inhomogeneities will undoubtedly occur. Since theoretical estimates of the parameters at the time of the phase transition are very uncertain, a large parameter space had to be allowed for with constraints provided by the required fit to the primordial abundances [*Mathews et al.*(1990), *Mathews et al.*(1996), *Orito et all.*(1997)]. The model might predict relatively high primordial ^{9}Be abundance [*Boyd and Kajino*(1989), *Malaney and Fowler*(1989), *Kajino and Boyd*(1990)]. The detection of primordial ^{9}Be as well as higher-mass isotopes would put limits on the inhomogeneity of the big bang and if observed, could indicate deviations from the standard model.

18

1.3.2 Heavy Element Production

The most fascinating aspect of the inhomogeneous scenarios is that there appears for the first time an open window to form nuclei beyond mass $A=8$ in the neutron-rich regions. The main reaction chain which leads to the production of the ^7Li is $^1H(n,\gamma)^2H(n,\gamma)^3H$ $(d,n)^4He(t,\gamma)^7Li$, and the sequence starting with neutron capture on ^7Li, $^7Li(n,\gamma)^8Li(\alpha,n)^{11}B$ $(n,\gamma)^{12}B(\beta^-)^{12}C(n,\gamma)^{13}C(n,\gamma)$ $^{14}C(...)$ produces carbon [*Malaney and Fowler*(1988), *Applegate et al.*(1988a), *Applegate*(1988b), *Kajino and Boyd*(1990), *Kajino et al.*(1990), *Malaney and Mathews*(1993), *Boyd*(1999)]. An alternate branching is $^7Li(\alpha,\gamma)$ ^{11}B [*Rauscher et al.*(1994)]. Additional reactions such as $^7Li(t,n)^9Be(t,n)^{11}B$, $^8Li(n,\gamma)^9Li$ $(\beta^-)^9Be$, $^8Li(d,p)^9Li$, $^8Li(d,n)^9Be$, and $^8Li(d,t)^7Li$ might also become important [*Boyd and Kajino*(1989), *Kajino and Boyd*(1990), *Brune et al.*(1991), *Balbes et al.*(1993), *Balbes et al.*(1995)]. If the neutron-rich nuclei ^9Li, ^{10}Be, and ^{13}B are produced, further (α,n) reactions, $^9Li(\alpha,n)^{12}B$, $^{10}Be(\alpha,n)^{13}C$, and $^{13}B(\alpha,n)^{16}N$, can become important. These rates have been investigated with statistical model methods [*Rauscher et al.*(1994)]. At three positions (^7Li, ^9Be, and ^{11}B), proton-induced reactions would prevent the buildup of heavier nuclei in a standard big bang scenario and lead to the destruction of heavy nuclei instead via $^7Li(p,\alpha)^4He$, $^9Be(p,\alpha)^6Li$, or $^{11}B(p,2\alpha)^4He$ [*Rauscher et al.*(1994)]. There are considerable associated uncertainties, because many of these reactions on stable targets in this region of the nuclear chart are not well determined [*Malaney and Fowler*(1989), *Fowler*(1993)].

19

Once ^{14}C has been produced, there are possible pathways to heavier nuclei that can occur [*Applegate et al.*(1988a), *Applegate*(1988b)], starting from ^{14}C: ^{14}C(α,γ) ^{18}O(n,γ)^{19}O(β⁻) ^{19}F(n,γ)^{20}F(β⁻)^{20}Ne(n,γ)^{21}Ne (n,γ)^{22}Ne, etc. However, it has been demonstrated [*Wiescher et al.*(1990), *Kajino et al.*(1988a)] that the (p,γ) and (n,γ) reactions on ^{14}C are of greater importance for the build-up of heavy elements. Once past the oxygen isotopes, the reactions are dominated by neutron captures and beta decays.

The neutron captures are fairly slow until nuclei with mass number $A \approx 60$ are produced, but become rapid afterwards because of large neutron capture cross sections of heavier nuclei, potentially leading to an r-process [*Applegate et al.*(1988a), *Applegate*(1988b)]. A nucleus captures neutrons and beta decays until it fissions. Once fission has occurred, both daughter nuclei capture neutrons until they grow to the point of fission. Now four nuclei can capture neutrons and grow. Once they fission, eight nuclei exist, then sixteen. This runaway fission cycling is limited by the neutron supply, which is primarily determined by Ω_B, and by the time required to make a cycle, which is determined by how far the nucleosynthesis path is located from the valley of stability [*Applegate*(1988b), *Rauscher et al.*(1994)]. [*Applegate et al.*(1988a)] and [*Applegate*(1988b)] used neutron capture cross sections and fission cycle times estimated for the r-process and found that, while the number of fission cycles was quite uncertain, observable, and possibly even excessive, levels of r-process enrichment were possible. [*Rauscher et al.*(1994)] computed the synthesis of heavy elements in neutron-rich environments fully self-consistently with the changing neutron density

20

using a detailed reaction network. and found that the production of heavy elements is very sensitive to baryon density.

1.3.3 Motivation

$^{14}C(n,\gamma)^{15}C$ and subsequent neutron capture process on neutron-rich carbon. nitrogen. and oxygen isotopes may bypass the long-lived ^{14}C and may trigger a primordial r-process [*Kajino and Boyd*(1990)]. This is in contrast to the result of [*Applegate et al.*(1988a)] and [*Malaney and Fowler*(1988)]. where $^{14}C(\alpha,\gamma)^{18}O$ plays the major role in heavy-element production.

Two critical branch points are found in this subsequent neutron capture process [*Boyd*(1999)]. First. there are two possible reactions which follow $^{14}C(n,\gamma)^{15}C$ reaction as

$$^{14}C(n,\gamma)^{15}C(\beta^-)^{15}N$$

or

$$^{14}C(n,\gamma)^{15}C(n,\gamma)^{16}C$$
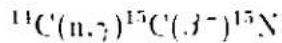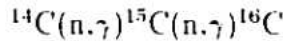
If ^{15}C beta decays to ^{15}N. it will quickly be returned to ^{12}C by the reaction $^{15}N(p,\alpha)^{12}C$. If ^{15}C captures a neutron to make ^{16}C. it can move on to heavier nuclei. and then the second sequence is possible as follows

$$^{15}C(n,\gamma)^{16}C(\beta^-)^{16}N(n,\gamma)^{17}N$$
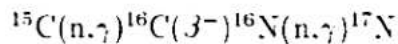
There two possible reactions which follows $^{17}N(n,\gamma)^{18}N$ reaction as

$$^{17}N(n,\gamma)^{18}N(\beta^-)^{18}O$$

or

21

$^{17}N(n,\gamma)^{18}N(n,\gamma)^{19}N$
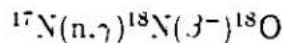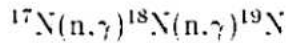
If ^{18}N beta decays to ^{18}O, it will quickly be returned to ^{15}N by the reaction $^{18}O(p,\alpha)^{15}N$, which as mentioned above will be returned to ^{12}C, quickly terminating the progression to heavier nuclei by that nucleus. If ^{18}N captures a neutron to make ^{19}N, it can move on to heavier nuclei.

Since the $^{15}C(n,\gamma)^{16}C$ reaction governs one of these branch points in the mass flow from light to heavy elements in various inhomogeneous big bang scenarios, its reaction rate may be an important ingredient for network calculations needed to predict cosmic abundances. In this study, it was therefore proposed to investigate the astrophysically important reaction $^{15}C(n,\gamma)^{16}C$ cross section. Studies of reactions of importance to primordial nucleosynthesis often require neutron captures on shortlived nuclides, usually an experimental impossibility [Boyd(1999)]. One must therefore utilize other experimental approaches to determine the cross section of interest. In this context, it was proposed to study the cross section of $^{15}C(n,\gamma)^{16}C$ by measuring the transfer reaction $^{15}C(d,p)^{16}C$ to bound states and to states above the threshold. The bound states give information on direct contributions to $^{15}C(n,\gamma)^{16}C$ reaction, and the unbound levels give the resonant contributions.

1.4 Calculation of the Reaction Rates for Neutron Capture Reactions

Calculation of capture reaction rates are very well discussed in [*Rolfs and Rodney*(1988). *Wiescher et al.*(1990). *Mohr et al.*(1993). *Rauscher et al.*(1994). *Herndl et al.*(1995). *Herndl et al.*(1999)]. The cross section for neutron capture processes is dominated by nonresonant direct capture process and by contributions from resonances which correspond to neutron unbound states in the compound nucleus. For calculating the different reaction contributions. the nonresonant contributions are determined by using a direct capture model. and the resonant contributions are based on determining the resonant Breit-Wigner cross section. For determining the neutron capture cross sections on the β-unstable nuclei. the input parameters for the calculations are taken from experimental data. If there are no experimental data available. theoretical values mainly obtained from the shell model are used.

The total reaction rate can be given as

$$N_A \langle \sigma v \rangle_{tot} = N_A \langle \sigma v \rangle_R + N_A \langle \sigma v \rangle_{NR} \tag{1.17}$$

where. $N_A \langle \sigma v \rangle_R$ is the resonant contribution term. and $N_A \langle \sigma v \rangle_{NR}$ is the nonresonant contribution term. Here. $\langle \sigma v \rangle$ is the reaction rate per particle pair that can be defined for a temperature T [*Rolfs and Rodney*(1988)] by

$$\langle \sigma v \rangle = \left(\frac{8}{\pi \mu} \right)^{1/2} \frac{1}{(kT)^{3/2}} \int_0^\infty \sigma(E) E \, exp \left(-\frac{E}{kT} \right) \, dE \tag{1.18}$$

where μ is the reduced mass of the interacting particles. E is the centre of mass energy.

23

1.4.1 Resonant Reaction Rate

The cross section of a single level resonance in neutron capture process is described by the Breit Wigner formula [*Rolfs and Rodney*(1988)]

$$\sigma_R(E) = \frac{\pi \hbar^2}{2\mu E} \frac{(2J+1)}{(2J_T+1)(2J_n+1)} \frac{\Gamma_n \Gamma_\gamma}{(E-E_R)^2 + (\Gamma/2)^2} \tag{1.19}$$

where, J is the angular momentum of the resonant state, J_T and J_n are the spins of the target nucleus and the neutron projectile, respectively, E_R is the resonance energy, Γ_n and Γ_γ are the partial width of the entrance and exit channels, respectively, and Γ is the total width which is the sum of the partial widths of all open decay channels. The neutron partial width Γ_n can be given [*Wiescher et al.*(1990), *Herndl et al.*(1995)] by

$$\Gamma_n = C^2 \mathcal{S} \times \Gamma_{sp} \tag{1.20}$$

where $\mathcal{S}$ is the single particle spectroscopic factor, C is the isospin Clebsch-Gordon coefficient, and Γ_{sp} is the single particle width of the resonance state.

The thermal average of σv (Equation 1.18) over a narrow resonance gives a reaction rate of the form [*Rolfs and Rodney*(1988)]

$$\langle \sigma v \rangle = \left(\frac{2\pi}{\mu kT} \right)^{3/2} \hbar^2 (\omega \gamma) \, exp \left(-\frac{E_R}{kT} \right) \tag{1.21}$$

where $\omega \gamma$ is the resonance strength which is given as

$$\omega \gamma = \frac{(2J+1)}{(2J_T+1)(2J_n+1)} \frac{\Gamma_n \Gamma_\gamma}{\Gamma} \tag{1.22}$$

24

when a nuclear reactions has several narrow resonances their contributions to $\langle \sigma v \rangle$ are summed:

$$\langle \sigma v \rangle = \left(\frac{2\pi}{\mu k T} \right)^{3/2} \hbar^2 \sum_i (\omega \gamma)_i \, exp \left(-\frac{E_{R_i}}{kT} \right) \tag{1.23}$$

The resonance strength has to be determined experimentally by low energy neutron capture measurements or has to be derived from the calculated partial widths.

1.4.2   Nonresonant Reaction Rates

The nonresonant part of the neutron capture cross section can be calculated using the direct capture model [Kim et $al.$(1987), $Mohr$ et $al.$(1993)]. The total cross section σ_{NR} is determined by the direct capture transitions σ_i^{DC} to all bound states with the single particle spectroscopic factors $(C^2S)_i$ in the final nucleus

$$\sigma_{NR} = \sum_i (C^2S)_i \, \sigma_i^{DC} \tag{1.24}$$

The direct capture cross sections σ_i^{DC} are determined by the overlap of the scattered wave function in the entrance channel, the bound state wave function in the exit channel, and multiple transition operator.

If the Q value of the neutron capture reaction energy is much higher than the neutron energy, the cross section for s-wave neutron capture follows a $1/v$ law, that is the reaction rate is constant over the entire temperature range, $\langle \sigma v \rangle = \sigma v = constant$

25

[*Fowler*(1967), *Rolfs and Rodney*(1988), *Wiescher et al.*(1990)]. Therefore, the s-wave contribution to the direct capture reaction rate can be obtained from the thermal cross section, σ_{th}.

$$N_A \langle \sigma v \rangle_s = N_A \times \sigma_{th} v_{th} \tag{1.25}$$

The cross section for p-wave neutron capture contributions is proportional to the relative velocity v, therefore, the reaction rate proportional to the temperature as follows [*Fowler*(1967), *Wiescher et al.*(1990), *Fowler*(1975)]

$$N_A \langle \sigma v \rangle_p = \frac{1.08 \times 10^8}{\mu^{1/2}} \frac{\sigma_p(E)}{E^{1/2}} T_9 \quad cm^3 \, mole^{-1} \, s^{-1} \tag{1.26}$$

The total nonresonant reaction can be parametrized as a function of T_9 [*Herndl et al.*(1999)]

$$N_A \langle \sigma v \rangle_{NR} = A + B T_9 - C T_9^D \quad cm^3 \, mole^{-1} \, s^{-1} \tag{1.27}$$

The first and second terms are for the s- and p-wave contributions, and the third one is the d-wave contributions.

In order to calculate the single particle amplitude in both resonant and nonresonant neutron capture cross sections, the spectroscopic factors have to be known. These can be obtained experimentally from single particle transfer reaction studies. So, the spectroscopic factors necessary for $A(n,\gamma)B$ reaction can be extracted from $A(d,p)B$ reaction, the theory for which is explained in the next chapter.

26

CHAPTER 2

The (d,p) Stripping Reaction

2.1 Introduction

Direct nuclear reactions are very important in the the study of of nuclear structure. These take place in the time the projectile takes to traverse the target nucleus (typically around 10^{-22}s) [*Cohen*(1971)]. In these processes the projectile may interact with a nucleon, a group of nucleons or the whole nucleus and an emission takes place immediately. The simplest direct reaction is elastic scattering, which leaves the target in its ground state. In non-elastic reactions, the states of the residual nuclei which are excited have a simple structural relationship with the ground state of the target. Inelastic scattering predominantly excites collective states, one-nucleon transfer reactions tend to excite single-particle states, and multinucleon transfer reactions tend to excite cluster states. Measurement of the absolute cross-section for exciting each of these states, and of the angular distributions of the emitted particles, allows the study of the structure of these states. The direct reactions are very well discussed in [*Butler*(1957), *Enge*(1966), *Austern*(1970), *Satchler*(1983), *Glendenning*(1983), *Satchler*(1990)]. This chapter concentrates on the (d,p) reaction.

27

2.2 Nucleon Transfer Reaction: The (d,p) Stripping Reaction

A direct nucleon transfer reaction is a reaction in which one or more nucleons are transferred from the projectile to the target (stripping reactions) or from the target to the projectile (pick-up reactions). One of the one-nucleon transfer reactions is the (d,p) reaction which is essentially the transfer of a neutron from the projectile to the target to an unfilled single particle state of the target nucleus. The same formalism and methods of analysis are applicable to other one-nucleon transfer reactions and in particular to the (d,n) reaction.

Historically, the (d,p) reaction was the first of these reactions to be studied in detail, and it showed their value for studies of nuclear structure [*Oppenheimer and Phillips*(1935)]. The angular distributions of the protons from (d,p) reactions were soon found to be either forward or backward-peaked suggesting a direct process [*Satchler*(1983)]. The observation of a forward peak in reactions at high energies on light nuclei led Serber (1947) to suggest a very simple model of the reaction in which the neutron is captured by the target, leaving the proton to go on alone. The emitted proton momentum k_p is the sum of its translational momentum as part of the incident deuteron and its momentum within the deuteron. The angular spread of the outgoing protons is thus an indication of the momentum distribution of the proton inside the deuteron before the neutron was removed.

28
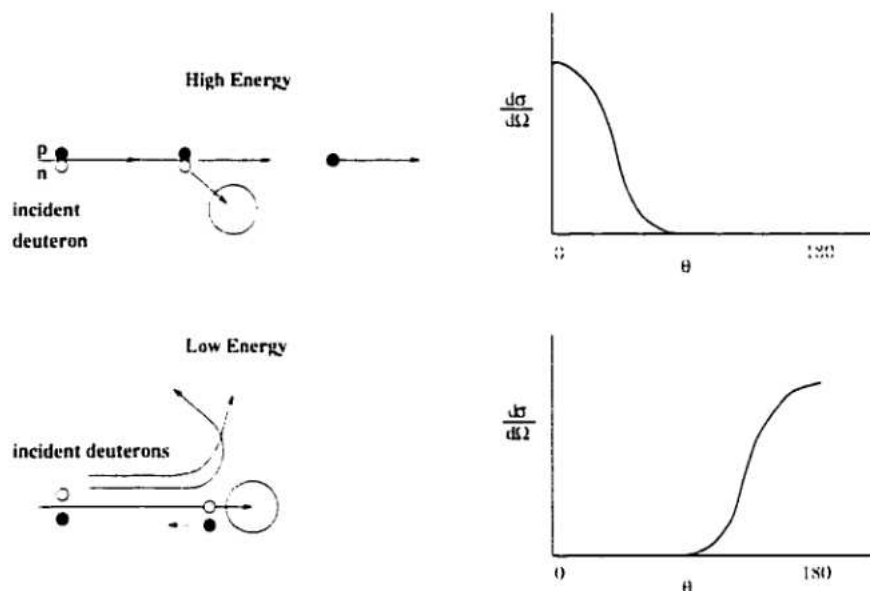
Figure 2.1: Deuteron stripping at high and low energy, giving angular distributions of the outgoing protons that are peaked in the forward and backward directions.

In the case of (d,p) reactions at low energies on heavy nuclei, the outgoing protons are backward-peaked, and this has a simple physical explanation. Deuterons with large impact parameters travel along Coulomb orbits that never get close enough to the target nucleus for a nuclear interaction to take place. Only those deuterons that make nearly head-on collisions get close enough and then, after the neutron has been captured, the proton is repelled back in the direction from which it came.

These two simple models of deuteron stripping are shown in Figure 2.1.

The (d,p) reaction is a powerful tool for the study of nuclear structure, allowing the identification the single-neutron strength in a nucleus. In a (d,p) reaction, the neutron is captured into a vacant single-particle state while the proton goes on alone.

29
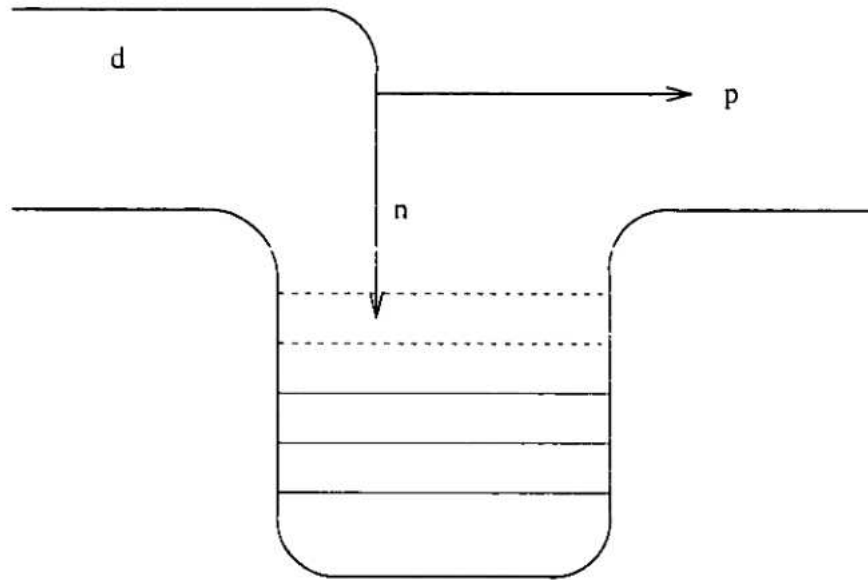
Figure 2.2: In a (d.p) reaction. the neutron is captured into an unoccupied single-particle state of the target nucleus.

as shown schematically in Figure 2.2. The energy of the outgoing proton gives the energy of the excited state of the residual nucleus. The angular distribution and the polarization of the proton give the spin and the parity of the state, and the absolute magnitude of the cross-section allows measurement of the *spectroscopic factor*. the single-particle occupation probability of the state in which the neutron is captured.

The analysis of (d.p) reaction data showed that the angular distributions of the outgoing protons can be divided into a few distinct classes. depending on the angle at which the cross-section has its maximum value. The kinematics of the reaction suggest that these classes correspond to reactions that transfer different amounts of orbital angular momenta $L = 0. 1\hbar. 2\hbar. ...$ to the target nucleus as shown in Figure

30

2.3.a. Let us suppose the energies of the incident deuteron and outgoing proton
are large enough to allow neglect of the effect of the Coulomb interaction on both
the incident deuteron and the outgoing proton. The incident deuteron has linear
momentum $\mathbf{k}_d$, the captured neutron carries to the nucleus a momentum $\mathbf{k}_n$ and the
proton is left with momentum $\mathbf{k}_p$. The absolute value of the angular momentum
carried by the neutron into the nucleus is given by $\hbar k_n b$ where b ranges from zero
to the radius R of the nucleus. Thus, the maximum transferred momentum is $\hbar k_n R$.
On the other hand the neutron is captured on an orbital of a defined orbital angular
momentum L so that

$$k_n R \geq L \qquad (2.1)$$

In the case of $L = 0$, Equation 2.1 is always satisfied and thus all angles of emission
are allowed. However, when the deuteron dissociates, the proton wave number $\mathbf{k}_p$
is always close to the direction of motion of the deuteron itself because the binding
energy E_B of the deuteron is usually less than its kinetic energy so that the internal
proton momentum ($\approx \sqrt{m E_B}$) is small with respect to its translational momentum.
Therefore, the angular distribution in this case is peaked in the forward direction
near θ. When L is greater than zero, Equation 2.1 cannot be satisfied for the small
angles of scattering corresponding to small values of k_n, as shown in Figure 2.3.b.
The angle of emission of the proton must thus increase to the value for which $R k_n = L$
before the reaction can occur. At this angle, for the same reason that emission was
most likely at zero degrees in the $L = 0$ case, the angular distribution will show a

31
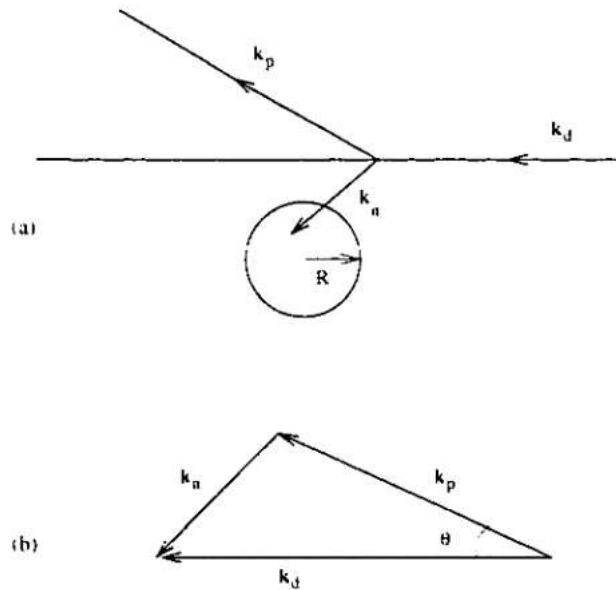
Figure 2.3: Schematic representation of a (d.p) reaction.

pronounced maximum. The experimental angular distributions satisfy this expectation (e.g. as shown in Figure 2.4 [*Macefield et al.*(1963)]). Thus. the shape of the angular distributions allows to determine the L-transfer in the reaction. Many target nuclei (including all even-Z-even-N nuclei) have $J = 0$. and for these the analysis is particularly simple. If the captured neutron has orbital angular momentum L. the total angular momentum of the final nuclear state in a (d.p) reaction. target + nucleon. is $\mathbf{J} = \mathbf{L} + \mathbf{1/2}$. so that $J = L \pm 1/2$. Thus knowledge of L gives two possible values of J. This ambiguity may be resolved by measuring the polarization of the outgoing proton. which is of opposite sign in the two cases. Furthermore. the product of the parities of the initial and final states is $(-)^L$. so if that of the initial state is known. that of the final state follows from knowledge of L.

32
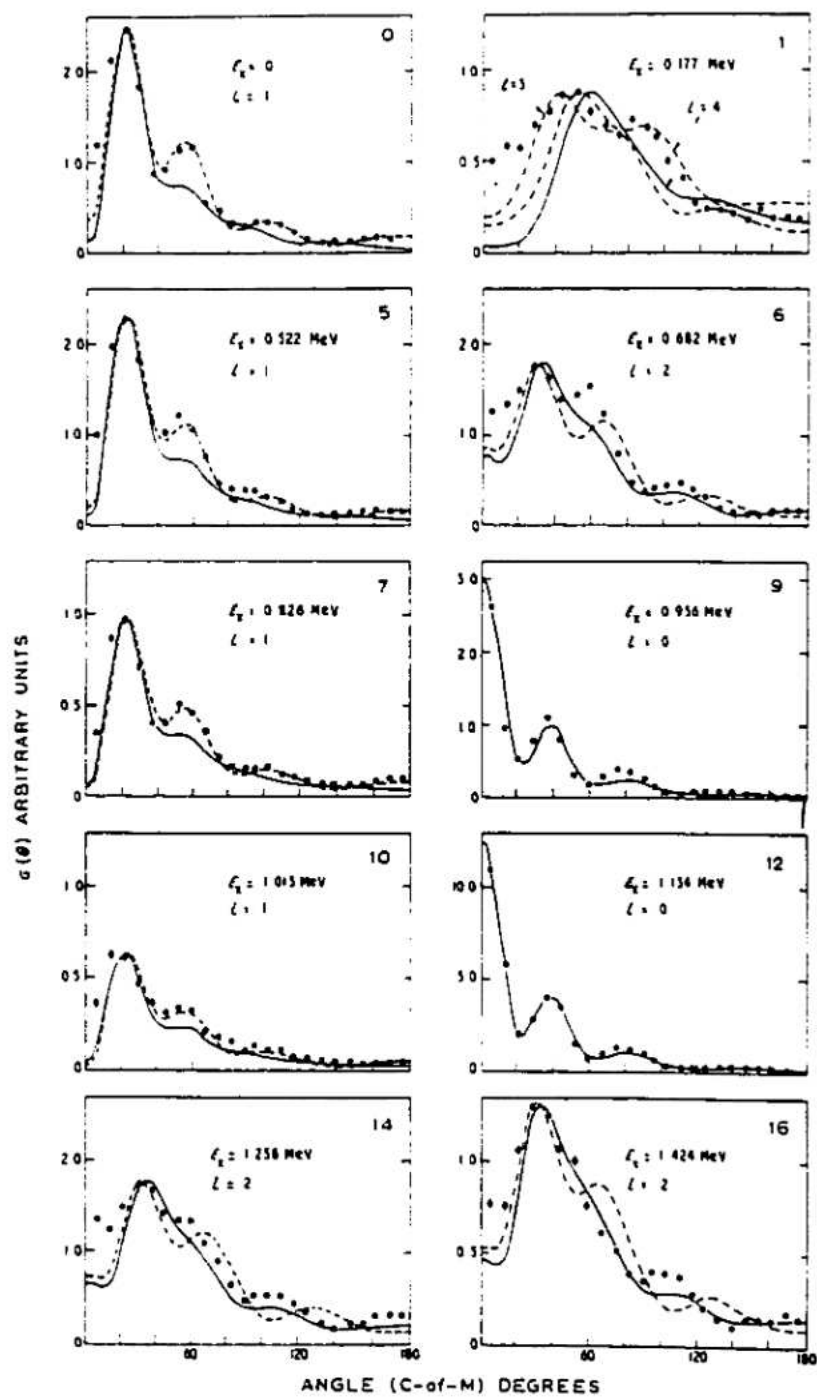
Figure 2.4: Angular distribution of the intense proton groups from the $Se^{76}(d,p)Se^{77}$. $E_d = 7.8$ MeV [Macefield (1963)].

33

2.3 The Theory of the Deuteron Stripping Reaction

The cross-section of non-elastic reactions may be calculated by expressing the to-
tal wavefunction as a sum of the wavefunctions in all the reaction channels, with
coefficients that depend on the structures of the corresponding nuclear states. If
this is inserted into the Schrödinger equation for the whole system, it gives a set of
coupled equations for the wavefunctions in all the channels and these may be solved
in principle if the interaction potential known.

The theory of the deuteron stripping reaction is described here in a very schematic
way to bring out the most important features. If the coupling between the initial
and the final channel is weak, the cross-section is given in terms of the square of the
matrix element of the perturbing interaction potential, and differential cross-section
for the transition from the initial state i to the final state f [Glendenning(1983)] is

$$\left(\frac{d\sigma}{d\Omega}\right)_{if} = \frac{m_f m_i k_f}{(2\pi\hbar^2)^2 k_i} \, |< f \mid V \mid i >|^2 \tag{2.2}$$

where $< f \mid V \mid i >$ is the matrix element, m_f and m_i are, the reduced masses,
and k_f and k_i are the wave numbers of the final and initial channels, respectively.
Speaking of spin angular momentum, the cross section is an average of the preceding
one over the initial angular momentum projections of J_d and J_T, and a sum over the
final states as follows

$$\frac{d\sigma}{d\Omega} = \frac{1}{(2J_d + 1)(2J_T + 1)} \sum_f \left(\frac{d\sigma}{d\Omega}\right)_{if} \tag{2.3}$$

34

Initial State   **Final State**
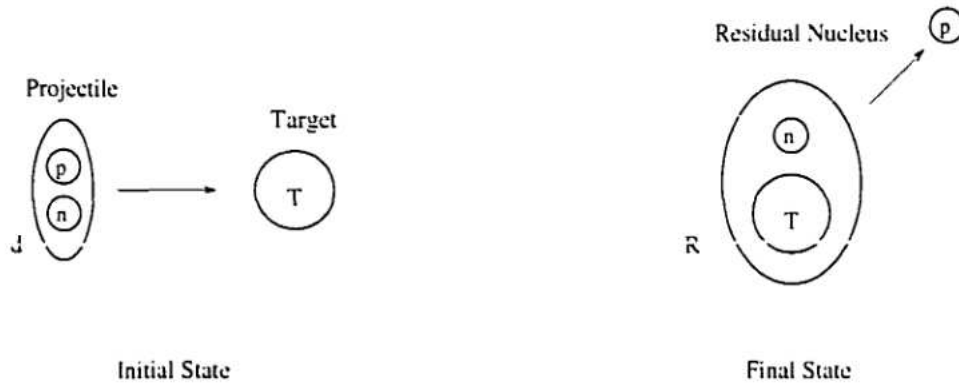
Figure 2.5: Schematic diagram of the (d.p) stripping reaction [Segre(1965)].

Schematically the initial and final states of the reaction may be represented by the diagram in Figure 2.5 [*Segre*(1965)]. So. the total Hamiltonian is

$$H = T_{dT} + T_{pn} + V_{pn} + V_{nT} + V_{pT} = T_{pR} + T_{nT} + V_{pn} + V_{nT} + V_{pT} \qquad (2.4)$$

[*Enge*(1966). *Glendenning*(1983), *Koonin and Mukerjee*(1990)]. where T_{dT} is the relative kinetic energy of the deuteron and target. and so on. The initial and final state Hamiltonians are

$$H_i = T_{dT} + T_{pn} + V_{pn} + \bar{V}_{dT} \qquad (2.5)$$

and

$$H_f = T_{pR} + T_{nT} + V_{nT} + \bar{V}_{pR} \qquad (2.6)$$

where the $\bar{V}$'s are optical potentials. Thus the perturbing Hamiltonian can be written in two ways. called the prior and post forms [*Enge*(1966). *Edwards et al.*(1973)]:

35

$$H'_{prior} = H - H_i = V_{nT} + V_{pT} - V_{dT} \tag{2.7}$$

and

$$H'_{post} = H - H_f = V_{pn} + V_{pT} - V_{pR} \tag{2.8}$$

The post form is used in (d.p) stripping calculations because

$$V_{pT} \approx V_{pR} \tag{2.9}$$

so that

$$H'_{post} \approx V_{pn} \tag{2.10}$$

Therefore the matrix element in Equation 2.2 can be written in the form

$$< \Phi_R \Psi_p(\mathbf{k}_p) \mid V_{pn} \mid \Psi_d(\mathbf{k}_d)\Phi_d\Phi_T > \tag{2.11}$$

where. $\Psi_d(\mathbf{k}_i)$ and $\Psi_p(\mathbf{k}_p)$ are the wavefunctions describing the motion of the incident deuteron and outgoing proton. respectively. Φ_d is the internal wavefunction of the deuteron. and Φ_T and Φ_R are the wavefunctions of the target and residual nuclei. respectively.

The wave function Φ_R can be expanded in terms of the wavefunctions of the target Φ_T and of the captured neutron $\Phi_n(J.L)$. For reactions on 0^+ targets. the neutron may be captured only into a state of definite J and L and

$$\Phi_R = \Theta_{JL}\Phi_T\Phi_n(J.L) \tag{2.12}$$

36

where Θ_{JL} is a spectroscopic amplitude [Austern(1970)]. Integrating over the target coordinates gives the matrix element in the form

$$< f \mid V \mid i >= \Theta_{JL} < \Psi_p \Phi_n \mid V_{pn} \mid \Phi_t \Psi_t > \tag{2.13}$$

and the cross section from Equation 2.2 is

$$\frac{d\sigma}{d\Omega} = \frac{m_d m_p k_p}{(2\pi \hbar^2)^2 k_d} S_{JL} F_{JL}(E.\theta) \tag{2.14}$$

[Glendenning(1983)], where m_p and m_d are the proton and the deuteron mass, respectively, and $S_{JL} = \Theta_{JL}^2$ is the spectroscopic factor. The spectroscopic factor measures the extent to which the state populated by a (d.p) reaction resembles a neutron in a single particle orbit coupled to the target nucleus. The function $F_{JL}(E.\theta)$ contains the energy and angular variation of the differential cross-section and is given by

$$F_{JL}(E.\theta) =|< \Psi_p \Phi_n \mid V_{pn} \mid \Phi_t \Psi_t >|^2 \tag{2.15}$$

This function can be evaluated numerically using deuteron and proton wavefunctions calculated from the corresponding optical potentials, and the neutron wavefunctions obtained from the shell model. It is a six-dimensional integral over the coordinates of the neutron and proton and it may be simplified to a good approximation by expressing the product $V_{pn}\Phi_d$ as a delta function.

$$V_{pn}(\mid r_p - r_n \mid)\Phi(\mid r_p - r_n \mid) = V_0\delta(r_p - r_n) \tag{2.16}$$

This reduces it to a three-dimensional integral. The angular integrations can be done analytically leaving a single radial integral to be done numerically. The value of

37

the constant V_0 is determined by analysing some stripping reactions to states known to have a pure single-particle structure. The theory takes account of the distortion of the incident and outgoing waves, so is called the distorted wave theory. The Equation 2.13 enables the theory to be tested by comparison with experimental data. If the transferred L-value is not known, the cross-sections are calculated for several assumed values, and it is usually found that one fits much better than the others, thus determining L. Normalizing the calculated cross-section to the experimental cross-section then gives the spectroscopic factor S_{JL}.

CHAPTER 3

Distorted-Wave Born Approximation Code: DWUCK4

3.1 Introduction

Direct nuclear reactions are caused by an interaction that induces a transition between two channels. In each channel the relative motion is described by an optical potential. which describes the average field experienced by the colliding nuclei. In this chapter. an approximation of the transition amplitude that corresponds to this interpretation is discussed. The approximate transition amplitude. involving as it does the distortion (from plane waves) of the wave function of relative motion in incident and outgoing channels. is known as distorted-wave Born approximation (DWBA) amplitude. which is the most useful in direct nuclear reaction theory and the interpretation of experimental data.

The DWBA calculations were performed using an extended version (DWUCK4) of the code DWUCK by Kunz (1979). and it is described in its manual as follows.

39

3.2 General Description of DWUCK

The computer program DWUCK calculates the scattering differential cross section within the DWBA. The incoming and outgoing waves may be in any combination of spin 0, spin 1/2, or spin 1 particles. The spin dependent parts of the optical potentials for distorted waves are diagonal in the total and orbital angular momentum [Glendenning(1983), Satchler(1983)]. The calculations are performed in a zero range form between the coordinates of the incoming and outgoing waves. Particle transfer reactions can be treated with this program using a local energy approximation to correct for finite range effects.

The DWBA computer code DWUCK calculates a transition amplitude for the reaction A(a,b)B of the form [Austern(1970), Glendenning(1983)]

$$ T = J \int dr_f \int dr_i \chi_f^{-*}(\mathbf{k}_f, \mathbf{r}_f) \langle bB|V|aA \rangle \chi_i^{+}(\mathbf{k}_i, \mathbf{r}_i) \qquad (3.1) $$

where, k_f and k_i are the relative momenta, χ_f^{-} and χ_i^{+} are the distorted waves in the final and initial channels, respectively, $\mathbf{r}_i$ and $\mathbf{r}_f$ are the relative coordinates for the systems (a,A) and (b,B) respectively and J is the Jacobian of the transformation from R and ρ to $\mathbf{r}_i$ and $\mathbf{r}_f$ coordinates, as indicated in Figure 3.1. The quantity $< bB \mid V \mid aA >$ is the form factor for the reaction and contains a delta function (the zero range approximation) for the coordinates $\mathbf{r}_i$ and $\mathbf{r}_f$. The distorted wave χ_i^{+} describes asymptotically a plane wave of momentum k plus an outgoing (+) (or incoming (-)) wave which in the case of no Coulomb potential has the form

40
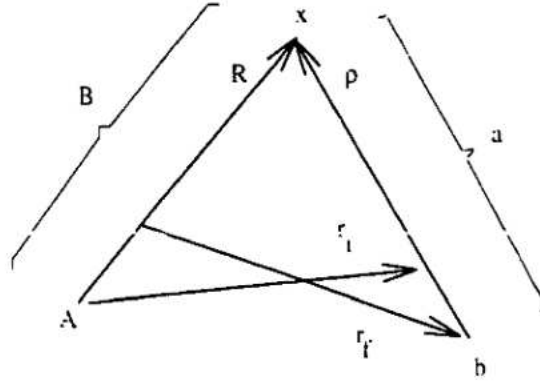
Figure 3.1: Coordinate relations for a transfer reaction of x nucleons. The channel coordinates $\mathbf{r}_i$ and $\mathbf{r}_f$ connect the CM's of A and a, and B and b, respectively, whereas $\mathbf{R}$ and ρ connect the CM's of A and x, and b and x, respectively. [Glendenning(1983)]

[Glendenning(1983)]

$$\chi^{\pm}(\mathbf{k}.\mathbf{r}) \longrightarrow e^{i\mathbf{k}.\mathbf{r}} + f(\theta)\frac{e^{\pm ikr}}{r} \tag{3.2}$$

where $f(\theta)$ is the scattering amplitude. The final state distorted wave, which has an incoming scattered wave, is related to the solution with outgoing waves by time reversal [Austern(1970), Glendenning(1983)]

$$\chi^{-*}(\mathbf{k}.\mathbf{r}) = \chi^{+}(-\mathbf{k}.\mathbf{r}) \tag{3.3}$$

When the particles a and b have spin, the functions $\chi^{\pm}$ become matrices in spin space $\chi^{\pm}_{m'm}$. The relevant time reversal condition is

$$\chi^{-*}_{m',-m}(\mathbf{k}.\mathbf{r}) = (-)^{m-m'}\chi^{\pm}_{-m',m}(-\mathbf{k}.\mathbf{r}) \tag{3.4}$$

The distorted waves $\chi_{m'm}(k.r)$ can be written as

$$\chi^{\pm}_{m'm}(\mathbf{k}.\mathbf{r}) = \frac{\sqrt{4\pi}}{kr}\sum_{JL} i^{L}\sqrt{2L+1}\,\chi_{JLs}(\mathbf{k}.\mathbf{r})\,\langle LsMm|JM'\rangle$$

41

$$\langle Ls\ M' - m l\ m l | J M' \rangle\ Y_L^{M'-m'}(\mathbf{r})\ d^L_{\, M'-m'} \qquad (3.5)$$

The $d^L_{\, m}$ are the rotation functions for integer spin [*Edmonds* (1974)]. The radial part of the distorted waves satisfies the equation.

$$\left[\frac{d^2}{dr^2} + k^2 - \frac{L(L+1)}{r^2} - \frac{2\mu}{\hbar^2}(U(r) + U_c(r) + U_{Ls}(r)\mathbf{L.s}) \right] \chi_{JLs}(\mathbf{k.r}) = 0 \qquad (3.6)$$

where U is a central potential with real and imaginary parts. U_c is a Coulomb potential for a uniform charge distribution of radius R_c, and U_{Ls} is a spin orbit potential. The radial functions $\chi_{JLs}(\mathbf{k.r})$ satisfy the boundary conditions $\chi_{JLs}(k,0) = 0$ at the origin, and

$$\chi_{JL}(\mathbf{k,r}) \longrightarrow \frac{\left[H_L^-(kr) - \eta_L^J H_L^+(kr) \right]\ e^{i\sigma_L}}{2i} \qquad (3.7)$$

for large r. Here $H_L^\pm(kr) = G_L \pm iF_i$ is the outgoing and incoming wave Coulomb function. η_L^J is the reflection coefficient, and σ_L is the Coulomb phase shift. The functions χ_{JL} are computed by numerically integrating the differential equations to a value of r. The χ_{JL} are then matched to the Coulomb functions G_L and F_L at the last two integration points to determine η_L^J and the overall normalization constants.

The factor $< bB \mid V \mid aA >$, which contains the nuclear structure information, is expressed as [*Austern*(1970)]

$$\begin{aligned}
\langle J_B M_B\ s_b m_b | V | J_A M_A\ s_a m_a \rangle &= \sum_{lsj} B_{lsj} \langle J_A j\ M_A\ M_B - M_A | J_B M_B \rangle \\
&\quad \langle s_a s\ m_b\ m_a - m_b | s_a m_a \rangle \\
&\quad \langle ls\ m\ m_a - m_b | j\ M_B - M_A \rangle \\
&\quad f_{lsj}(r_c)\delta(\mathbf{r}_f - \frac{A}{B}\mathbf{r}_i)\ i^{-l}\ Y_l^m(\mathbf{r}_i)^*. \qquad (3.8)
\end{aligned}$$

42

where Y_l^m is a spherical harmonic. The quantity B_{lsj} is a measure of the strength of the interaction and is equal to $\sqrt{(2s+1)/2s_a + 1} A_{lsj}$ where A_{lsj} is the spectroscopic coefficient used in DWUCK4. The function f_{lsj} is the radial form factor for the reaction. In this equation above, the angular momenta must satisfy.

$$\mathbf{j} = \mathbf{J}_B - \mathbf{J}_A, \quad \mathbf{s} = \mathbf{s}_a - \mathbf{s}_b, \quad \mathbf{l} = \mathbf{j} - \mathbf{s}.$$

With the definitions of $<bB \mid V \mid aA>$ and the distorted waves $\chi_{m'm}^{\pm}(kr)$, the transition amplitude can be written as

$$T^{M_A M_B; m_a m_b} = \frac{\sqrt{4\pi}}{k_a k_b} \sum_{l,s,j} \sqrt{2l+1} \, B_{lsj} \, \langle J_A j \, M_A \, M_B - M_A | J_B M_B \rangle \, S_{lsj}^{m m_a m_b}. \qquad (3.9)$$

where the angle dependent amplitude S can be written as

$$S_{lsj}^{m m_a m_b} = \sum_{L_b} \beta_{lsj:L_b}^{m m_a m_b} P_{L_b}^{m_a - m - m_b}. \qquad (3.10)$$

where $P_{L_b}^{m_a - m - m_b}$ is an associated Legendre polynomial. The amplitude β is given by

$$
\begin{aligned}
\beta_{lsj:L_b}^{m m_a m_b} = \sum_{J_a L_a J_b m} & \langle L_a s_a \, 0 m_a | J_a m_a \rangle \\
& \langle L_b s_b \, m_a - m - m_b \, m_b | J_b m_a - m \rangle \langle J_b j \, m_a - m \, m | J_a m_a \rangle \\
& (2L_b + 1) \langle L_b l \, 00 | L_a 0 \rangle \sqrt{(2s_a+1)(2j+1)(2J_b+1)(2L_a+1)} \\
& \begin{Bmatrix} L_b & s_b & J_b \\ l & s & j \\ L_a & s_a & J_a \end{Bmatrix} I_{J_a L_a J_b L_b}^{lsj} i^{L_a - L_b - l}
\end{aligned} \qquad (3.11)
$$

In the above expression the usual nine$-j$ symbol, $\{\ \}$ [Edmonds (1974)]. appears.

43

The radial integrals are defined as

$$I_{J_a l_a J_b i_b}^{l s_J} = \frac{CB}{A^2} \int dr_i \, \backslash \bar{j}_{J_i L_b}(k_f \cdot \frac{A}{B} r_i) \, f_{l s_J}(r_i) \, \backslash \dagger_{J_a L_a}(k_i \cdot r_i)$$ (3.12)

where C is the mass of the form factor core.

The differential cross section for the $A(a,b)B$ reaction is defined in terms of T by

$$\begin{aligned}
\frac{d\sigma}{d\Omega} &= \frac{\mu_a \mu_b}{(2\pi\hbar^2)^2} \frac{k_f}{k_i} \frac{1}{2J_A + 1} \frac{1}{2s_a + 1} \sum_{M_A M_B m_a m_b} |T^{M_A M_B; m_a m_b}|^2 \\
&= \frac{1}{4\pi} \frac{2J_A + 1}{2J_B + 1} \frac{1}{E_i E_f} \frac{k_b}{k_a} \frac{1}{2s_a + 1} \\
&\qquad \sum_{m_a m_b m} \left| \sum_{l s_J} \sqrt{2l + 1} \, \beta_{l s_J} S_{l s_J}^{m m_a m_b} \right|^2 .
\end{aligned}$$ (3.13)

where E_i and E_f are the center of mass energies for the entrance and exit channels respectively.

The program DWUCK computes the cross sections with the appropriate normalization. The normalizations result from the zero range approximation, so depend on the specific type of reaction. The cross section predicted by DWUCK for a (d,p) reaction is

$$\frac{d\sigma_{DW}^{l s_J}(\theta)}{d\Omega} = \frac{1}{4\pi} \frac{1}{E_i E_f} \frac{k_f}{k_i} \frac{1.0 \times 10^4}{2s_a + 1} \sum_{m_a m_b m} \left| \sum_{l s_J} \sqrt{2l + 1} \, S_{l s_J}^{m m_a m_b} \right|^2 .$$ (3.14)

in units of $fm^2/ster$ ($1 fm^2 = 10 mb = 10^{-26} cm^2$). Therefore the cross section is

$$\frac{d\sigma^{l s_J}(\theta)}{d\Omega} = \frac{2J_B + 1}{2J_A + 1} \frac{1}{2j + 1} \frac{|B_{l s_J}|^2}{1.0 \times 10^4} \frac{d\sigma_{DW}^{l s_J}(\theta)}{d\Omega} .$$ (3.15)

44

CHAPTER 4

Experimental Procedure

This experiment was carried out in inverse kinematics at the projectile fragmentation type radioactive beam facility of the National Superconducting Cyclotron Laboratory (NSCL) at the Michigan State University (MSU). The NSCL is a national user facility devoted primarily to basic research in nuclear science as well as accelerator and instrumental research and development. With the K1200 and K500 cyclotrons, experiments with beams proton to Uranium and energies of 20 to 200 MeV per nucleon are possible [NSCL(1999)a]. In addition, the A1200 beam analysis device for the K1200 cyclotron is able to measure and define precisely the beam energy, and thereby produce separated radioactive beams which can be transported to any experimental device. A layout of the facility, showing the position for the S800 spectrometer, which is used for this study, is given in Figure 4.1.

4.1 Beam and Target

A secondary beam of ^{15}C was produced in the A1200 fragment separator (Figure 4.2) at the NSCL using a primary beam of ^{18}O at 55 MeV per nucleon incident on

45
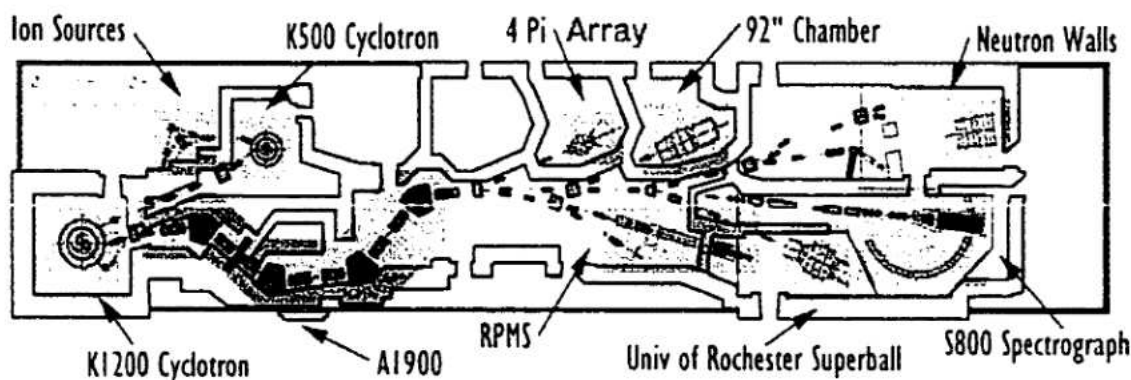
Figure 4.1: Floor plan of the NSCL showing the beam distribution system to allow experiments with the K1200 and K500 [NSCL(1999)b].

a ^{9}Be production target with thickness 190 mg/cm^2. A thick polyethylene wedge (200 mg/cm^2) was used at the second dispersive image of the A1200. This wedge was able to degrade the secondary beam energy to 20 MeV per nucleon and allow the strong ^{17}N contaminant to be removed from the secondary beam by using the extended focal plane slit of the A1200. The computer code INTENSITY predicted, by the MSU group, a secondary beam intensity of 10^4 particles per second with 98% purity for a primary beam current of 55 pnA with this target and wedge. The resulting secondary beam of ^{15}C was transported to the S800 spectrometer where the experiment was performed.

Multiwire proportional counters were used to measure the energy and trajectory of each incoming ^{15}C. The secondary beam was then focussed onto CD_2 target of thickness 1.94 mg/cm^2. The S800 spectrometer (Figure 4.3) was used to measure

46

the energy of the ^{16}C ejectiles. and an array of position sensitive proton detectors was used to detect the protons. It is necessary to detect the protons in order to reconstruct the scattering angle in the centre of mass.

4.2 The A1200 Radioactive Beam Facility

The secondary radioactive beams can be produced by the A1200 (Figure 4.2) either by fragmentation-like reactions at high energy or by direct reactions with large cross sections at lower energies [NSCL(1997)]. The latter mechanism offers the advantage of limited beam energy spread in the secondary beams. A degrader wedge can be inserted at *Image* #2 to purify the secondary beams.

The A1200 device immediately follows the K1200 cyclotron. allowing radioactive beams to be delivered to all the experimental vaults. as seen in Figure 4.1.

4.3 The K1200 Cyclotron

The K1200 cyclotron. which was used for this study. provides the particle beams for the nuclear science research at the NSCL. The cyclotron can accelerate ions of any element [NSCL(1999)a]. The beam energy can be selected within the range from 20 MeV/nucleon to 200 MeV/nucleon. The radio frequency (rf) system provides the accelerating potential: its frequency range. which corresponds to energy per nucleon mentioned above. is 9 MHz to 26.5 MHz. The magnet provides an azimuthally

47

Dispersive Image #1

Final
Achromatic
Image

Target

Dispersive Image #2

Beam from
K1200 Cyclotron
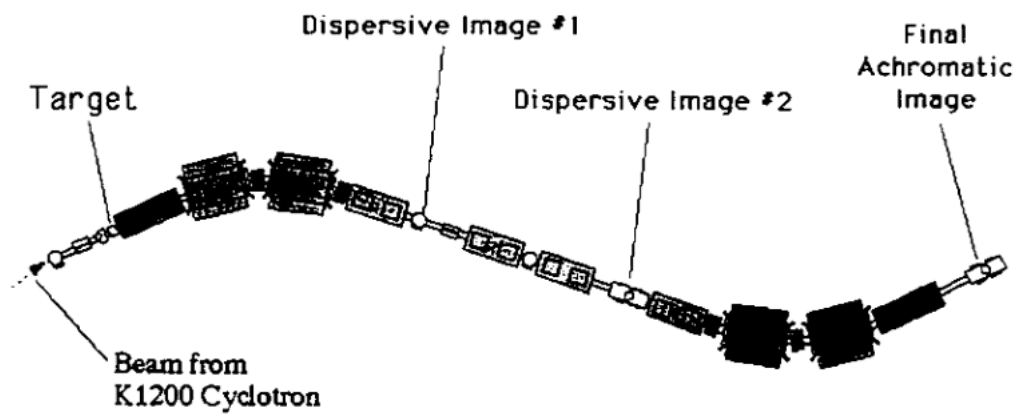
Figure 4.2: A1200 Radioactive Beam Facility of the MSU [*NSCL*(1997)].

48

varying field whose average value at the extraction radius of 1 m is between 3 and 5 Tesla.

The useful beam intensity ranges from about 10^{12} particles/second down to approximately 100 particles/second. The cyclotron usually accelerates single atoms, but it also works with molecules. e.g. H_3^+ is accelerated to provide protons. The particles are fed continuously from the electron cyclotron resonance (ECR) ion source to the center axis of the cyclotron and are delivered as a continuous beam from the accelerator. As they leave the ion source, the particles are accelerated by a DC voltage of 7 to 20 kV and are transported to the midplane the cyclotron. They follow a spiral path inside as they gain energy from the rf system, making approximately 700 to 800 turns and traveling about 3 km.

4.4 The ECR Ion Source

The purpose of the electron cyclotron resonance (ECR) ion source is to produce highly-charged positive ions and send them down a beam pipe to be injected into the cyclotron for acceleration. In an ECR ion source, a plasma of the element of interest is held in a magnetic bottle that is long enough for element atoms to be ionized in collisions with electrons. The magnetic bottle is shaped by circular coils at its top and bottom and hexapole magnet around the sides, three north poles alternating with three south poles [NSCL(2000)]. The transmitters for the microwaves that heat the electrons run at several times the frequency of a household microwave oven. A gas of the element enters at the top of the bottle and gradually leaks out as ions at

49
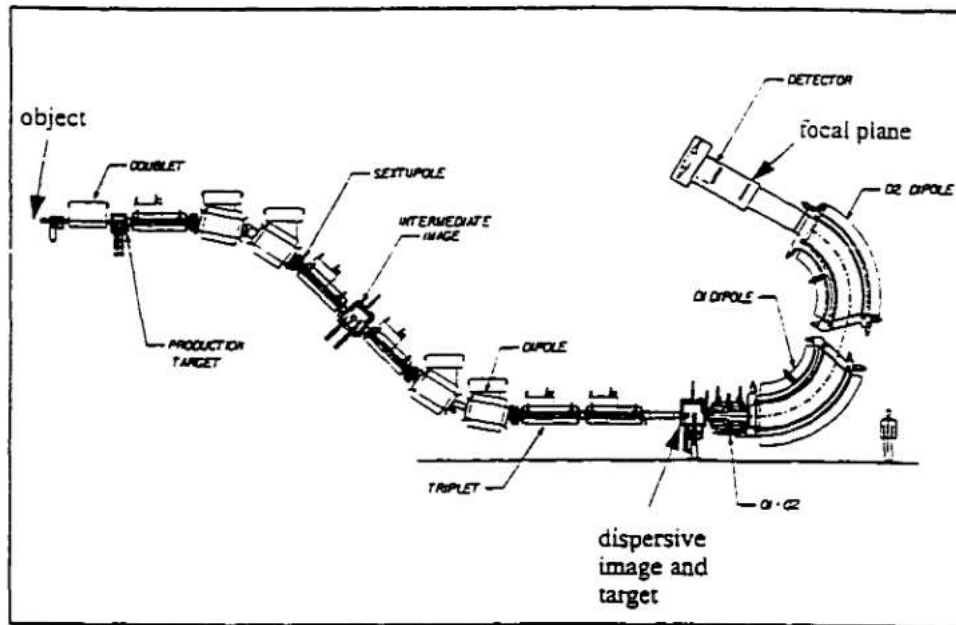
Figure 4.3: S800 Beam Line and Spectrometer at the MSU [Sherrill(1999)].

the bottom, from which point it is sent to the cyclotron. Metals and the other solid element can be heated to the gaseous stage in a very tiny oven [NSCL(2000)].

4.5   The S800 Beam Line and Spectrometer

The S800 analysis beam line, from the object to target chamber, and spectrometer is schematically shown in Figure 4.3. The analysis line is very similar to the A1200 fragment separator [Sherrill et al.(1992)], but with better resolution and larger solid angle acceptance. The S800 has a design energy resolution $E/\Delta E$ of 10^4 for the entire 20 msr solid angle [Yurkon et al.(1997), Zhang(1997), Sherrill(1999)]. Table

50
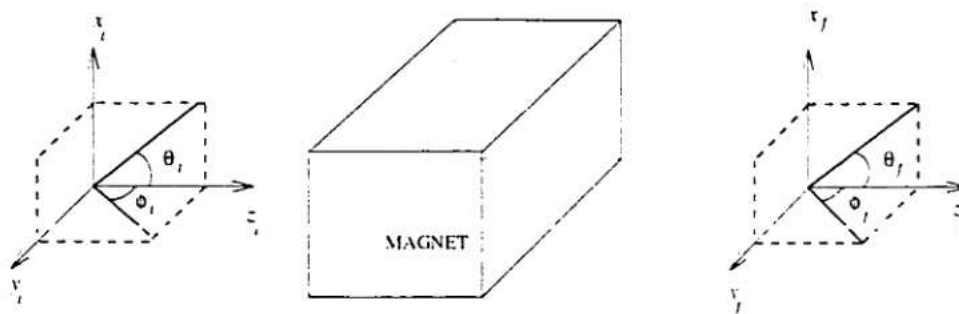
Figure 4.4: Schematic of the optical coordinate system before and after a magnet.

4.1 summarizes the design goals and physical parameters of the S800 spectrometer [Zeller et al.(1994). Caggiano(1995). Zhang(1997). Caggiano(1999)].

The beam line consists of four 22.5° dipoles. five quadrupole triplets. four sextupoles and one quadrupole doublet [Sanderson(1995). Zhang(1997)]. The "object" [Caggiano(1999)] position is the production target when radioactive beams are transferred in the analysis line. The intermediate image has a focus in x and y (the coordinate system is illustrated in Figure 4.4). and a dispersion of 1.5 cm/%. here % is the unit of the deviation in momentum $\delta = \Delta p/p_0$. There is also a focus in x and y at the target position. but the dispersion is very high. about 12 cm/% [Zhang(1997). Caggiano(1999)].

The beam line quadrupole triplets are described in detail in [Zhang(1997)]. The triplets are capable of maximum field gradients of 35 T/m and maximum currents of 100 Amperes. Each triplet weighs 5 tons.

51

Energy resolution. $\Delta E/E$	10^{-4}
Momentum resolution. $\Delta P/P$	5×10^{-5}
Energy range	11.6 %
Momentum range	5.8 %
Solid angle	20 msr
Angular resolution	2 mrad
Vertical dispersion (x/δ)	9.5 cm/%
Horizontal dispersion (y/ϕ)	0.9 mm/mrad
Magnification (x/x)	0.74
Focal Plane tilt	28.5°
Focal plane size	30 cm x 59 cm
Maximum dipole field	1.6 Tesla
Maximum rigidity $(B\rho)$	4.0 T-m
Dipole bend angle	75°
Dipole bend radius	2.8 m

Table 4.1: Parameters of the S800 Spectrometer

The spectrometer system chosen for the S800 is a QQDD configuration. where Q and D refer quadrupoles and dipoles. respectively. The parameters of the superconducting spectrometer dipole magnets. D1 and D2. are given in Table 4.2 [*Zeller et al.*(1994). *Caggiano*(1995). *Zhang*(1997). *Caggiano*(1999)]. The bend radii of the dipoles are 2.8 meters. and their bend angles are 75°. Ions are defocused in the x direction while focused in the y direction by means of the 30 degree edge angles on the dipole steel. The dipole power supplies deliver up to 450 Amperes to the coil. and the maximum central field is 1.6 Tesla. The dipoles weigh 70 Tons each.

Quadrupole magnets are the primary focusing elements in an accelerator beam line. The design for the high resolution spectrometer at the NSCL required two

Max. central field	1.6 Tesla
Max. current	150 Amperes
Dipole bend radius	2.8 m
Dipole bend angle	75°
Dipole entrance angle	D1: 0°; D2: 30°
Dipole exit angle	D1: -30°; D2: 0°
Weight	70 Tons

Table 4.2: Features of the D1 and D2 magnets

Max. field gradient	Q1: 19.7 T/m; Q2: 7.5 T/m
Max. current	Q1: 85 A; Q2: 100 A
Pole diameter	Q1: 24 cm; Q2: 12 cm
Length of pole tips	Q1: 30 cm; Q2: 30 cm
Weight	5 Tons

Table 4.3: Features of the Q1 and Q2 magnets

53

quadrupole magnets. Q1 and Q2 whose parameters are summarized in Table 4.3 [*Zeller et al.*(1994). *Caggiano*(1995). *Zhang*(1997). *Caggiano*(1999)]. The design of the quadrupole doublet is described in detail in [*Zhang*(1997)]. The doublet focuses in the y direction first. then the x direction to maximize the acceptance of the spectrometer.

4.6   The S800 Focal Plane Detectors

The S800 spectrometer is a high resolution. wide acceptance magnetic device for charged particle spectroscopy that requires high resolution performance from its focal plane detectors. Features of the S800 spectrometer that are relevant to the design of the focal plane are summarized in Table 4.1. The focal plane detector array for the S800 consists of six detectors as shown in Figure 4.5 [*Yurkon et al.*(1997)]. First are two Cathode Readout Drift Counters (CRDC). separated by one meter. These are immediately followed by an ionization chamber. Behind the ion chamber there is a stack of three scintillators. The detector system and electronics are described in detail in [*Yurkon et al.*(1994). *Yurkon et al.*(1996). *Yurkon et al.*(1997). *Caggiano*(1999)].

The positions of the particles in the focal plane are measured in the x and y directions by means of the two CRDC's. From the positions in the two detectors. the particle optical angles θ and o (as seen in Figure 4.4) in the focal plane are obtained. The CRDC's have an active area of 30 cm x 59 cm and an active depth of 1.5 cm. The particles are dispersed in momentum along the 59 cm direction. that

54
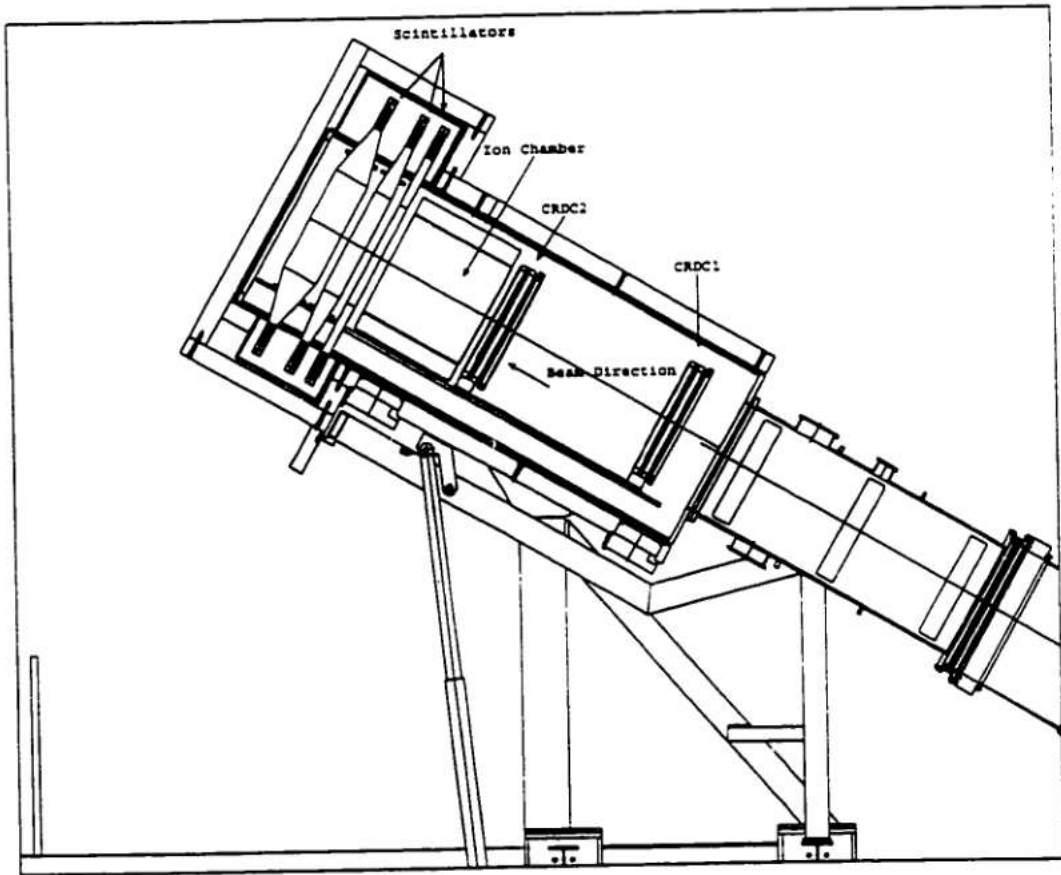
Figure 4.5: The S800 focal plane [*Yurkon et al.*(1997)].

55

is along the x direction or in other words radial direction in the dipole magnets. The principle of the operation of CRDC's is schematicly described in Figure 4.6. The CRDC is filled with a gas of 140 Torr of 80% CF_4 and 20% C_4H_{10}. Particles travel through the gas and create ions. In a electric field in the counter, the electrons produced in the ionization move toward an anode wire, where charge amplification takes place in the high electric field close to the wire. The anode wire is located below a grounded Frisch grid and held at a constant voltage. The cathode pads are placed behind and in the front of the anode wire. The electrons are collected on the anode wire, and then a positive charge is produced on the cathode pads by being induced by the charge collected on the anode wire. After each pad is individually read, a Gaussian fit is performed to the charge distribution, and the centroid is taken as the dispersive position in the focal plane.

The drift time of the electrons to the anode wire in the CRDC's is measured to determine the y position of the particle, that is, in the transverse direction. Depending on the distance between the particle that creates the ionization and the anode wire, the typical drift time of the electrons to the anode wire ranges up to 20 μs. The time between the anode wire signal and the scintillator signal is measured to obtain a direct y (transverse) position in the plane. The fast response of the scintillator is advantageous for timing the electron drift to the anode wire in the CRDC's.

The ionization chamber used in the S800 focal plane is a standard Frisch gridded ion chamber that is segmented into 16 one inch anodes perpendicular to the path of the ions. The detector gas is 300 Torr of P_{10}, which is a mixture of 90% Argon and

56
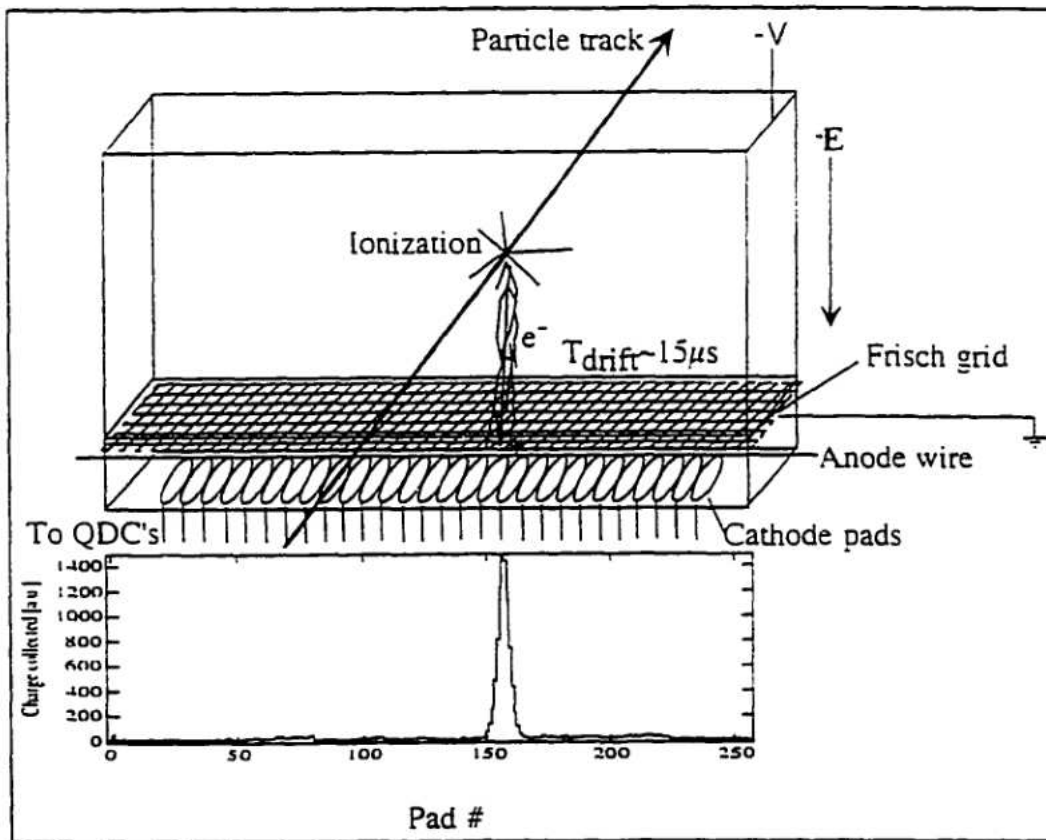
Figure 4.6: The schematic of the Cathode Readout Drift Counter (CRDC) operation [*Caggiano*(1999)].

10% Methane (CH_4). Energy loss measurement is done in the ionization chamber for particle identification. Ionization chambers operate in a way similar to that of a CRDC. They have a gas region between two parallel plates with a voltage applied across them. Charged particles entering the chamber produce ion pairs which drift towards the electrons. The output signal is proportional to the particle energy dissipated in the detector: therefore measurement of particle energy is possible.

The scintillator detectors with 5 cm, 10 cm, and 20 cm thickness are closely coupled with the ionization chamber and provide energy loss, total energy, and timing information. The 5 cm scintillator that is behind the ionization chamber stopped all ions from the reactions in this study, and it provided the master gate for the data acquisition electronics and a total energy measurement for particle identification. The general principle of scintillation counting depends on interaction of the incident particle with a suitable fluorescent material. The scintillator is a piece of plastic that is designed to scintillate when particles strike it. There are light guides mounted on each end to collect the light in the photomultiplier tubes. The light collection time is the order of nanoseconds from the scintillator. The amount of light collected in the scintillator is a function of the ion's atomic number, mass, and total energy.

4.7 Proton Detectors

Due to the reaction kinematics, the angle of the residual ^{16}C nuclei cannot be detected easily, since the maximum scattering angle is about 5^0 with ^{15}C beam energy about 300 MeV. However, the protons can be detected with a very high

58
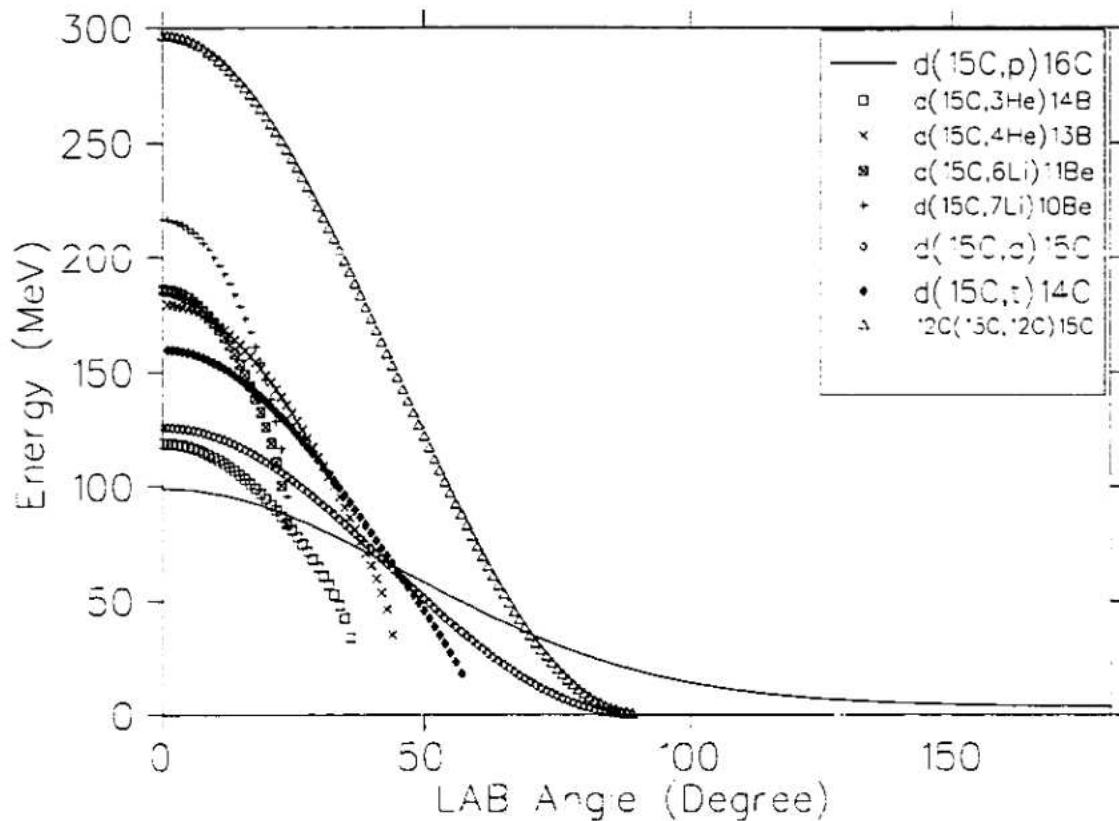
Figure 4.7: Energies of the Ejectile Particles versus the Laboratory Angles

range of angles. Contaminant reactions that can take place on deuterium are e.g. $^2H(^{15}C,^2H)^{15}C$, $^2H(^{15}C,^3He)^{14}B$, $^2H(^{15}C,^4He)^{13}B$, $^2H(^{15}C,^3H)^{14}C$, $^2H(^{15}C,^6Li)^{11}Be$, and $^2H(^{15}C,^7Li)^{10}Be$. In addition, backscattering of the ^{12}C from CD_2 target foil can occur. Figure 4.7 shows the energy of the above listed reactions as a function of the proton laboratory angle for a ^{15}C beam energy of 300 MeV. While the heavy residual nuclei of the contaminant reactions are all strongly forward peaked, the light charged ejectiles cover a considerable angular range.

59

Since studies of the kinematics predicted that a detector at back angles would only see protons. position sensitive Si-detectors mounted at back angles in the target chamber observed protons in inverse kinematics. as seen in Figure 4.8. This corresponds to forward angles for the protons in the centre of mass. Each of the disc shaped detectors. which have thus been called CD detectors. has 16 rings and sectors. each of the rectangular detectors called strip detectors has 16 3.14 mm strips. Figure 4.10 and 4.11 show the top and the front. looking at the beam. views of the strip detectors. and 4.9 shows the front view of a CD detector.

60
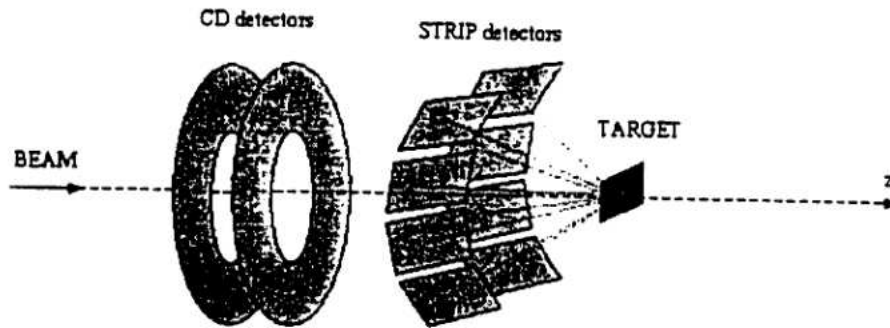
Figure 4.8: Si proton detectors. CD and Strip
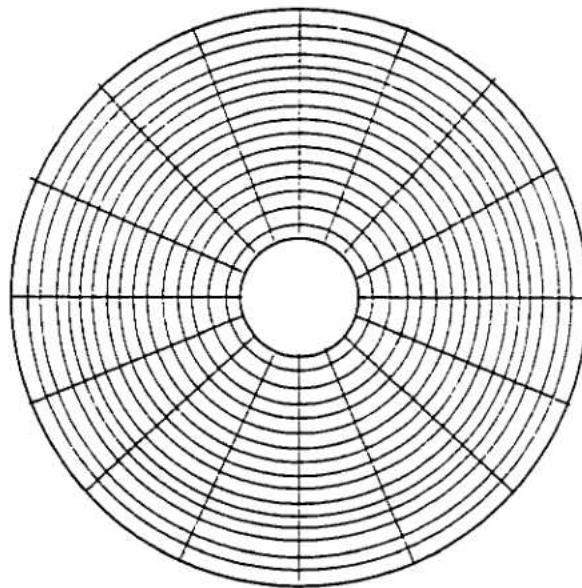
Figure 4.9: Front view of a CD detector, looking into the beam

61
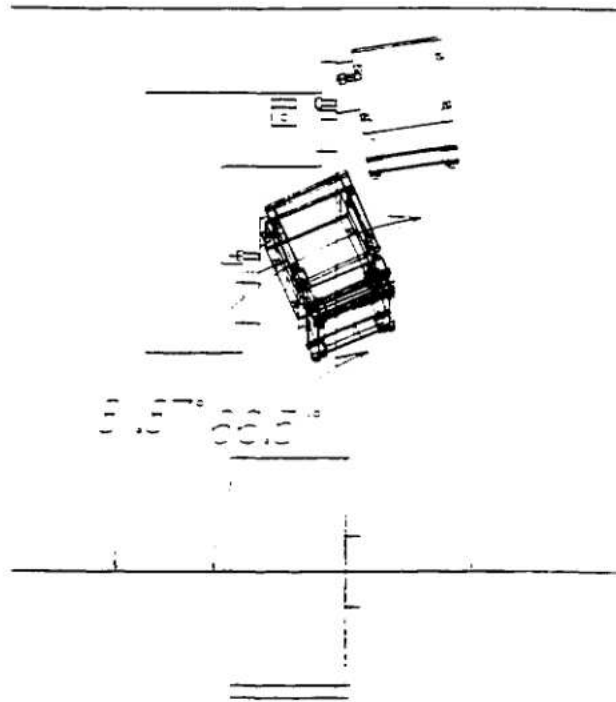
Figure 4.10: Top views of the Strip Detectors
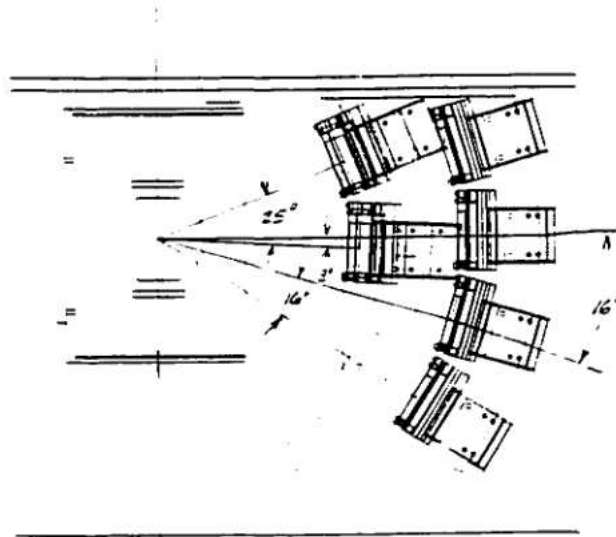
Figure 4.11: Front views of the Strip Detectors. looking into the beam

62

CHAPTER 5

Data Analysis

5.1 CRDC Calibration

5.1.1 Pulser Calibration

As described in section 4.6, the position, on the focal plane, of the particles going through the CRDC (Cathode Readout Drift Counter) is determined via the induced charge distribution generated by ions passing through the chamber. Thus, a moving charged particle should induce the same charge on each pad, and correspond to the same channel in the QDC (Charge to Digital Converter). However, the combined effects of this being a statistical process and the electronics associated with each channel having slightly different calibrations, required that a correction be made on the CRDC for each pad to give the same response to the same charge induced. This was achieved by depositing identical charges on all the pads simultaneously with a high precision pulser, and then re-calibrating the observed QDC pulse hight. The charge deposited by the pulser was increased by a known amount to explore the linearity of the electronics. It was found that a single linear relationship would

63

suffice to ensure a good correlation between all the CRDC channels. Figure 5.1 and Figure 5.2 show that the charge distribution on three pads caused by the two pulsers before and after the calibration, respectively. Figure 5.3 shows the charge distribution on all pads produced from one pulse before and after the calibration.

Several methods for determining the position of the track were investigated [*Yurkon et al.*(1994), *Bazin*(1998)]. The Simple center of gravity of all the pads, the center of gravity of several pads around the peak, and a Gaussian fit of the charge distribution were compared. The resolution was improved by fitting the charge distribution on the pads to a gaussian over a limited number of pads. It is thought that this improvement results because this ignores the somewhat random tails of the distributions. Figure 5.4 shows an induced charge distribution measured on the pads for a particle through a CRDC.

For the real data, after each calibrated pad was individually read, a Gaussian fit was performed to the charge distribution, and the centroid was taken as the position in the focal plane.

5.1.2 Position Calibration

In order to calibrate the detector positions, masks with defined holes were placed in front of the CRDC's and illuminated with beam particles. The position calibration in the dispersive direction did not need to be done since it was well known that the CRDC cathode pads are separated by 2.54 mm and fixed in position. The optical center of the detectors is provided by the beam axis hole. The position calibration

64
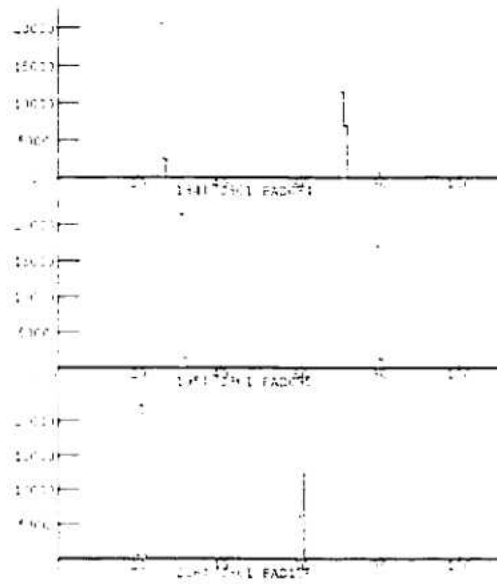
Figure 5.1: Charge distribution on three pads of CRDC for two pulses before the calibration.
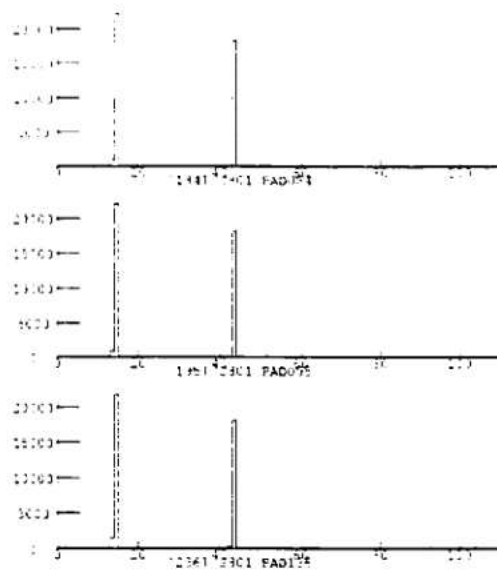
Figure 5.2: Charge distribution on three pads of CRDC for two pulses after the calibration.

65
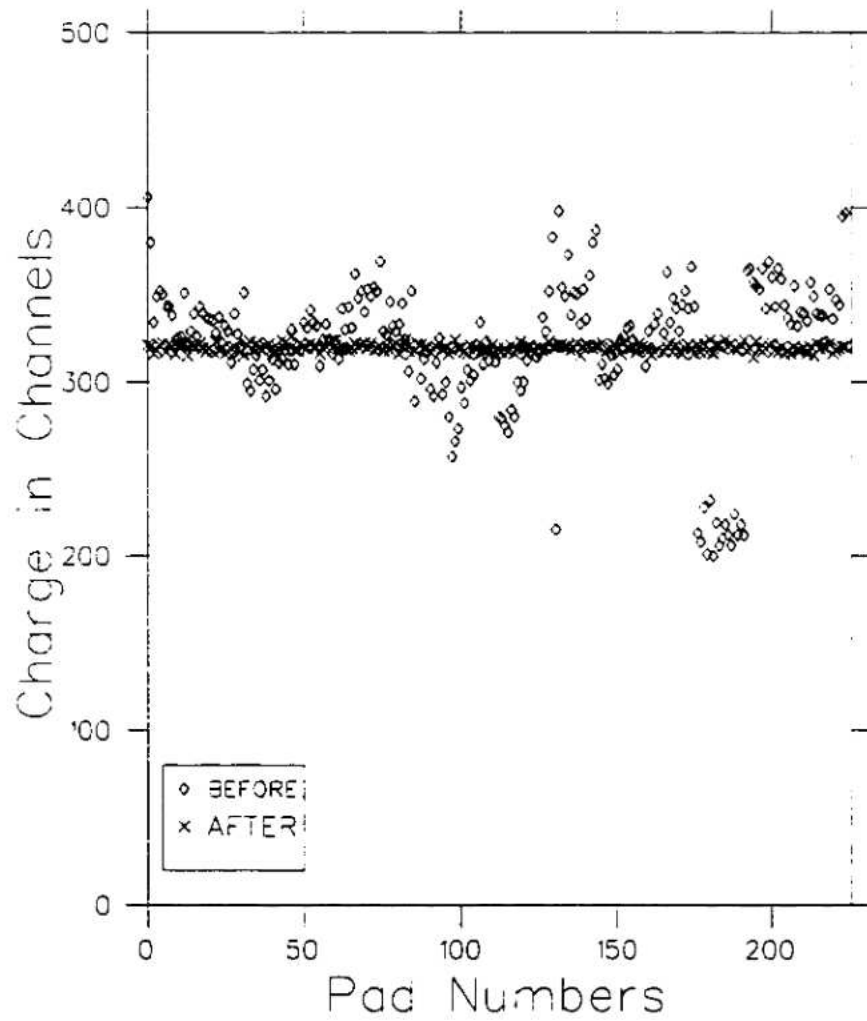
Figure 5.3: Charge distribution on the pads produced from one pulse. before and after the calibration.

66
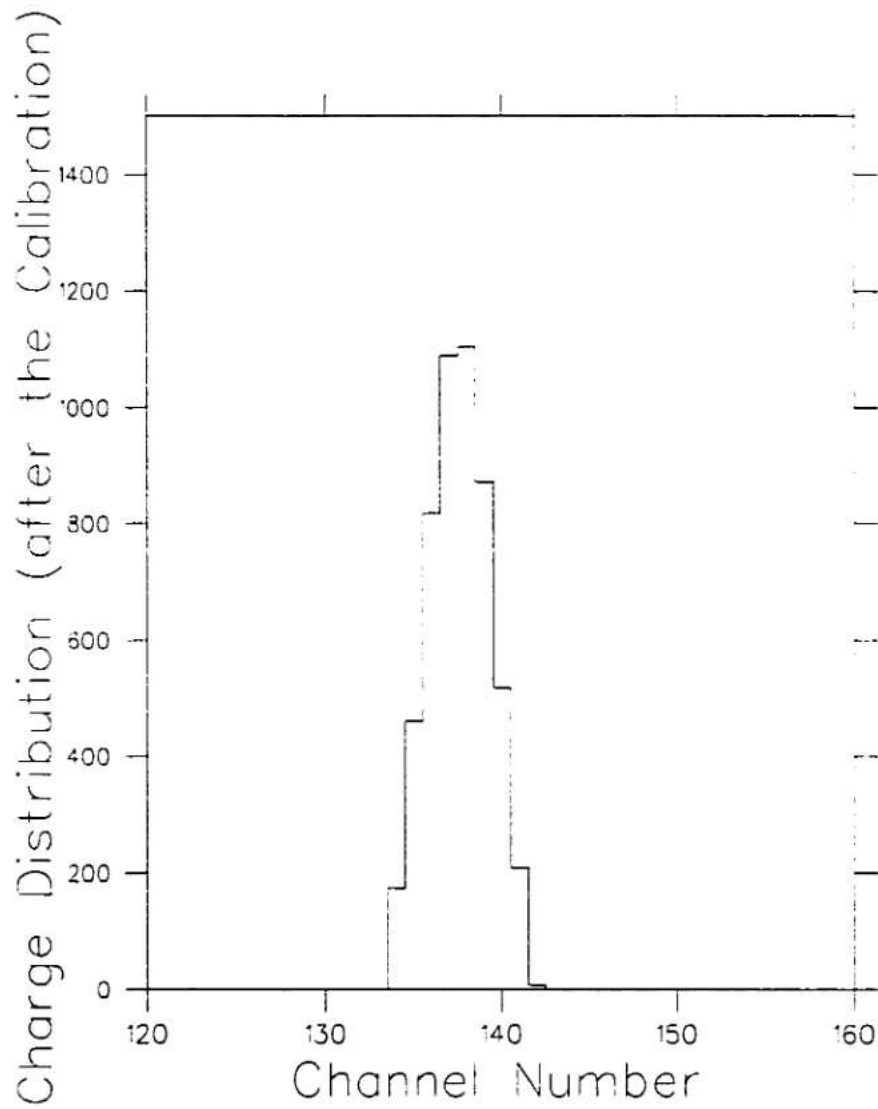
Figure 5.4: Charge distribution on the pads for a particle through a CRDC.

67

in the transverse direction is provided by the other holes at several known locations from the beam axis hole.

5.2 Particle Identification

The product $\Delta E.E$ is proportional to $Z^2 M$ [Krane(1988)], where Z is the atomic number of the particle, M is its mass, ΔE is its energy loss in the thin counter, and E is its total energy. Thus, graphing ΔE against E should yield a group of hyperbolas corresponding to different values of $Z^2 M$.

Energy loss measurement was done in the ionization chamber in order to identify ^{16}C particles from the reactions. Figure 5.5 shows the result of performing the ΔE - E analysis for particles on the focal plane. Since the Si proton detectors see only protons backscattered, as mentioned in Chapter 1, the ΔE - E plot is gated by the detected protons, and then there is only the ^{16}C group is left on the ΔE - E plot as seen in Figure 5.6.

After the first third of the experiment, the ionization chamber ceased working. The total charge collected on the cathode pads in a CRDC also depends on the nuclear species and its energy loss in the detector gas, and thus was used as a $\Delta E \times Z^2$ measurement for particle identification, even though charge resolution was barely sufficient to separate particle groups. However, the same proton gate was applied on the CRDC to define ^{16}C particles that hit it.

68

Figure 5.5: ΔE - E Particle Identification spectrum, in Channels
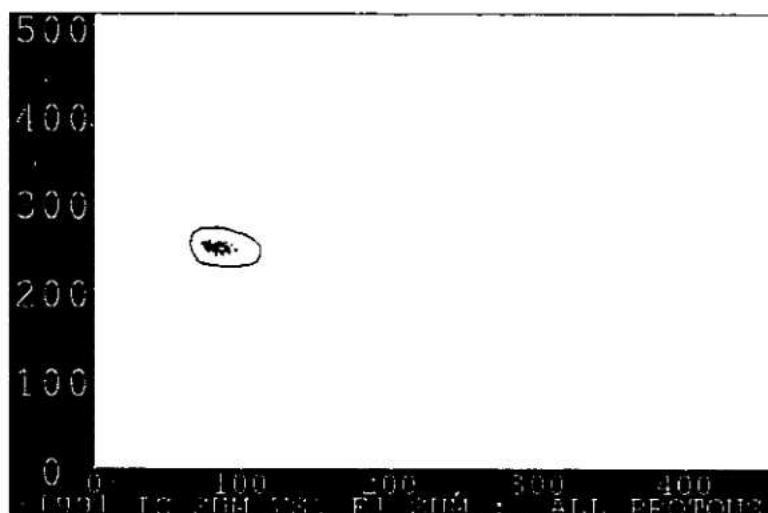
Figure 5.6: ^{16}C Group on the ΔE-E spectrum gated with protons

69

5.3 Ray Reconstruction

Nuclear reactions occur in the target chamber and the emerging particles from the reaction are detected in the focal plane. Converting the measurements on the focal plane to those on the target is crucial to getting information from the reaction, such as particle species, scattering angle, and energy. Since the S800 spectrograph makes use of the magnetic elements to direct the particles which pass through it, a particle moving through the magnetic fields can be tracked analytically, as they obey the Lorentz law $\mathbf{F} = q(\mathbf{E} + \mathbf{v} \times \mathbf{B})$, if the magnetic fields of all the magnetic elements are known.

The coordinate system is shown in Figure 4.4. The coordinate z defines the distance along the central path at any point in the motion. The coordinate x defines the dispersive direction, which is perpendicular to the z axis. The coordinate y defines the transverse direction, which is perpendicular to the coordinate z, as well. The particles are bent in the xz plane. θ is the angle in the xz dispersive plane. ϕ is the angle in the yz transverse plane. In Figure 4.4, a particle is assumed to be emitted from, or passing through, point x_1, y_1 in the plane $z_1 = 0$. After having traversed the magnetic system, it is detected at position x_2, y_2 in the plane $z_2 = 0$. The direction of the particle before entering and after exiting the magnetic system is specified by the angles θ_1, ϕ_1 and θ_2, ϕ_2. For simplicity, it is assumed that the magnetic system is mechanically symmetric about a plane assumed to be the xz plane and that the magnetic field is every where perpendicular to the symmetry plane [*Berz et al.*(1993), *Bazin*(1998)].

70

The position at the exit is a function of the position and direction at the entrance and of the momentum [*Enge*(1979)], as

$$x_2 = f(x_1, \theta_1, o_1, \delta) \tag{5.1}$$

with similar expressions for y_2, θ_2, and o_2. Here, $\delta = \Delta p/p_0$ is the deviation from the reference momentum p_0 that is the momentum of a particle that passes through the center of the magnets. p_0 is defined as $p_0 = qB\rho$ for the dipole elements, where ρ is the central bend radius for the dipoles. B is the dipole magnetic field, and q is the ionic charge of the particle. It is assumed that the exit coordinate system has been placed such that a particle with momentum p_0 emitted along the z_1 axis exits along the z_2 axis. Equation 5.1 can be expressed as a Taylor expression in x_1, θ_1, y_1, o_1, and δ, that can be written as [*Enge*(1979)]

$$\begin{aligned}
\frac{x_2}{\rho} &= (x/x)\frac{x_1}{\rho} + (x/\theta)\theta_1 + (x/\delta)\delta + \\
&+ (x/x^2)\frac{x_1^2}{\rho^2} + (x/x\theta)\frac{x_1}{\rho}\theta_1 + (x/\theta^2)\theta_1^2 + \\
&+ (x/x\delta)\frac{x_1}{\rho}\delta + (x/\theta\delta)\theta_1\delta + (x/\delta^2)\delta^2 + \\
&+ \cdots
\end{aligned} \tag{5.2}$$

where, (x/x) is the first order derivative $\partial x_2/\partial x_1$, and it is called transfer coefficient. (x/θ) is the first order derivative $\partial x_2/\partial \theta_1$, and similarly (x/x^2) and $(x/x\theta)$ are the second order derivatives $\partial^2 x_2/\partial x_1^2$ and $\partial^2 x_2/\partial x_1^2$, respectively. The factor (x/x) is the magnification of the system in the x (dispersive) direction, and (x/δ) is the dispersive which measures the displacement in the x direction at the exit per unit

71

change in δ. Since there is a symmetry about the median plane in the system. the terms $(x/y^n o^m)$ are zero if $n + m$ is odd.

A simple transfer matrix can be used to find the relation between the exit and the entrance coordinates [Berz et al.(1993)]. Each magnetic element in the S800 has its own transfer matrix that contains information as to how a particle's motion changes as it travels through the magnetic element. Total transformation of the particle through the entire S800. the sequence of the consecutive magnetic elements. is the product of the transfer matrices. If the total transformation matrix is known. it can be inverted to convert the final coordinates (on the focal plane) to the initial coordinates (on the target). This process of reconstructing the quantities on the target from the measured quantities on the focal plane is referred to as ray reconstruction [Bazin(1998)].

Four quantities are measured on the focal plane. and they are related to four quantities on the target by the matrix equation [Berz et al.(1993)]

$$\begin{pmatrix} x_f \\ \theta_f \\ y_f \\ o_f \end{pmatrix} = S \begin{pmatrix} \theta_i \\ y_i \\ o_i \\ d_i \end{pmatrix} \tag{5.3}$$

where the quantities on the target and focal plane are denoted by subscripts i and f. respectively. and d is the fractional kinetic energy difference from the central ray. that is $d = (E - E_0)/E_0$. The matrix inversion procedure is complicated and described in detail in [Berz et al.(1993)]. The resultant matrix R is not the true inverse of S.

72

but can be used to get the energy and the scattering angle on the target.

$$
\begin{pmatrix} \theta_i \\ y_i \\ o_i \\ d_i \end{pmatrix} = R \begin{pmatrix} x_f \\ \theta_f \\ y_f \\ o_f \end{pmatrix}
\tag{5.4}
$$

The inversion matrix for this study was obtained by D. Bazin (1998) [$Bazin$(1998)] using the code COSY INFINITY [$Berz$(1995)]: an inverse matrix for a run is given in Appendix A.

5.4 The S800 Detection Efficiency

Since we are looking for a cross section in this study, it is crucial to understand the solid angle of the S800 system. That the S800 is a complex design makes the conventional notation of solid angle as simply A/r^2 inappropriate.

As mentioned before, the S800 is a high resolution, wide acceptance spectrometer. However in our case, not all of the ^{16}C nuclei would be detected due to the kinematics of the reaction. Since we are interested in a two-body reaction, and detecting both proton and ^{16}C, we need to determine, for each detected proton, the detection efficiency for its companion ^{16}C. The detection efficiency for the protons in a silicon detector is essentially 100 percent.

The S800 efficiency at detecting particles is primarily a function of laboratory scattering angle, since the particles would start to hit the entrance apertures of the S800 system for the large scattering angles. The case is complicated further since particles that successfully enter the S800 are magnetically analysed by the dipole

73

magnets. whose magnetic fields involved are strong and significantly non uniform. This makes the detection efficiency a function of particle energy. as well.

The design of the detector system is such that reaction product protons detected in the very backward angle CD detectors have corresponding ^{16}C ions that have kinematically very small laboratory scattering angles. Consequently. the S800 detection efficiency for these reactions is expected to be almost 100 percent. However. for protons detected in the strip detectors. the corresponding ^{16}C ions have quite large scattering angles. so the detection efficiencies for these reactions are therefore substantially lower.

We utilized a program written at the MSU. which used a Monte Carlo simulation of the entire kinematic process in order to deduce the S800 detection efficiency. The Monte Carlo technique simulates every stage of a single particle's projection through the apparatus. At each stage of that trajectory. typical kinematic parameters are chosen. and the resulting particle energy and momentum is calculated. This process is then repeated many times. with each particle having a different set of initial kinematic parameters being chosen. Each time a kinematic parameter is required. it is chosen from a random distribution which is weighted to. on average. reproduce the actual distribution.

The code was run. simulating 10^6 events. for each angle from 0 to 5.30 degrees with a 0.05 degree increment. An event is recorded if the proton is ejected within a given angular range and the ^{16}C successfully make it to the the focal plane. The

74
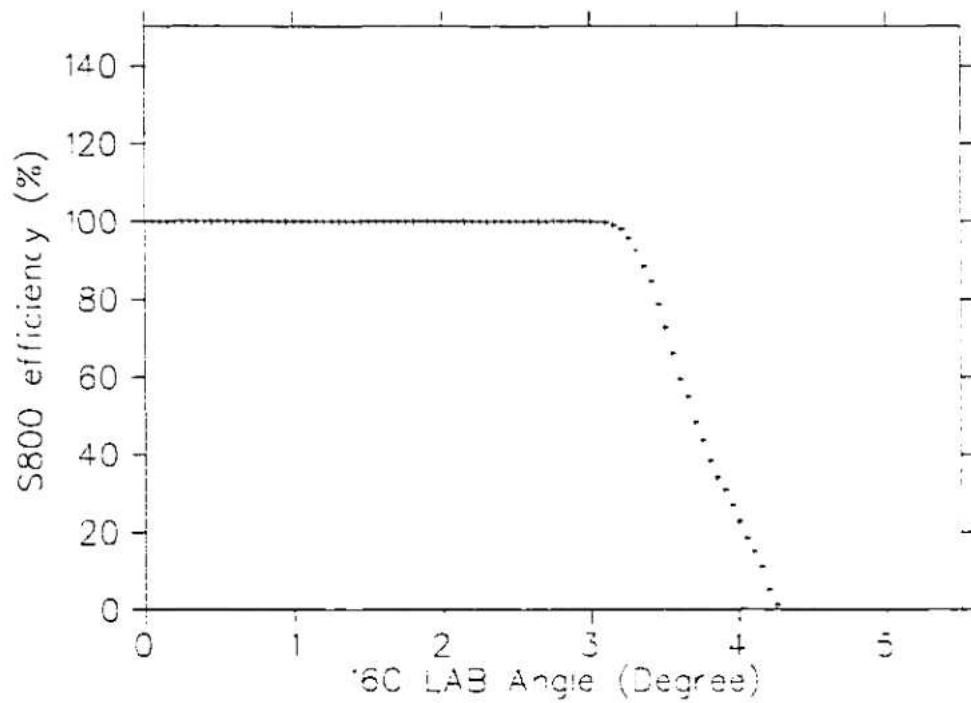
Figure 5.7: S800 Detection Efficiency versus ^{16}C Laboratory Angle.

S800 detection efficiency was obtained by dividing the number of hits by the number of events. and is plotted as a function of the angle of ^{16}C in Figure 5.7.

75

CHAPTER 6

Results and Discussion

After the experiment it was found that the detectors that provided beam particle tracking did not function during the experiment. This affected both the energy and the position resolutions, which, therefore, were not good. Without the beam tracking information, our best assumption is that there was zero angular divergence of the beam, i.e. it was incident at right-angles with the target, and that there was a zero beam size. However, it is also possible to correct for these assumptions in beam spot size and angular divergence; our corrections are discussed in the next section of this chapter.

6.1 Angular Distribution of the Differential Cross Section

Roughly speaking, the cross section is a measure of the relative probability for the nuclear reaction to occur. If a detector is placed to record particle b emitted in a direction (θ, ϕ) with respect to the beam direction, then the detector defines a small solid angle $\Delta\Omega$ at the target nucleus, as seen in Figure 6.1. If the current of incident particles is I_a per unit time, and the target shows to the beam n target nuclei per

76
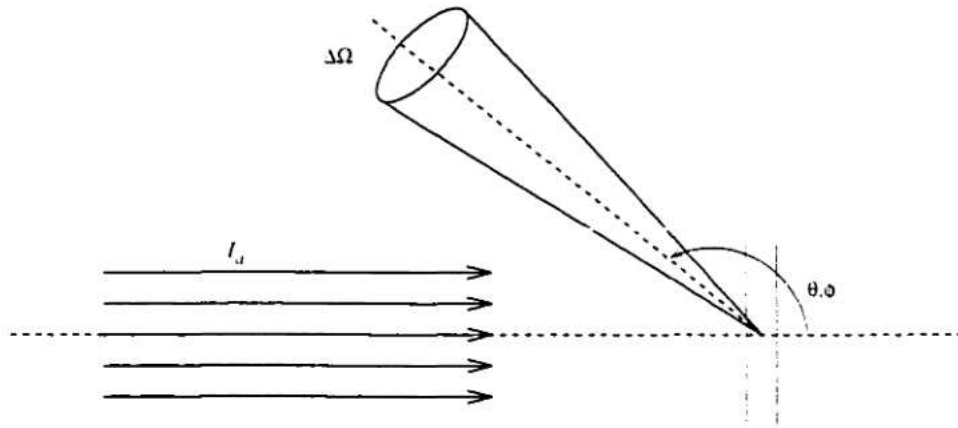
Figure 6.1: Reaction geometry showing incident beam, target, and outgoing beam going into solid angle $\Delta\Omega$ at θ, ϕ.

unit area, and the outgoing particles appears at rate of R_b, the reaction cross section is given as

$$\sigma = \frac{R_b}{I_a n} \tag{6.1}$$

or

$$\sigma = \frac{number\ of\ reactions\ per\ target\ nucleus}{number\ of\ incident\ particles\ per\ unit\ area}. \tag{6.2}$$

Thus the cross section has dimensions of area.

Equation 6.1 can be rewritten for a section of a detector used in this experiment as

$$\Delta\sigma = \frac{\sum_i \frac{Y_i}{\prod_j \varepsilon_{ij}}}{n \sum_i I_i t_i} \tag{6.3}$$

where Y is the yield that is the number of outgoing reaction products detected. ε is the efficiency. n is the number of deuterons in the CD_2 target per unit area. I is the

77

$w_{CD_2}(\text{mg/cm}^2)$	$M_{CD_2}(\text{g/mole})$	$n\ (\#\,ofD/cm^2)$
1.94	16.0282	1.44×10^{20}

Table 6.1: Macroscopic Quantities of the CD_2 Target

current of the ^{15}C projectiles. t is the time duration of the run, and the sum $\sum_i$ is over the runs, and the product $\prod_j$ is over the different efficiencies, such as dead time of the data acquisition system and geometric efficiencies.

The number of deuterons in the target per cm^2, n. was calculated as

$$ n = 2\frac{w_{CD_2}}{M_{CD_2}}N_A . \tag{6.1} $$

where w_{CD_2} is the target thickness in gr/cm^2. M_{CD_2} is the molar mass of the CD_2 in grams/mole. N_A is the Avogadro's number in number/mole, and the factor 2 is because there are two deuterium atoms in each CD_2 molecule. The values of all these quantities and the result of n are given in Table 6.1.

The cross section $\Delta\sigma$ in the laboratory system was calculated for each section of each detector, that is for each ring of each CD detector and for each strip of the others. Then the differential cross section $d\sigma/d\Omega$ was calculated by dividing $\Delta\sigma$ by the appropriate solid angle $\Delta\Omega$ of the part of the detector being considered. the results are represented in Table 6.2. The differential cross section versus the scattering angle in the laboratory system is shown in Figure 6.4. The laboratory angles corresponding to the sections of the detectors were determined as follows.

78

θ_{LAB}	$\Delta\Omega_{LAB}$(msr)	$\frac{d\sigma}{d\Omega}_{LAB}$(mb/sr)	θ_{CM}	$\frac{d\sigma}{d\Omega}_{CM}$(mb/sr)
171.30	8.62	0.29	2.74	2.90
170.78	9.10	0.27	2.90	2.69
170.26	9.58	0.16	3.07	1.61
169.75	10.05	0.28	3.23	2.80
169.23	10.51	0.30	3.40	2.94
168.72	10.97	0.31	3.56	3.04
168.21	11.41	0.23	3.72	2.27
167.70	11.85	0.20	3.89	1.93
167.19	12.28	0.22	4.05	2.18
166.69	12.71	0.22	4.21	2.11
166.19	13.12	0.16	4.37	1.56
165.69	13.53	0.14	4.54	1.39
165.19	13.93	0.10	4.70	0.93
164.69	14.31	0.10	4.86	1.00
164.20	14.69	0.04	5.02	0.37
163.71	15.06	0.00	5.18	0.00
163.93	28.05	0.34	5.11	3.19
163.01	29.33	0.32	5.41	2.97
162.10	30.54	0.29	5.71	2.68
161.19	31.69	0.28	6.02	2.59
160.30	32.78	0.24	6.31	2.22
159.42	33.80	0.27	6.61	2.41
158.55	34.76	0.23	6.90	2.10
157.69	35.65	0.26	7.20	2.27
156.84	36.48	0.25	7.49	2.21
156.00	37.25	0.23	7.78	2.02
155.17	37.95	0.21	8.06	1.85
154.35	38.60	0.21	8.35	1.77
153.54	39.18	0.21	8.64	1.77
152.74	39.71	0.21	8.92	1.76
151.96	40.18	0.23	9.20	1.91
151.19	40.60	0.23	9.48	1.86

Table 6.2: Results for the Differential Cross section in the Laboratory and Center of Mass systems.

79
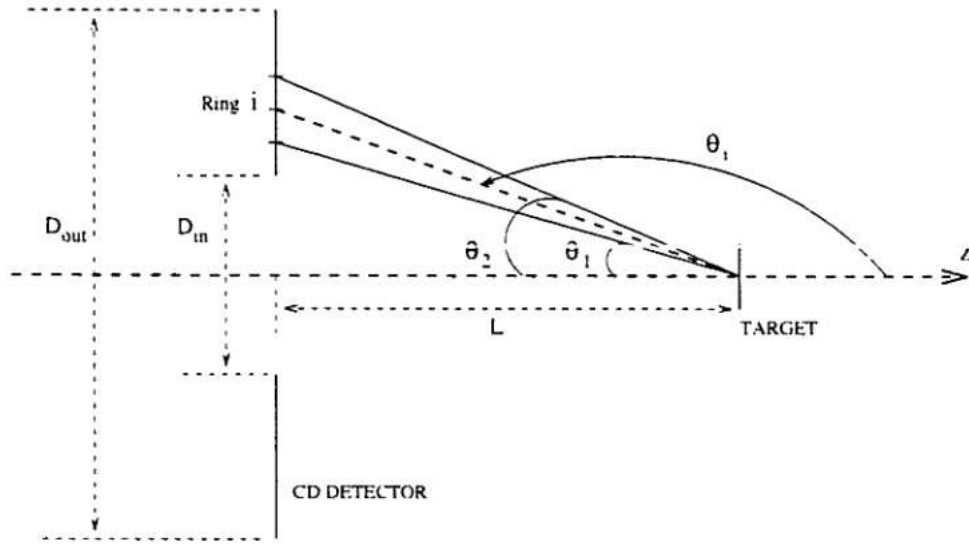
Figure 6.2: Geometry of a CD Detector with the Target

For CD detectors, the laboratory angle corresponding to each ring is the one between the positive z axis and the midpoint of the ring, as seen in Figure 6.2. The laboratory angle θ for a ring can be obtained from

$$tan(180 - \theta_i) = \frac{\frac{D_{in}}{2} + (2i - 1)\frac{1}{2}\frac{(D_{out}-D_{in})/2}{N_{ring}}}{L} .$$ (6.5)

where, i is the identification (ID) number of the ring, which changes from 1 to 16. D_{in} and D_{out} are the inner and outer diameters of the CD detector, respectively. N_{ring} is the number of the rings of a CD detector, and L is the separation between the target and the CD detector.

80
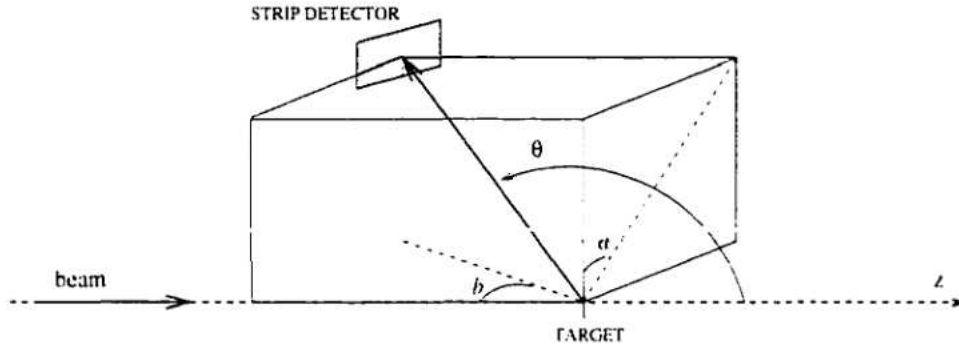
Figure 6.3: Geometry of a Strip Detector with the Target

For the strip detectors, the laboratory angle corresponding to each strip is again the one between the midpoint of the strip and the positive z axis, and it was determined based on the known angles shown in the Figure 4.10 and 4.11 as follows

$$tan(180 - \theta) = tan(b) \left(\frac{1}{tan^2(a)} + 1 \right)^{1/2} . \qquad (6.6)$$

where a and b are the angles shown in Figure 6.3.

As seen in Figure 6.4, there is a discontinuity between the two CD detectors. This is to be expected from a finite beam spot size and finite angular divergence of the incident beam, which were not accommodated in the calculation of the cross section. The outermost few rings of the back CD detector (which is the more backward angle detector) will see fewer events corresponding to protons backscattered from the $d(^{15}C,p)^{16}C$ reaction than it should, as the innermost rings of the CD detector closer to the target should will partially block them. This effect is due to the finite beam spot size. Similarly, some blockage will also result from the beam divergence, the effect of the incident beam impacting the target from directions other than

81

directly perpendicular to it. Correction can be made for those effects, as will be discussed below. Finally, though there might be another effect, i.e., an offset of the beam from the cylindrical (z) axis of symmetry for the CD detectors.

In order to check whether plausible choices of these parameters could produce the observed effects, we have performed a simple Monte Carlo simulation of the proton yield with the inclusion of a beam spot size, an angular divergence of the incident beam, and an offset of the beam from the z-axis. We would expect a beam spot size about 0.7 cm FWHM based on the measurement from a scintillator target, and the incident beam perpendicular to the target with a distribution about 4 degrees FWHM, that corresponds to maximum incident angles up to ± 3 degrees based on the estimate from the geometry of the collimation slit and the target.

Assuming the distribution is Gaussian for both finite spot size and angular divergence, an event is simulated by taking a particle with mass that is equal to a ^{15}C nucleus, with energy of the beam, and direction perpendicular to the target, modified by an amount randomly chosen from a Gaussian distribution. Then, including the Q value and excitation energy, the reaction kinematics are calculated for the $d(^{15}C,p)^{16}C$ reaction in order to obtained the direction and energy of the outgoing proton. For a zero beam spot size, protons would be scattered from the centre of the target, i.e., along the z-axis through the centre of the CD detectors. A random offset in the x and y directions is chosen from a Gaussian distribution in order to include the effect of finite beam spot size.

82
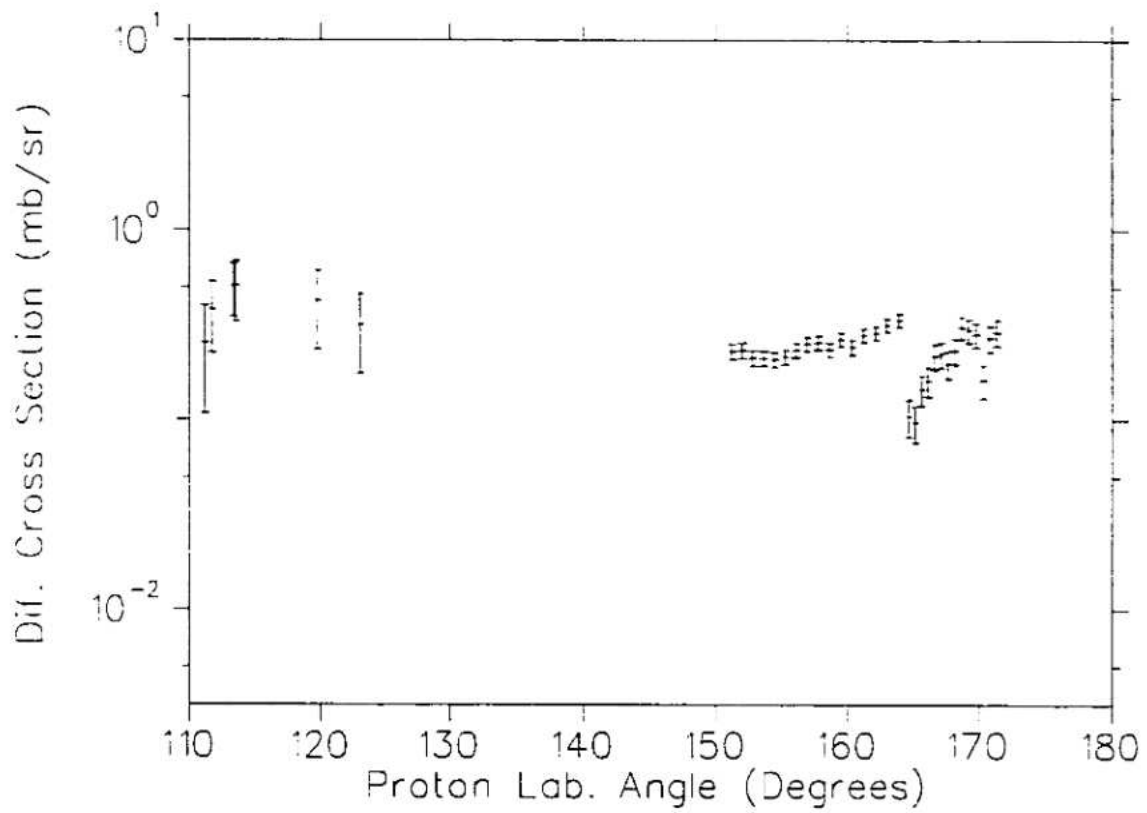
Figure 6.4: Differential Cross Section versus Scattering Angle in the Laboratory System

83

The resulting proton trajectory is calculated. and if it should be in a direction which passes through one of the CD detectors. it is recorded as a hit in the appropriate ring. Typically 10^8 events were simulated in this way for each Monte Carlo run. and the resulting angular distribution of the hits compared to the data.

The mean width of the beam spot size and incident ^{15}C angle distributions was set for each Monte Carlo run. the aim being to run the Monte Carlo several times. each with different choices of widths. The results from several of the runs are shown in Figure 6.5. which shows the ratio of the number of protons detected in the run with a finite beam spot size and incident angular divergence to the run with zero beam spot size and no angular divergence versus the CD detector ring ID number. corresponding to the angle in the Figure 6.4. The run with the choice of 0.7 cm for the beam spot size. and ±3 degrees for the incident angular width. exhibits a discontinuity very similar to that of the actual data. as can be seen in Figure 6.5. Therefore. we redraw Figure 6.4 by dividing the differential cross sections by the results of the Monte Carlo calculations in order to compensate for the shadowing of the back CD detector by the forward one. Figure 6.6 shows the correction of the finite beam spot and the angular divergence only. The resulting differential cross section distribution which includes also the effect of the 0.7 cm offset of the incident beam from the z-axis is shown in Figure 6.7. However. comparing Figure 6.6 and Figure 6.7. the offset is seen to have little effect and possibly even increased the discontinuity. Thus it was set to zero.

84
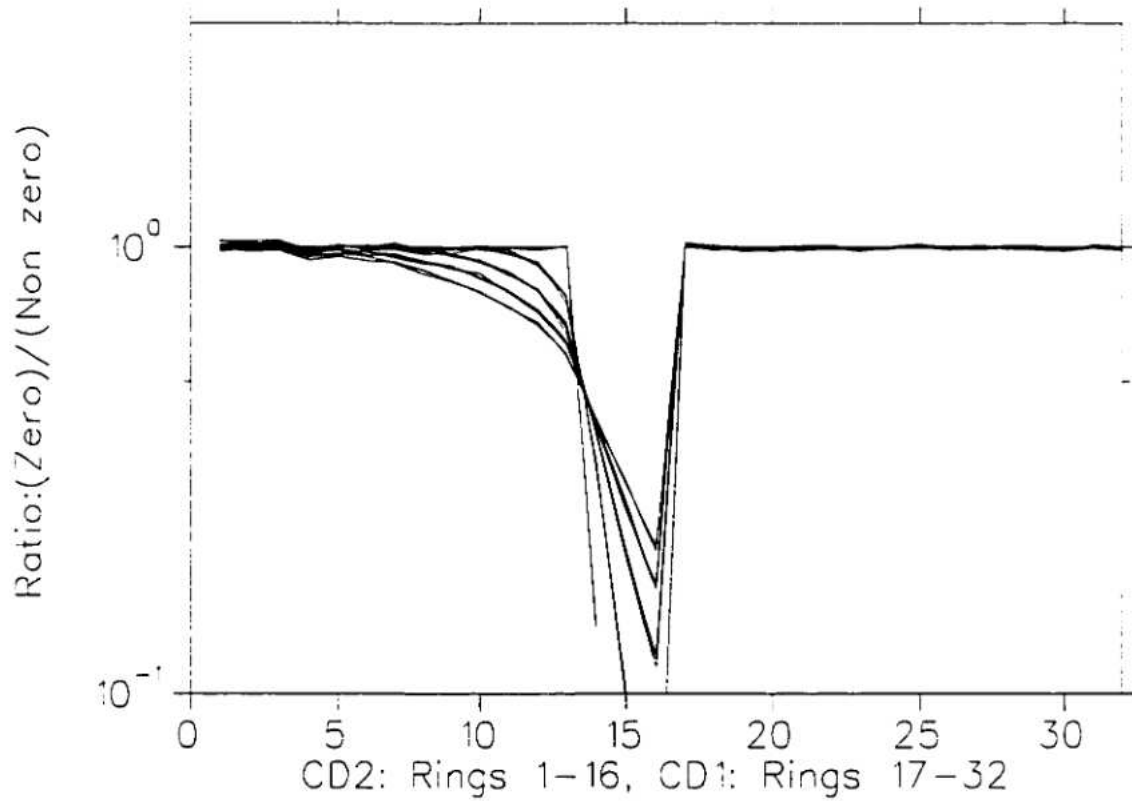
Figure 6.5: The Ratio of The Number of Protons Detected in the Monte Carlo Simulation with a Finite Beam Spot Size and Incident Angular Divergence to the Simulation with Zero Beam Spot Size and No Angular Divergence versus the Laboratory Angle of the CD Ring

85
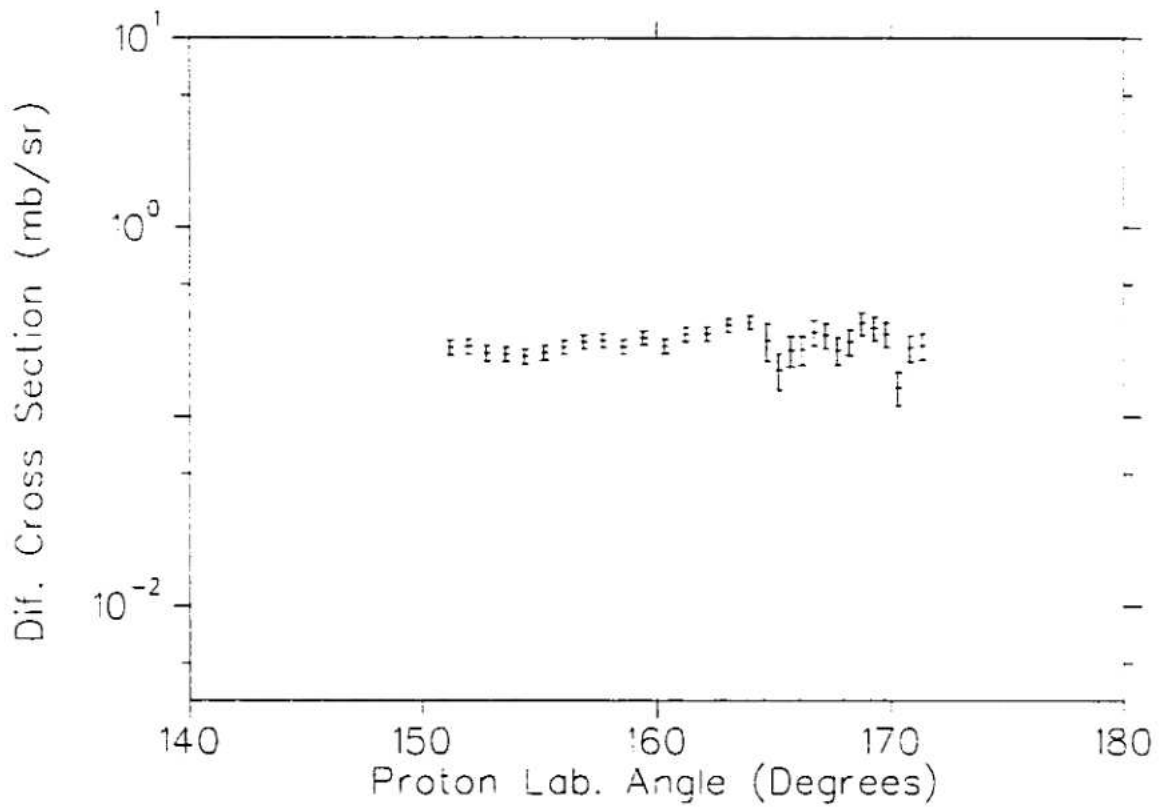
Figure 6.6: Corrected Differential Cross Section versus Scattering Angle in the Laboratory System, with the Monte Carlo Simulation for only Finite Beam Spot Size and Angular Divergence

86
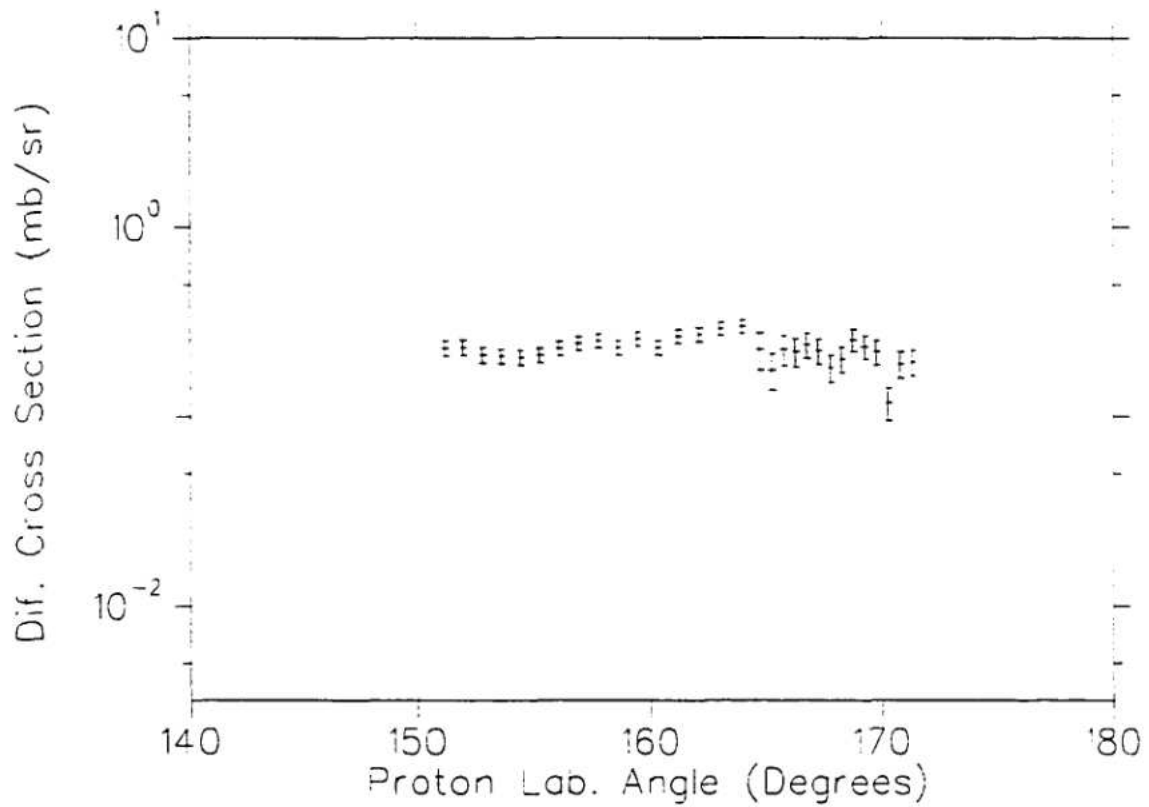
Figure 6.7: Corrected Differential Cross Section versus Scattering Angle in the Laboratory System. with the Monte Carlo Simulation for Finite Beam Spot Size. Angular Divergence. and Offset

87

6.2 DWBA Calculation

The DWBA formalism is a well known attempt to describe direct nuclear reactions. as discussed in Chapter 3. The differential cross section is compared to the theoretical DWBA calculation provided by the software DWUCK4 [Kunz (1979)], which is a standard computer code often used in such analysis. This reaction description requires potentials in the entrance and exit channels to characterize the interaction between the two nuclei. so as to produce the distorted waves for the Born approximation calculation. As discussed in Chapter 2 and 3. in terms of the transition matrix. T_{if} the cross section is given by

$$\left(\frac{d\sigma}{d\Omega}\right)_{if} = \frac{m_f m_i k_f}{(2\pi \hbar^2)^2 k_i} |T_{if}|^2 \tag{6.7}$$

In the DWBA formalism. the transition matrix is approximated by

$$T_{if}^{DWBA} = \langle \chi_f^- o_f | V | o_i \chi_i^+ \rangle \tag{6.8}$$

χ_i and χ_f are the elastic scattering (optical model) wave functions for the entrance and exit channels. respectively. o_i (o_f) is the internal wave function of the target (residual) nucleus in the entrance (exit) channel. and V is the perturbative interaction potential. The optical model wave functions used by DWUCK4 to characterize the interaction between the deuteron and ^{15}C nuclei. and between the proton and ^{16}C nuclei were based on a set of optical parameters obtained from the parameter systematics of [Perey and Perey (1976)]. These parameters are given in Table 6.3.

88

Channel	V (MeV)	r_o(fm)	a_o(fm)	W_D(MeV)	r_D (fm)
^{15}C+d	77.01	1.15	0.81	24.06	1.34
^{16}C+p	59.89	1.25	0.65	13.50	1.25
^{15}C+n	48.20	1.25	0.66		
Channel	a_D(fm)	r_c(fm)	V_{so}(MeV)	r_{so}(fm)	a_{so} (fm)
^{15}C+d	0.68	1.15	7.0	0.75	0.50
^{16}C+p	0.47	1.25	7.5	1.25	0.47
^{15}C+n			6.2	1.01	0.75

Table 6.3: Optical parameters used in the DWBA calculation of the ^{15}C(d,p) ^{16}C

The optical model potential is defined [Perey and Perey (1976), Kunz (1979)] as follows

$$U(r) = V_c - V f(x_0) + \left(\frac{h}{m_\pi c}\right)^2 V_{so}(\sigma.l)\frac{1}{r}\frac{d}{dr}f(x_{so}) - i[W f(x_W) - 4W_D\frac{d}{dx_D}f(x_D)] .$$

(6.9)

where, V_c is the coulomb potential of a spherical uniform charge distribution of radius $R_c = r_c.A^{1/3}$, as follows

$$\begin{aligned} V_c &= ZZ'\frac{\epsilon^2}{r} & , r \geq R_c \\ &= \left(\frac{ZZ'\epsilon^2}{2R_c}\right)\left(3 - \frac{r^2}{R_c^2}\right) & , r \leq R_c . \end{aligned}$$

(6.10)

where A is the mass number of the target nucleus. V and W are the volume attractive real and absorptive imaginary potentials, respectively. W_D is the absorptive surface imaginary potential. V_{so} is the volume spin orbit potential.

89

The functions $f(x_0)$, $f(x_W)$, $f(x_D)$ and $f(x_{so})$ are Woods-Saxon form factors with appropriate radii, r_i, and diffusivity parameters, a_i, as follows

$$f(x_i) = (1 + e^{x_i})^{-1}$$
$$x_i = \frac{r - r_i A^{1/3}}{a_i} \qquad (6.11)$$

The imaginary absorptive potential can be either volume ($W \neq 0$, $W_D = 0$), surface ($W = 0$, $W_D \neq 0$), or volume plus surface ($W \neq 0$, $W_D \neq 0$).

The possible J and L-transfer in the $^{15}C(d,p)^{16}C$ reaction are based on , as discussed in chapter 2, the following vector selection rules on L and J

$$\mathbf{J}_{16C} = \mathbf{J}_{15C} + \mathbf{J} = \mathbf{J}_{15C} + \mathbf{L} + \frac{1}{2} \qquad (6.12)$$

and the connection between the parities of the initial and final states

$$\pi_{16C} = \pi_{15C} (-)^L \qquad (6.13)$$

The known energy levels of ^{16}C are shown in Figure 6.8 [*Tilley et al.*(1993)]. The spin statistics based on the rules above for the $^{15}C(d,p)^{16}C$ reaction gives the possible L and J-transfer values as follows:

For the ground state of ^{16}C:

$$I_d^\pi = 1^+ \qquad I_{15C}^\pi = \frac{1}{2}^+$$
$$I_p^\pi = \frac{1}{2}^+ \qquad I_{16C}^\pi = 0^+$$

Thus,

$$L = 0 \quad and \quad J = \frac{1}{2}$$

90

For the first excited state of ^{16}C:

$$I_d^\pi = 1^+ \quad I_{^{15}C}^\pi = \frac{1}{2}^+$$
$$I_p^\pi = \frac{1}{2}^+ \quad I_{^{16}C}^\pi = 2^+$$

Thus.

$$L = 2 \quad and \quad J = \frac{3}{2}, \frac{5}{2}$$

Based on the all these parameters. the results of the DWBA calculations are represented in Figure 6.10. The choice of parameters to be used is somewhat uncertain. Therefore. in order to ensure that our calculations were reasonably robust to the specific choice of parameters. we repeated the DWBA calculations for likely alternative choices. We observed that the resulting angular distributions were not particularly sensitive to the specific of input parameters.

6.3 Comparison: DWBA Results and Data

In Figure 6.9. the angular distribution of the differential cross section in the laboratory system is compared to that from the DWBA calculation results. The data for the smaller laboratory angles is coming from the strip detectors. Since. in general. DWBA calculations are most believable in the forward angle part of the differential cross section (in the center of the mass) [Boyd (2000)]. we concentrated on the data from the CD detectors. which correspond to the larger laboratory angles and smaller center of mass angles. It seems that the dominant states through which the reaction

91

Energy (MeV)   Spin & Parity
      6.11   (2+,3-,4+)
——————————————   ——————————————

4.251   4+
————————————   ——————————————
15   — 3.99 —————————————— 3+ ——
  C + n
                                                   2
                                                   —

                             3.03   0+
                      ——————————————   ——————————————

                             1.77   2+
                      ——————————————   ——————————————

                                                   0+
                      ——————————————————————————————————————

                              ^{16}C
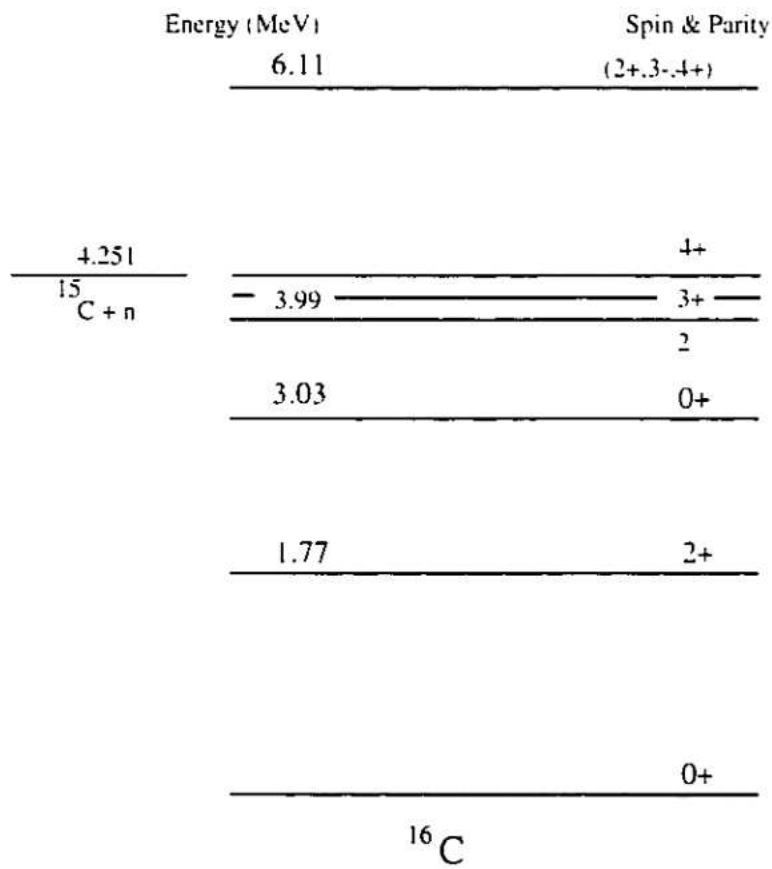
Figure 6.8: Energy Levels of ^{16}C [*Tilley et al.*(1993)]
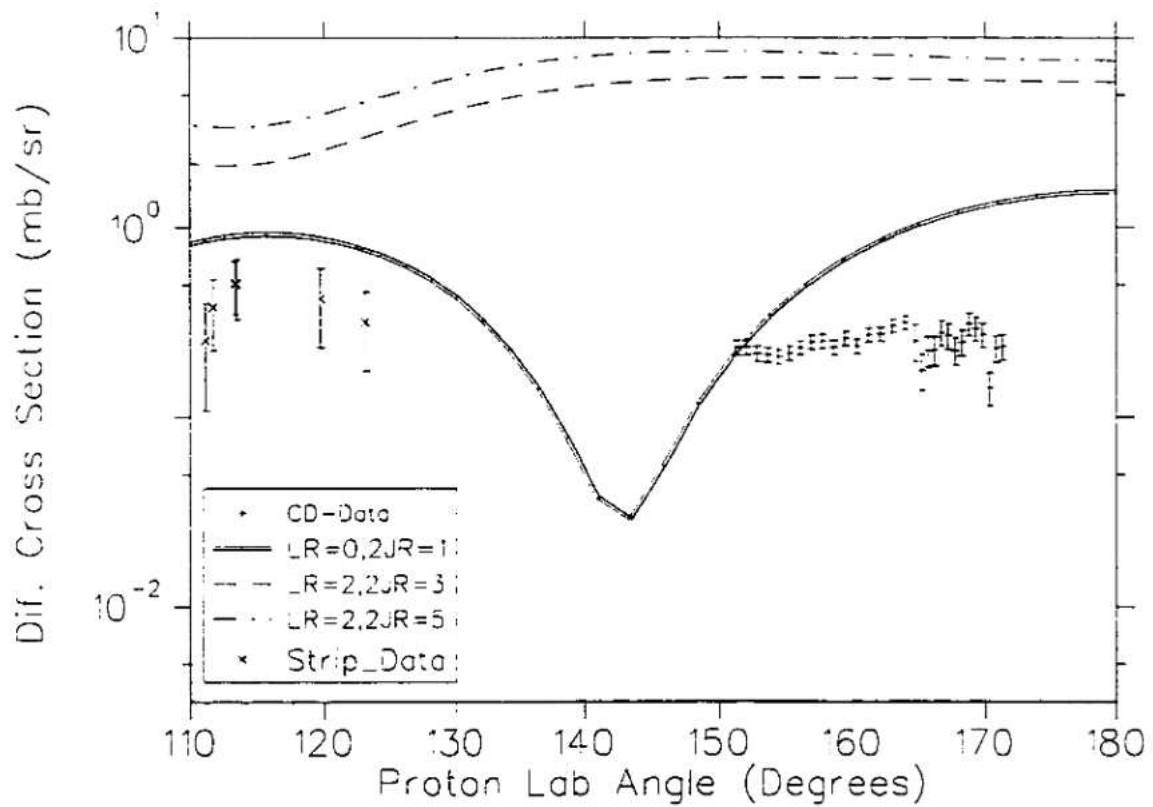
Figure 6.9: Angular Distribution of the Differential Cross Section from the Data and the DWBA Calculation. in the Laboratory System.

93

is proceeding are the excited states of ^{16}C populated by $L = 2$ angular momentum transfer. This is because the observed angular distribution is almost flat. consistent with an agreement of the DWBA calculations for the $L = 2$ transfer. but inconsistent with the angular distribution predicted for states populated by $L = 0$ transfer.

The angular distribution of the differential cross section in the laboratory system was converted to the centre of mass system (CM) using the kinematics based on the first excited state. and the result is given in Figure 6.10. The DWBA calculation gives absolute cross section. $\left(\frac{d\sigma}{d\Omega}\right)_{DWBA}$, under the assumption that the nuclear structure change in the reaction follows a model. In our case. (d.p) reaction. the model is that the transferred neutron enters a single particle state. If this is not the case. the experimental cross section. $\left(\frac{d\sigma}{d\Omega}\right)_{exp}$, will be lower than the calculated one. Then. the cross section can be written as follows

$$\left(\frac{d\sigma}{d\Omega}\right)_{exp} = S \left(\frac{d\sigma}{d\Omega}\right)_{DWBA} \tag{6.11}$$

where. S is the *spectroscopic factor*. describing the degree to which the wave function of the ^{16}C state to which the reaction proceeds looks like a shell model neutron coupled to the ^{15}C ground state.

94
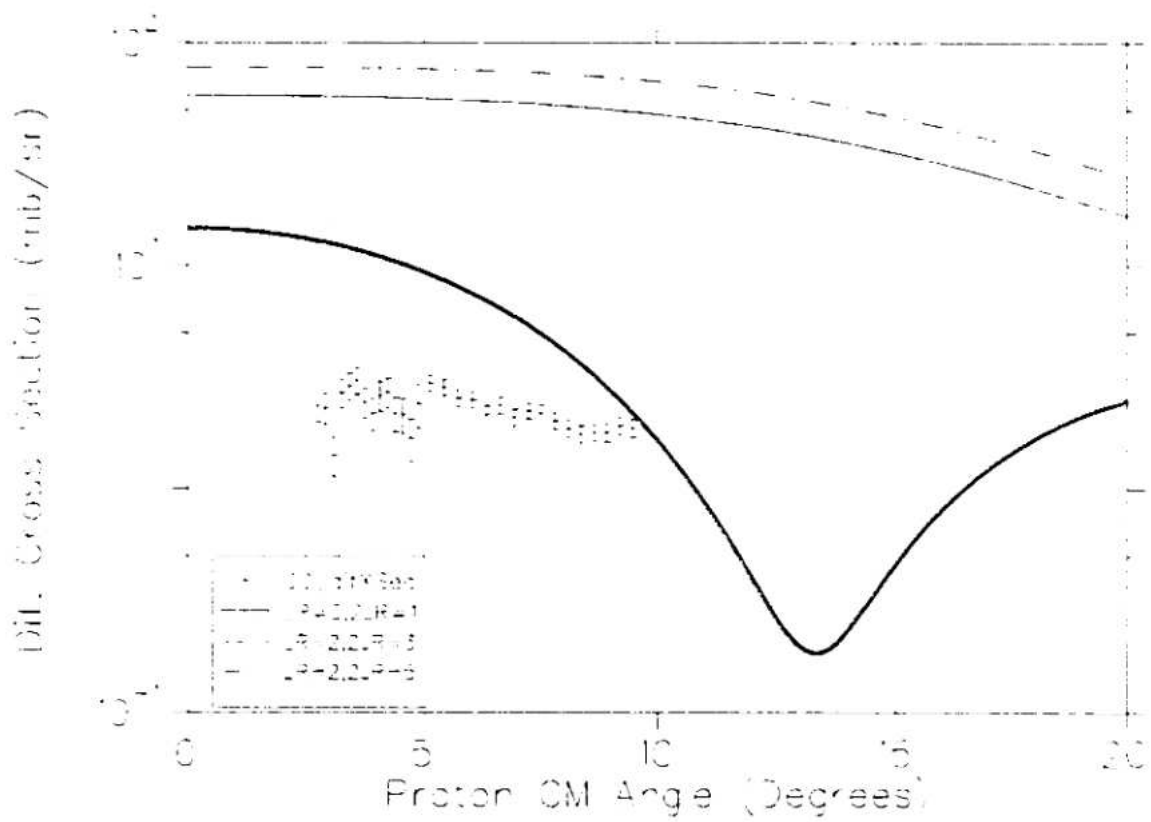
Figure 6.10: Angular Distribution of the Differential Cross Section from the Data and the DWBA Calculation. in the Centre of Mass System.

95

CHAPTER 7

Conclusion

The aim of the experiment was to measure states in ^{16}C below and just above the neutron threshold, with the hope of determining the nonresonant and resonant cross section components of the ^{15}C$(n,\gamma)^{16}$C reaction. The states below threshold could participate in direct (n,γ) capture; the ^{15}C$(d,p)^{16}$C reaction would provide the strengths of that process. Those above threshold, if they existed, would allow the ^{15}C$(n,\gamma)^{16}$C capture reaction to proceed resonantly. This reaction governs one of the branch points in the mass flow from light to heavy elements in Inhomogeneous Big Bang scenarios, and its reaction rate is an important ingredient for network calculations needed to predict cosmic abundances. Comparison of the predicted abundances with measured abundances has the potential to either confirm or rule out models of the Inhomogeneous Big Bang.

Several states are known in ^{16}C, three of them closely spaced (3.99 MeV, 4.09 MeV, and 4.14 MeV) and just below the neutron threshold (4.25 MeV). The first known state in ^{16}C above threshold is at 6.11 MeV, far beyond the astrophysically relevant excitation energies.

96

As mentioned in Chapter 2. the energy of the outgoing proton gives the energy of the excited state of the residual nucleus. The angular distribution and the polarization of the proton give the spin and the parity of the state. and the absolute magnitude of the cross section allows measurement of the spectroscopic factor, or single particle occupation probability of the state in which the neutron is captured. Therefore. good energy resolution and good determination of particle trajectories are crucial.

Due to the beam spot size on the target and close detector geometry. protons detected at the same coordinates can correspond to quite different scattering angles. It is therefore necessary to: (a) track each ^{15}C particle. and thus determine its point of impact on the target: (b) determine the coordinates of each proton hitting a detector: (c) calculate the scattering angle of the proton as a function of the incoming vector of the ^{15}C hitting the target and outgoing vector of the proton leaving the target and hitting the detector: (d) plot the ΔE - E for several scattering angles and isolate the proton groups of interest.

Since the S800 is a high resolution spectrometer. the ΔE - E plot was obtained for the ^{16}C particles. detected by the S800. corresponding the protons detected by the Si detectors. However. this experiment is the first one with the S800 spectrometer. and after the experiment. it was found that some devices did not function during the experiment. especially the detectors that provided beam particle tracking. This effected both the energy and the position resolutions.

97

Nevertheless. we were able to measure a good angular distribution of the differential cross section. although it may be for several unresolved states. As discussed in Chapter 6. it seems that the dominant states through which the reaction is proceeding are the excited states of ^{16}C populated by $L = 2$ angular momentum transfer. There may also be a contribution from the $L = 0$ transfer. but the resolution is not good enough to separate the states. In order to check our sensitivity to this contribution. we compared the DWBA calculations for the $L = 0$ transfer and the $L = 2$ transfer as follows. For each angle at which data exist. some percentage of the differential cross section for the $L = 0$ transfer was added to that for the $L = 2$ transfer. and then the resultant distribution scaled to the experimental results. The range of the $L = 0$ percentage lies from 1 to 90. The results for 1 and 90 percent contribution of the $L = 0$ transfer are represented in Figure 7.1 and Figure 7.2. respectively. There is little difference between the two results. This leads to the conclusion that any contribution from a state populated by a $L = 0$ transfer would have an unobservable effect on the observed yield. This is due to two factors. one being the poor experimental resolution. and the other being the intrinsic dominance of the reaction yield by $L = 2$ transfer. as shown by the DWBA results. Thus. the contribution of any state populated by a $L = 0$ transfer cannot be determined from our results. Excited states potentially populated by $L = 0$ transfer. through which resonant scattering could occur. would be expected to dominate the astrophysical reaction rate for $^{15}C(n.\gamma)^{16}C$ reaction.

98
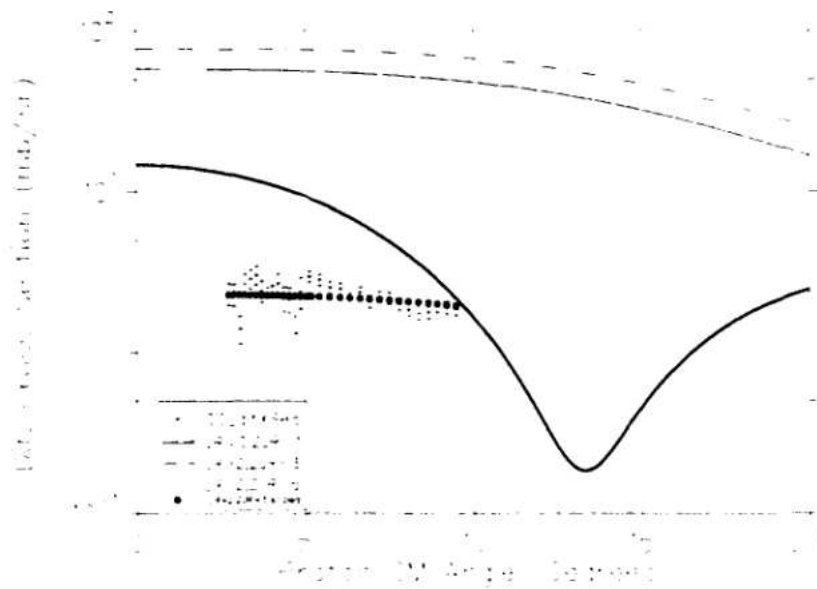
Figure 7.1: Result for 1% contribution of the $L = 0$ transfer to the $L = 2$ transfer.
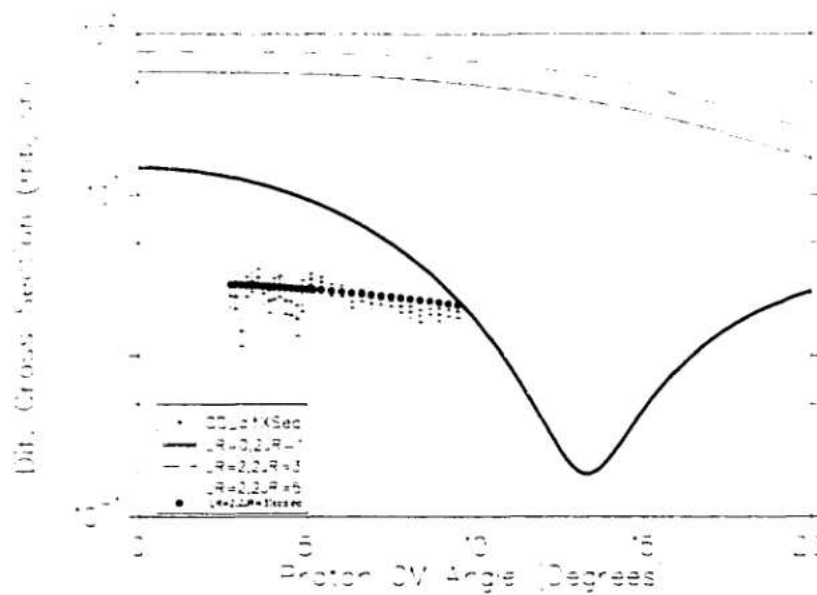
Figure 7.2: Result for 90% contribution of the $L = 0$ transfer to the $L = 2$ transfer.

99

Appendix A

An Inverse Transfer Map

This appendix lists all of the inverse map coefficients used to reconstruct energy and scattering angle. The reconstructed coefficients are θ_t, y_t, ϕ_t and δ on the target are as a function of x_f, θ_f, y_f, and ϕ_f in the focal plane. The δ is the reconstructed fractional energy. $\delta = (E - E_0)/E_0$.

100

COEFF.#	COEFFICIENT	ORDER	x_f	θ_f	y_f	ϕ_f
1	0.1736180354925927E-01	1	1	0	0	0
2	-.9525841918468597	1	0	1	0	0
3	-.1260605599153401E-01	2	2	0	0	0
4	0.1980454843431094-1	2	1	1	0	0
5	0.8121509034926742E-01	2	0	2	0	0
6	0.1527812184232483E-01	2	0	0	2	0
7	-.1199131357886932	2	0	0	1	1
8	0.9867106054237444E-01	2	0	0	0	2
9	0.3533976594684741E-02	3	3	0	0	0
10	-.5437142097162120E-01	3	2	1	0	0
11	0.2622676144252794	3	1	2	0	0
12	-5.770549384936888	3	0	3	0	0
13	0.8705659984424161E-01	3	1	0	2	0
14	-6.677871235873632	3	0	1	2	0
15	0.3230596559212831	3	1	0	1	1
16	5.579748134331294	3	0	1	1	1
17	-1.2348750563299528	3	1	0	0	2
18	-2.649286727967114	3	0	1	0	2
19	-.1002240380484173E-02	4	4	0	0	0
20	0.2432439570891184E-01	4	3	1	0	0
21	-.5371165538563824	4	2	2	0	0
22	6.706267212255762	4	1	3	0	0
23	2.951135158640844	4	0	4	0	0
24	-.1216180993367586	4	2	0	2	0
25	3.422881676739932	4	1	1	2	0
26	27.527622201101146	4	0	2	2	0
27	0.1042462049886650	4	0	0	4	0
28	0.3129009809743562E-01	4	2	0	1	1
29	-4.237039698437211	4	1	1	1	1
30	-149.5306776260850	4	0	2	1	1
31	-1.131562926714324	4	0	0	3	1
32	0.3145378714905080	4	2	0	0	2

Table A.1: S800 Spectrograph inverse map for the d(^{15}C.p)^{15}C Run 250: θ_i coefficients. 1 through 32

101

COEFF.#	COEFFICIENT	ORDER	x_f	θ_f	y_f	o_f
33	3.356730525990590	4	1	1	0	2
34	57.603249159008870	4	0	2	0	2
35	4.953080490924174	4	0	0	2	2
36	-22.308420644165410	4	0	0	1	3
37	45.952972441190320	4	0	0	0	4
38	0.3429281193989573E-03	5	5	0	0	0
39	-.1679092925852384E-01	5	4	1	0	0
40	0.4812204884767724	5	3	2	0	0
41	-5.157829585045262	5	2	3	0	0
42	13.936010535123897	5	1	4	0	0
43	-168.2935367400184	5	0	5	0	0
44	0.9083048360701847E-01	5	3	0	2	0
45	-2.499763914051796	5	2	1	2	0
46	-.9697871943241258	5	1	2	2	0
47	-271.3981769974299	5	0	3	2	0
48	2.244629435074556	5	1	0	4	0
49	-140.2375599763948	5	0	1	4	0
50	-.2363170159951434	5	3	0	1	1
51	7.806995559415742	5	2	1	1	1
52	108.1019830503182	5	1	2	1	1
53	508.4165478299566	5	0	3	1	1
54	-47.28452137313806	5	1	0	3	1
55	1231.055326725062	5	0	1	3	1
56	0.2455417622263393E-01	5	3	0	0	2
57	-3.220268099903207	5	2	1	0	2
58	-86.73584920979262	5	1	2	0	2
59	-822.0917226364035	5	0	3	0	2
60	101.6242221513660	5	1	0	2	2
61	-7412.967380460020	5	0	1	2	2
62	-214.6360740703337	5	1	0	1	3
63	18221.74004856613	5	0	1	1	3
64	-86.53002053745986	5	1	0	0	4
65	-6277.057597190409	5	0	1	0	4

Table A.2: θ_i coefficients. 33 through 65

102

COEFF.#	COEFFICIENT	ORDER	x_f	θ_f	y_f	o_f
1	-.1920295071488211	1	0	0	1	0
2	0.7347891249381041	1	0	0	0	1
3	-.1033129056067584	2	1	0	1	0
4	-.2203567611893739	2	0	1	1	0
5	-.1324848207660370E-01	2	1	0	0	1
6	-.4853702323301030	2	0	1	0	1
7	0.1263327012468133E-01	3	2	0	1	0
8	-.2395092718790498	3	1	1	1	0
9	11.0971060800374	3	0	2	1	0
10	2.72770459827873	3	0	0	3	0
11	-.3640297776247747E-02	3	2	0	0	1
12	-.7779900951805825	3	1	1	0	1
13	-5.742381402515887	3	0	2	0	1
14	2.911457591574665	3	0	0	2	1
15	-41.08100016786841	3	0	0	1	2
16	101.2027027669039	3	0	0	0	3
17	-.1940685160647793E-01	4	3	0	1	0
18	0.5823167057342488	4	2	1	1	0
19	-9.092347055445552	4	1	2	1	0
20	-19.19315131776759	4	0	3	1	0
21	-1.871713165715945	4	1	0	3	0
22	-18.34822065688821	4	0	1	3	0
23	0.7156771128204301E-01	4	3	0	0	1
24	-.4865745669826432E-01	4	2	1	0	1
25	2.461346326800790	4	1	2	0	1
26	109.4646522496107	4	0	3	0	1
27	11.91115576036086	4	1	0	2	1
28	145.6105081325150	4	0	1	2	1
29	-51.73023950073779	4	1	0	1	2
30	-260.6228316774000	4	0	1	1	2
31	109.6660255756332	4	1	0	0	3
32	275.7857514788462	4	0	1	0	3

Table A.3: y_i Coefficients. 1 through 32

103

COEFF.#	COEFFICIENT	ORDER	x_f	θ_f	y_f	o_f
33	0.10849371677768790E-01	5	4	0	1	0
34	-.4719499515879917	5	3	1	1	0
35	6.176488835723560	5	2	2	1	0
36	-3.649832633883651	5	1	3	1	0
37	207.7295966071128	5	0	4	1	0
38	1.4414371553345459	5	2	0	3	0
39	-6.745220376261910	5	1	1	3	0
40	296.6572001361229	5	0	2	3	0
41	52.33390077883427	5	0	0	5	0
42	-.2250566000609197E-01	5	4	0	0	1
43	0.3727363885104378	5	3	1	0	1
44	-4.194001722020233	5	2	2	0	1
45	-111.6252779998085	5	1	3	0	1
46	-69.57494977794762	5	0	4	0	1
47	-8.367781053966697	5	2	0	2	1
48	-13.84884106206439	5	1	1	2	1
49	-1362.810593279643	5	0	2	2	1
50	-644.3286424339865	5	0	0	4	1
51	14.36814868841613	5	2	0	1	2
52	-185.1466615364257	5	1	1	1	2
53	6551.786630883448	5	0	2	1	2
54	3223.128946287549	5	0	0	3	2
55	-27.24439163058430	5	2	0	0	3
56	520.2333745223863	5	1	1	0	3
57	-12637.10526071586	5	0	2	0	3
58	56.08873162572854	5	0	0	2	3
59	-40407.94275596144	5	0	0	1	4
60	66121.24475967788	5	0	0	0	5

Table A.4: y_i Coefficients. 33 through 60

104

COEFF.#	COEFFICIENT	ORDER	x_f	θ_f	y_f	o_f
1	-1.316253135795306	1	0	0	1	0
2	-.1709711799982999	1	0	0	0	1
3	0.1345408763409112	2	1	0	1	0
4	3.090477505241490	2	0	1	1	0
5	-.5136398054735815	2	1	0	0	1
6	-14.95626760366406	2	0	1	0	1
7	-.15173510215978:39	3	2	0	1	0
8	0.2295762674114112	3	1	1	1	0
9	-8.456560866208315	3	0	2	1	0
10	-9.385039498794230	3	0	0	3	0
11	0.8300282057654016	3	2	0	0	1
12	3.191347461178531	3	1	1	0	1
13	8.091550670842649	3	0	2	0	1
14	118.8961961639576	3	0	0	2	1
15	-735.3361028927541	3	0	0	1	2
16	1643.696362435215	3	0	0	0	3
17	0.3944672975661004E-01	4	3	0	1	0
18	-.5404379833221067	4	2	1	1	0
19	7.533269231750142	4	1	2	1	0
20	16.39510897706597	4	0	3	1	0
21	1.957196997567717	4	1	0	3	0
22	-11.10119007753684	4	0	1	3	0
23	-.1313749046064569	4	3	0	0	1
24	-1.560781874706382	4	2	1	0	1
25	-6.361983293173314	4	1	2	0	1
26	-97.87276425701506	4	0	3	0	1
27	-25.55828895422177	4	1	0	2	1
28	272.6781007756152	4	0	1	2	1
29	156.0355879939214	4	1	0	1	2
30	-1345.608234268372	4	0	1	1	2
31	-366.6545543415910	4	1	0	0	3
32	628.3680318363214	4	0	1	0	3

Table A.5: o_i Coefficients. 1 through 32

105

COEFF.#	COEFFICIENT	ORDER	x_f	θ_f	y_f	o_f
33	-.1058986035685021E-01	5	4	0	1	0
34	0.3655123620967058	5	3	1	1	0
35	-4.739384415096927	5	2	2	1	0
36	1.701915687364330	5	1	3	1	0
37	-193.1197867145880	5	0	4	1	0
38	-2.046977213666360	5	2	0	3	0
39	12.71085258667377	5	1	1	3	0
40	-327.3944039357717	5	0	2	3	0
41	-147.1718674711495	5	0	0	5	0
42	0.3497017237377484E-02	5	1	0	0	1
43	0.2989830219576706E-01	5	3	1	0	1
44	7.031127326834009	5	2	2	0	1
45	101.8648289603465	5	1	3	0	1
46	178.7475412548374	5	0	4	0	1
47	26.80596757581770	5	2	0	2	1
48	-111.6556195867163	5	1	1	2	1
49	1543.943055814273	5	0	2	2	1
50	3650.689074006173	5	0	0	4	1
51	-138.1833543282689	5	2	0	1	2
52	687.8417130271046	5	1	1	1	2
53	-5212.266783518987	5	0	2	1	2
54	-42048.92640472157	5	0	0	3	2
55	275.9338763336268	5	2	0	0	3
56	-810.3170460892987	5	1	1	0	3
57	10365.43067109001	5	0	2	0	3
58	257458.7203719560	5	0	0	2	3
59	-825024.4352411738	5	0	0	1	4
60	1111583.494821192	5	0	0	0	5

Table A.6: o_i Coefficients. 33 through 60

106

COEFF.#	COEFFICIENT	ORDER	x_f	θ_f	y_f	o_f
1	0.208798191823932	1	1	0	0	0
2	-.255990639942062 1E-01	1	0	1	0	0
3	0.162112779657323 5E-01	2	2	0	0	0
4	0.184846360475197 9	2	1	1	0	0
5	0.559379450795558 1	2	0	2	0	0
6	0.943087264247304 3E-01	2	0	0	2	0
7	-.468361640003991 6	2	0	0	1	1
8	1.160839310896839	2	0	0	0	2
9	0.181283758472082 7E-02	3	3	0	0	0
10	-.297600047919600 3E-01	3	2	1	0	0
11	0.247925454864779 2	3	1	2	0	0
12	-3.48213583516213 4	3	0	3	0	0
13	0.659477055967195 2E-01	3	1	0	2	0
14	-3.39686952772756 4	3	0	1	2	0
15	-.448814576160486 4E-01	3	1	0	1	1
16	2.519870859434191	3	0	1	1	1
17	-.967825999847035 77E-01	3	1	0	0	2
18	-.254325493434 7407	3	0	1	0	2
19	-.634620588228425 4E-03	4	4	0	0	0
20	0.175453555657385 6E-01	4	3	1	0	0
21	-.402255387668039 3	4	2	2	0	0
22	1.74636730701123 4	4	1	3	0	0
23	-2.06501430082237 9	4	0	4	0	0
24	-.674430157057400 0E-01	4	2	0	2	0
25	2.42017970945880 0	4	1	1	2	0
26	10.3548039567851 0	4	0	2	2	0
27	0.321203723718357 9	4	0	0	4	0
28	-.162502038774937 2E-01	4	2	0	1	1
29	-2.93032772329550 7	4	1	1	1	1
30	-73.7680660699938 8	4	0	2	1	1
31	-5.63146547154146 2	4	0	0	3	1
32	0.235755181318081 0	4	2	0	0	2

Table A.7: δ_i Coefficients. 1 through 32

107

COEFF.#	COEFFICIENT	ORDER	x_f	θ_f	y_f	o_f
33	1.6740751463199933	4	1	1	0	2
34	29.926943526237009	4	0	2	0	2
35	38.13108091224152	4	0	0	2	2
36	-109.93543737306786	4	0	0	1	3
37	87.4427699683976	4	0	0	0	4
38	0.2500539636277098E-03	5	5	0	0	0
39	-.13192392252246566E-01	5	4	1	0	0
40	0.37425784735506363	5	3	2	0	0
41	-4.262350668282729	5	2	3	0	0
42	14.453637390158811	5	1	4	0	0
43	-99.07062511808607	5	0	5	0	0
44	0.5821811252377521E-01	5	3	0	2	0
45	-1.795574175581190	5	2	1	2	0
46	1.8698258132414416	5	1	2	2	0
47	-138.3606919125615	5	0	3	2	0
48	1.0825928724066654	5	1	0	4	0
49	-67.95073250807742	5	0	1	4	0
50	-.12602011232177747	5	3	0	1	1
51	4.526701509082688	5	2	1	1	1
52	64.96880254400155	5	1	2	1	1
53	171.35551609393879	5	0	3	1	1
54	-8.943632396559504	5	1	0	3	1
55	602.1414458343033	5	0	1	3	1
56	-.4440836666185811E-02	5	3	0	0	2
57	-1.598948005330861	5	2	1	0	2
58	-51.517754592816684	5	1	2	0	2
59	-372.3077536197112	5	0	3	0	2
60	59.25943731076722	5	1	0	2	2
61	-3723.022051736396	5	0	1	2	2
62	-155.0035926351115	5	1	0	1	3
63	9365.777901842415	5	0	1	1	3
64	46.95704879872928	5	1	0	0	4
65	-3435.738808957916	5	0	1	0	4

Table A.8: δ_i Coefficients. 33 through 65

108

BIBLIOGRAPHY

[*Alcock et al.*(1987)] Alcock. C.. Fuller. G.M.. and Mathews. G.J.. *The Quark-Hadron Phase Transition and Primordial Nucleosynthesis.* **The Astrophysical Journal** 320: 439-447. 1987.

[*Applegate et al.*(1987)] Applegate. J.H.. Hogan. C.J.. Scherrer. R.J.. *Cosmological Baryon Diffusion and Nucleosynthesis.* **Physical Review D** 35: 1151-1160. 1987.

[*Applegate et al.*(1988a)] Applegate. J.H.. Hogan. C.J.. Scherrer. R.J.. *Cosmological Quantum Chromodynamics. Neutron Diffusion. and the Production of Primordial Heavy Elements.* **The Astrophysical Journal** 329: 572-576. 1988.

[*Applegate*(1988b)] Applegate. J.H.. *Neutron Diffusion. Primordial Nucleosynthesis. and the r-Process.* **Physics Reports** 163: 141-154. 1988.

[*Arzumanov et al.*(2000)] Arzumanov. S. et al.. *Neutron life time value measured by storing ultracold neutrons with detection of inelastically scattered neutrons.* **Physics Letters B** 483: 15-22. 2000.

[*Austern*(1970)] Austern. N.. **Direct Nuclear Reaction Theories.** John Wiley & Sons. New York. 1970.

[*Balbes et al.*(1993)] Balbes. M.J. et al.. *²H Induced Reactions on ⁸Li and Primordial Nucleosynthesis.* **Physical Review Letters** 71: 3931-3934. 1993.

[*Balbes et al.*(1995)] Balbes. M.J. et al.. *Cross Sections and Reaction Rates of d + ⁸Li Reactions Involved in Big Bang Nucleosynthesis.* **Nuclear Physics A** 584: 315-334. 1995.

[*Bazin*(1998)] Bazin. D.. *Pravite Communication*

[*Berz et al.*(1993)] Berz. M.. Joh. K.. Nolen. J.A.. Sherrill. B.M.. and Zeller. A.F.. *Reconstructive Correction of Aberrations in Nuclear Particles Spectrograph.* **Physical Review C** 47: 537-544. 1993.

[*Berz*(1995)] Berz. M.. **COSY INFINITY User's Guide and Reference Manual.** version 7. MSUCL-977. 1995.

109

[*Boesgaard and Steigman*(1985)] Boesgaard. A.M.. and Steigman.G.. *Big Bang Nucleosynthesis: Theories and Observations*. **Ann. Rev. Astron. Astrophys.** 23: 219-378. 1985.

[*Boyd and Kajino*(1989)] Boyd. R.N.. and Kajino. T.. *Can ^9Be Provide a Test of Cosmological Theories?*. **The Astrophysical Journal** 336: L55-L58. 1989.

[*Boyd*(1999)] Boyd. R.N.. *Nuclear Astrophysics at the Beginning of the Twenty-first Century*. **Heavy Element and Related New Phenomena**. editors: Walter. G.. Raj. K.G.. 1999

[*Boyd*(2000)] Boyd. R.N.. *Pravite Communication*

[*Brune et al.*(1991)] Brune. C.R.. Kavanagh. R.W.. Kellogg. S.E.. and Wang. T.R.. *Cross sections for $^3H(^7Li,n_0)^9Be$ and $^3H(^7Li,n_{tot})$.* **Physical Review C** 43: 875-882. 1991.

[*Butler*(1957)] Butler. S.T. in association with Hittmair. O.H.. **Nuclear Stripping Reactions**. Horwitz Publications Inc.. Sydney. 1957.

[*Burles et al.*(1999)] Burless. S.. Nollett. K.M.. Truran. J.W.. and Turner. M.S.. *Sharpening the Predictions of Big-Bang Nucleosynthesis*. **Physical Review Letters** 82: 4176-4179. 1999.

[*Caggiano*(1995)] Caggiano. J.A. Fontus. R.. Jonson. P.H. *Automated Data Acquisition System for S800 Dipole Magnetic Field Mapping*. **NSCL Annual Report**. 1995

[*Caggiano*(1999)] Caggiano. A.J. *Ph.D. dissertation.* **Spectroscopy of Exotic Nuclei with the S800 Spectrograph**. 1999.

[*Cohen*(1971)] Cohen. B.L.. **Concepts of Nuclear Physics**. McGraw-Hill Book Company. New York. 1971.

[*Copi*(1995)] Copi. C.J.. Schramm. D.N.. Turner. M.S.. *Big-Bang Nucleosynthesis and the Baryon Density of the Universe*. **Science** 267: 192-199. 1995.

[*Edmonds*(1974)] Edmonds. A.R.. **Angular Momentum in Quantum Mechanics**. Princeton University Press. New Jersey. 1974.

[*Edwards et al.*(1973)] Edwards. S.. et al.. *Multi-Interaction. Finite-Range. Two-Mode. DWBA Analysis of Direct Nuclear Reactions.* **Physical Journals C** 8: 456-471. 1973.

[*Enge*(1966)] Enge. H.A.. **Introduction to Nuclear Physics**. Addison-Wesley Publishing Company. Inc.. Massachusetts. 1966.

[*Enge*(1979)] Enge. H.A.. *Magnetic Spectrographs for Nuclear Reaction Studies.* **Nuclear Instruments and Methods** 162: 161-180. 1979.

110

[*Esmailzadeh et al.*(1991)] Esmailzadeh. R.E.. Starkman. G.D.. and Dimopoulos. S.. *Primordial Nucleosynthesis without a computer.* **The Astrophysical Journal** 378: 504-518. 1991.

[*Fowler*(1967)] Fowler. W.A. et al.. *Thermonuclear Reaction Rates.* **Annual Review of Astronomy and Astrophysics** 5: 525-570. 1967.

[*Fowler*(1975)] Fowler. W.A. et al.. *Thermonuclear Reaction Rates. II.* **Annual Review of Astronomy and Astrophysics** 13: 69-112. 1975.

[*Fowler*(1993)] Fowler. W.A.. *Nuclear Reactions in Inhomogeneous Cosmologies.* **Physics Reports** 227: 313-319. 1993.

[*Glendenning*(1983)] Glendenning N.K.. **Direct Nuclear Reactions.** Academic Press. New York. 1983.

[*Haidt et al.*(1998)] Haidt. D. et al.. editors. **The European Physical Journal C** 3 1-4: 50. 1998

[*Herndl et al.*(1995)] Herndl. H. et al.. *Proton Capture Reaction Rates in the rp process.* **Physical Review C** 52 2: 1078-1094. 1995

[*Herndl et al.*(1999)] Herndl. H. et al.. *Reaction Rates for Neutron Capture Reactions to C. N. and O Isotopes to the Neutron Rich Side of Stability.* **Physical Review C** 60 064614: 1-12. 1999.

[*Kajino and Boyd*(1990)] Kajino. T.. and Boyd. R.N.. *Production of the Light Elements in Primordial Nucleosynthesis.* **The astrophysical Journal** 359: 267-276. 1990.

[*Kajino et al.*(1990)] Kajino. T.. Mathews. G.J.. Fuller. G.M.. *Primordial Nucleosynthesis of Intermediate-Mass Elements in Baryon-Number-Inhomogeneous Big Bang Models: Observational Test.* **The astrophysical Journal** 364: 7-14. 1990.

[*Kim et al.*(1987)] Kim. K.H. et al.. *Radiative Capture Reaction $^7Be(p,\gamma)^8 B$ at Low Energies.* **Physical Review C** 35 1: 363-366. 1987.

[*Koonin and Mukerjee*(1990)] Koonin. S.E.. Mukerjee. M.. *Branching Ratios in Low-energy Deuteron-induced Reactions.* **Physical Review C** 42: 1639-1645. 1990.

[*Kolb and Turner*(1990)] Kolb. W.K.. and Turner. M.S.. **The Early Universe.** The Addison-Wesley Publishing Company. 1990.

[*Kragh*(1996)] Kragh. H. **Cosmology and Controversy.** Princeton University Press. Princeton. New Jersey. 1996.

[*Krane*(1988)] Krane. K.S.. **Introductory Nuclear Physics.** John Wiley and Sons. 1988.

111

[*Krauss and Romanelli*(1990)] Krauss, L.M., Romanelli, P., *Big Bang Nucleosynthesis: Predictions and Uncertainties*. **The astrophysical Journal** 358: 47-59, 1990.

[*Kunz*(1979)] Kunz, P.D., *DWBA code DWUCK*. **University of Colorado**. 1968. extended version DWUCK4 by Kunz, P.D. in 1979.

[*Macefield et al.*(1963)] Macefield, B.E.F., Middleton, R. and Pullen, D.J., *The Mechanism of the Reaction* $^{76}Se(d,p)^{77}Se$. **Nucl.Phys.** 44: 309-319, 1963.

[*Malaney and Fowler*(1988)] Malney, R.A. and Fowler, W.A., *Late-Time Neutron Diffusion and Nucleosynthesis in a Post-QCD Inhomogeneous* $\Omega_b = 1$ *Universe*. **The astrophysical Journal** 333:14-20, 1988.

[*Malaney and Fowler*(1989)] Malney, R.A. and Fowler, W.A., *On Nuclear Reactions and* ^9Be *Production in Inhomogeneous Cosmologies*. **The astrophysical Journal** 345: L5-L8, 1989.

[*Malaney and Mathews*(1993)] Malney, R.A. and Mathews, G.J., *Probing the Early Universe: A Review of Primordial Nucleosynthesis Beyond the Standard Big Bang*. **Nucl. Phys. Rep.** 229: 147, 1993.

[*Mathews et al.*(1990)] Mathews, G.J., Meyer, B.S., Alcock, C.R., Fuller, G.M., *Coupled Baryon Diffusion and Nucleosynthesis in the Early Universe*. **The astrophysical Journal** 358: 36-46, 1990.

[*Mathews et al.*(1996)] Mathews, G.J., Kajino, T., and Orito, M., *Inhomogeneous Primordial Nucleosynthesis and New Abundance Constraints on* $\Omega_b h^2$. **The astrophysical Journal** 456: 98-105, 1996.

[*Mohr et al.*(1993)] Mohr, P. et al., *Alpha Scattering and Capture Reactions in the* $A=7$ *System at Low Energies*. **Physical Review C** 48 3: 1420-1427, 1993.

[*NSCL*(1997)] National Superconducting Cyclotron Laboratory, Michigan State University, *The A1200 Beam Analysis System*. http://www.nscl.msu.edu/facility/devices/a1200/home.html

[*NSCL*(1999)a] National Superconducting Cyclotron Laboratory, Michigan State University, *The K1200 Cyclotron*. http://www.nscl.msu.edu/facility/k1200/

[*NSCL*(1999)b] National Superconducting Cyclotron Laboratory, Michigan State University, *Electronic Tour of the NSCL Facility*. http://www.nscl.msu.edu/facility/facilitytour/

[*NSCL*(2000)] National Superconducting Cyclotron Laboratory, Michigan State University, *ECR Ion Source* . http://www.nscl.msu.edu/facility/ecr/

[*Olive and Schramm*(1998)] Olive, K.A., and Schramm, D.N., *Big-Bang Nucleosynthesis*. **The European Physical Journal C** 3: 119-121, 1998.

[*Oppenheimer and Phillips*(1935)] Oppenheimer. J.R.. and Phillips. M.. **Physical Review** 48: 515. 1935.

[*Orito et all.*(1997)] Orito. M.. Kajino. T.. Boyd. R.N.. and Mathews. G.J.. *Geometrical Effects of Baryon Density Inhomogeneities on Primordial Nucleosynthesis.* **The Astrophysical Journal** 488: 515-523. 1997.

[*Pagel*(1997)] Pagel. B.E.J.. **Nucleosynthesis and Chemical Evolution of Galaxies.** Cambridge University Press. Cambridge. 1997.

[*Perlmutter et al.*(1999)] Perlmutter. S.. et all.. *Measurement of Ω and Λ from 42 High-Redshift Supernovae.* **The Astrophysical Journal** 517: 565-586. 1999.

[*Rauscher et al.*(1994)] Rauscher. R.. Applagate. J.H.. Cowan. J.J.. Thielemann. F.. and Wiescher. M.. *Production of Heavy Elements in Inhomogeneous Cosmologies.* **The Astrophysical Journal** 429: 499-530. 1994.

[*Riley and Irvine*(1991)] Riley. S.P.. and Irvine. J.M.. *Primordial Nucleosynthesis Revisited.* **J. Phys. G: Nucl. Part. Phys.** 17: 35-48. 1991.

[*Rolfs and Rodney*(1988)] Rolfs. C.E.. and Rodney. W.S.. **Cauldrons in the Cosmos.** The University of Chicago Press. Chicago and London. 1988.

[*Sanderson*(1995)] Sanderson. D.P. *Aligning The S800 Beam line.* **NSCL Annual Report.** 1995

[*Satchler*(1983)] Satchler. G.R.. **Direct Nuclear Reactions.** Oxford University Press. New York. 1983.

[*Satchler*(1990)] Satchler. G.R.. **Introduction to Nuclear Reactions.** Macmillan Education Ltd.. London. 1990.

[*Segre*(1965)] Segre. E.. **Nuclei and Particles.** W.A. Benjamin Inc.. New York. 1965.

[*Serber*(1947)] Serber. R.. **Physical Review** 72: 1008. 1947.

[*Sherrill et al.*(1992)] Sherrill. B. et al.. **Nucl. Inst. Meth. B** 70: 289. 1992.

[*Sherrill*(1999)] Sherrill. B. *The S800 Spectrograph.* **http://www.nscl.msu.edu/ facility/devices/s800/s800.html**

[*Smith et al.*(1993)] Smith. M.S.. Kawano. L.H.. Malaney. R.A.. *Experimental. Computational. and Observational Analysis of Primordial Nucleosynthesis.* **The Astrophysical journal supplement Series** 85: 219-247. 1993.

[*Smoot and Scott*(1998)] Smoot. G.F.. and Scott. D.. *Cosmic Background Radiation.* **The European Physical Journals C** 3: 127-131. 1998.

[*Steigman et al.*(1999)] Steigman. G., Hata. N., and Felten. J.E., *Nonnucleosynthetic Constraints on the Baryon Density and Other Cosmological Parameters*. **The Astrophysical Journal** 510: 564-575, 1999.

[*Suh and Mathews*(1998)] Suh. I., and Mathews. G.J., *Finite Temperature Effects on Cosmological Baryon Diffusion and Inhomogeneous Big-Bang Nucleosynthesis*. **Physical Review D** 58: 61-68, 1998.

[*Thielemann et al.*(1991)] Thielemann. F., Applagate. J.H., Cowan. J.J., and Wiescher. M., *Production of Heavy Elements in Inhomogeneous Cosmologies*. Harvard-Smithsonian Center for Astrophysics. Preprint Series. No: 3232. 1991.

[*Tilley et al.*(1993)] Tilley. D.R. et al., *Energy Levels of Light Nuclei*. **Nuclear Physics A** 564: 11. 1993.

[*Walker et al.*(1991)] Walker. T.P., Steigman. G., Schramm. D.N., Olive. K.A., Kang. H., *Primordial Nucleosynthesis Redux*. **The Astrophysical Journal** 376: 51-69. 1991.

[*Wiescher et al.*(1990)] Wiescher. M., Gorres. J., Thielemann. F.K., *Coature Reactions on* ^{14}C *in Nonstandard Big Bang Nucleosynthesis*. **The Astrophysical Journal** 363: 340-343. 1990.

[*Yang et al.*(1984)] Yang. J., Turner. M.S., Steigman.G., Schramm. D.N., and Olive. K.A., *Primordial Nucleosynthesis: A critical Comparison of Theory and Observation*. **The Astrophysical Journal** 281: 493-511. 1984.

[*Yurkon et al.*(1994)] Yurkon. J., Scherrill. B., Morrissey. D., Bazin. D., Brown. J., Swan. D. *Progress in Focal Plane Detector Development for the S800 Spectrograph*. **NSCL Annual Report**. 1994

[*Yurkon et al.*(1996)] Yurkon. J., Scherrill. B., Bazin. D., Steiner. M., Swan. D., Swanson. R. *S800 Detector Development for the S800*. **NSCL Annual Report**. 1996

[*Yurkon et al.*(1997)] Yurkon. J., Bazin. D., Benenson. W., Morrissey. D.J., Scherrill. B.M., Swan. D., Swanson. R. *Focal Plane Detector for the S800 High Resolution Spectrometer*. **NSCL Annual Report**. 1997 (http://www.nscl.msu.edu/research/1997_Annual_Report/Yurkon.pdf)

[*Zeller et al.*(1994)] Zeller. A., Sherrill. B., Alfredson. S., Bricker. S., Caggiano. J., DeKamp. J., Fontus. R., Hilbert. H., Johnson. P., Lauomer. H., McGilvra. A., Morris. L., Pendell. D., Sanderson. D., Swanson. R., Welton. R., Zhang. B. *S800 Progress Report*. **NSCL Annual Report**. 1994

[*Zhang*(1997)] Zhang. B. *Ph.D. dissertation.* **Characteristics of the Superconducting Megnets for the S800 Spectrometer**. 1997.